Stefan cel Mare University of Suceava

Faculty of Electrical Engineering and Computer Science

Study of electrical properties of bistable molecular materials: Towards nanoelectronic devices

-PH.D. THESIS-

Author:
Eng. Constantin LEFTER

Supervisors:
Prof. Adrian GRAUR
Dr. Azzedine BOUSSEKSOU

Suceava, January 2016

THÈSE

Soutenance prévue le *19/01/2016* **par :**
Constantin LEFTER

Études des propriétés électriques des matériaux á transition de spin:
vers des dispositifs pour la nano- électronique.

Résumé

Études des propriétés électriques des matériaux moléculaires bistables: vers des dispositifs pour la nano-électronique.

L'objectif central de cette thèse est l'évaluation de la possibilité d'utilisation de complexes moléculaires à transitions de spin pour des applications en nano-électronique. Dans un premier temps, les propriétés électriques du complexe $[Fe(Htrz)_2(trz)](BF_4)$ et de ces analogues $[Fe_{1-x}Zn_x(Htrz)_2(trz)](BF_4)$ ont été analysées sous forme de poudres au moyen de la spectroscopie diélectrique. Il a été montré que les conductivités AC et DC aussi bien que la constante diélectrique et que la fréquence de relaxation diélectrique subissent une baisse importante lors de la transition de l'état bas spin (BS) vers l'état haut spin (HS). Les molécules à base de cations de fer gardent leurs propriétés de transition de spin dans les échantillons dilués de Zn, mais les courbes de transition de spin sont considérablement altérées. La substitution par Zn des centres de fer actifs mène à une importante baisse de la conductivité électrique d'environ 6 ordres de grandeur (pour Zn/Fe = 0.75). Nous concluons de ces résultats que les ions Fe(II) participent directement au processus de transport des charges, qui a été analysé dans le cadre d'un modèle de conductivité par saut de porteurs de charge activé thermiquement. Des particules micrométriques de $[Fe(Htrz)_2(trz)](BF_4)$ ont été alors intégrées par diélectrophorèse entre des électrodes d'or. Ainsi, nous avons obtenu un dispositif montrant un phénomène de bistabilité lors de la caractérisation I-V, T. La stabilité du matériau initial et le dispositif électronique ont été contrôlés avec précision et les effets concomitants de changements de températures, d'irradiation lumineuse et du champ électrique sur l'intensité du courant ont été analysés en détail. D'une part, nous avons montré que le dispositif peut être adressé de manière préférentielle par une irradiation lumineuse en fonction de son état de spin, et d'autre part, nous avons démontré la commutation de l'état métastable HS vers l'état stable BS par application d'un champ électrique à l'intérieur du cycle d'hystérésis. Les effets de champ ont été discutés dans le cadre de modèles de type Ising statiques et dynamiques, tandis que les phénomènes photo-induits étaient attribués à des effets de surface. Le complexe $[Fe(H_2B(pz)_2)_2(phen)]$ a également été caractérisé par spectroscopie diélectrique sous forme de poudre et ensuite intégré par évaporation thermique sous vide au sein d'un dispositif vertical entre les électrodes en Al et ITO. Cette approche nous a permis de sonder la commutation de l'état de spin dans la couche de $[Fe(bpz)2(phen)]$ par des moyens optiques tout en détectant les changements de résistance associés, à la fois dans les régimes à effet tunnel (jonction de 10 nm) et dans les régimes à injection (jonctions de 30 et 100 nm). Le courant tunnel dans les jonctions à transition de spin diminue durant la commutation de l'état BS vers l'état HS, tandis que le comportement de rectification des jonctions « épaisses » ne révélait aucune dépendance significative à l'état de spin. L'ensemble de ces résultats ouvre la voie à de nouvelles perspectives pour la construction de dispositifs électroniques et spintroniques incorporant des matériaux à transition de spin.

Abstract

Study of electrical properties of bistable molecular materials: towards nanoelectronic devices

The central theme of this thesis is the evaluation of potential interest and applicability of molecular spin crossover (SCO) complexes for nanoelectronic applications. The electrical properties of the $[Fe(Htrz)_2(trz)](BF_4)$ complex and its Zn substituted analogues were analyzed first in the bulk powder form using broadband dielectric spectroscopy. It has been shown that the ac and dc conductivities as well as the dielectric constant and the dielectric relaxation frequency exhibit an important drop when going from the low spin (LS) to the high spin (HS) state. The iron ions kept their spin transition properties in the Zn diluted samples, but the SCO curves were significantly altered. The Zn substitution of active iron centers led to an important decrease of the electrical conductivity of ca. 6 orders of magnitude (for Zn/Fe = 0.75). We concluded from these results that the ferrous ions directly participate to the charge transport process, which was analyzed in the frame of an activated hopping conductivity model. Micrometric particles of $[Fe(Htrz)_2(trz)](BF_4)$ were then integrated by dielectrophoresis between interdigitated gold electrodes leading to a device exhibiting bistability in the I-V,T characteristics. The stability of the starting material and the electronic device were carefully controlled and the concomitant effect of temperature changes, light irradiation and voltage bias on the current intensity were analyzed in detail. We showed that the device can be preferentially addressed by light stimulation according to its spin state and the switching from the metastable HS to the stable LS state was also demonstrated by applying an electric field step inside the hysteresis loop. The field effects were discussed in the frame of static and dynamic Ising-like models, while the photo-induced phenomena were tentatively attributed to surface phenomena. The [Fe(bpz)2(phen)] complex was also investigated by dielectric spectroscopy in the bulk powder form and then integrated by high vacuum thermal evaporation into a large-area vertical device with Al (top) and ITO (bottom) electrodes. This approach allowed us to probe the spin-state switching in the SCO layer by optical means while detecting the associated resistance changes both in the tunneling (10 nm junction) and injection-limited (30 and 100 nm junctions) regimes. The tunneling current in the thin SCO junctions showed a drop when going from the LS to the HS state, while the rectifying behavior of the 'thick' junctions did not reveal any significant spin-state dependence. The ensemble of these results provides guidance with new perspectives for the construction of electronic and spintronic devices incorporating SCO molecular materials.

Rezumat

Studiul proprietăților electrice ale materialelor moleculare bistabile: Către dispozitive nanoelectronice

Tema centrală a acestei teze este evaluarea potențialului interes și aplicabilitatea materialelor cu tranziție de spin (SCO) în nanoelectronică. Proprietățile electrice ale complexului $[Fe(Htrz)_2(trz)]$ (BF_4) și complecșii analogi obținuși prin substituirea ionului de Fe cu ionul de Zn au fost analizați pentru prima dată în formă de pulbere folosind spectroscopia dielectrică de bandă largă. Sa demonstrat că atât conductivitatea ac cât și conductivitatea dc, precum și constanta dielectrică și frecvență de relaxare dielectrică prezintă o scădere importantă, atunci când se produce tranziția de la starea de spinul scăzut (LS) la starea de spin înalt (HS). Ionii de fier și-au păstrat proprietatea lor de tranziție de spin și în eșantioanele diluate cu Zn, dar curbele de tranziție de spin au fost modificate semnificativ. Substituția centrilor activi de fier a condus la o scădere semnificativă a conductivității electrice a cca 6 ordine de mărime (Zn / Fe = 0,75). Din aceste rezultate am ajuns la concluzia că ionii de fier participă direct la procesul de transport de sarcină, care a fost analizat în cadrul unui model de conductivitate activat prin salturi. Particule micrometrice de $[Fe(Htrz)_2(trz)]$ (BF_4) au fost apoi integrate prin dielectroforeză între electrozi din aur interdigitali, obținând un dispozitiv care prezintă bistabilitatea în caracteristicile I-V, T. Atât stabilitatea compusului și al dispozitivul electronic cât și efectul modificărilor de temperatură, iradiere cu lumină și al tensiunii electrice au fost analizate în detaliu. Am arătat că dispozitivul poate fi adresat în mod preferențial prin iradiere luminoasă în funcție de starea sa de spin și trecerea de la starea metastabilă HS la starea stabilă LS a fost, de asemenea, demonstrat prin aplicarea unui câmp electric în interiorul ciclului de histerezis. Efectele câmpului electric au fost discutate în cadrul unor modele statice și dinamice de tip Ising, în timp ce fenomenele foto-induse au fost atribuite unor fenomene de suprafață. Complexul cu tranziție de spin [Fe(bpz)2(phen)] a fost, de asemenea, investigat prin spectroscopie dielectrică, sub formă de pulbere și apoi integrat prin evaporare termică în vid înalt într-un dispozitiv nanoelectronic vertical cu electrozi de Al (superior) și ITO (inferior) electrozi. Această abordare ne-a permis să sondăm comutarea stărilor de spin în stratul SCO prin mijloace optice concomitent cu detectarea variației rezistenței asociate cu tranziția de spin în prin tunelare, (joncțiunea de 10 nm) și în regim de limitare de injecție de purtători de sarcină (joncțiunile de 30 și 100 nm). Curentul de tunelare în joncțiunile de 10 nm SCO prezintă o scădere, atunci când dispozitivul trece din starea LS în starea HS, în timp ce comportamentul de rectificare a joncțiunilor de 30 si 100 nm nu a evidențiat nici o dependență semnificativă de starea de spin. Ansamblul acestor rezultate furnizează noi perspective pentru construirea de dispozitive electronice și spintronice pe baza materialelor moleculare cu tranziție de spin.

Table of Contents

Contents

List of Figures

List of Tables

List of Tables

List of Abbreviations

AC	Alternating Current
BDS	Broadband Dielectric Spectroscopy
CITS	Current-imaging tunneling spectroscopy
DC	Direct Current
DFT	Density Functional Theory
DSC	Differential Scanning Calorimetry
EDX	Energy Dispersive X-ray Spectroscopy
EL	Electroluminescence
FIB	Focused ion beam
HN	HavriliakNegami
HOPG	Highly oriented pyrolytic graphite
HS	High spin
ITO	Indium tin oxide
LS	Low spin
MO	Molecular Orbital
ROM	read-only memory
SCE	Saturated Calomel Electrode
SCLC	Space charge limited current
SCO	Spin Crossover
STM	Scanning Tunneling Microscope/Microscopy
SQUID	Superconducting Quantum Interface Magnetometer
TEM	Transmission Electron Microscope/Microscopy

General introduction and motivation

Switchable molecular materials have been in the research spotlight since the miniaturization of silicon based devices and conventional magnetic storage devices, approach the technological and physical limits [1–3]. In this context, the field of molecular electronics might bring some solutions in the miniaturization equation with the use of molecular switches [4, 5], single molecular magnets [6, 7] or molecular logic gates [8–10]. Molecular switches can be switched between two different states (ON or OFF) characterized by two different structures (electronic states, stereo-isomerization or structural isomerization) or oxidative states (redox switches) [4]. Single molecular magnets exhibit slow relaxation of the magnetization at low temperatures and can exhibit striking quantum effects, like tunneling of the magnetization [11]. Molecular logic gates usually transform different chemical, optical, electrical and magnetic inputs into chemical, optical, electrical and magnetic outputs [9].

Among these molecular switches, spin crossover (SCO) compounds present a special interest due to the wide range of their potential applications. These transition metal complexes exhibit reversible switching between the so-called low spin (LS) and high spin (HS) electronic configurations [12–14]. The conversion between these two states can be triggered by various external stimuli such as temperature, pressure, light or X-ray irradiation, an intense magnetic field or the inclusion of guest molecules. The two spin states can then be distinguished by their different magnetic, optical, mechanical, spectroscopic and structural properties. The changes associated with the spin transition can propagate in a cooperative manner [15], which can produce hysteresis phenomena even at room temperature. An appealing aspect of the spin transition is that the switching of the electronic configuration can occur on a sub-ps scale [16], which can translate into THz scale processing rate. From the technological point of view SCO materials have been proposed for numerous applications ranging from displays [17], memory devices [18], pressure and temperature sensors [19], gas sensors [20], nanothermometers [21], optoelectronic devices [22] and actuators [23].

Considering the vast applicability of these materials, several research groups have recently embarked on the study of electrical properties of SCO compounds including the possibility of their addressing by electrical field and/or current. The use of electrical stimuli to control (read/write) the spin-state of the system would provide a great advantage to other stimuli such as temperature or pressure due to a faster dynamics (less inertia), easier size reduction and better compatibility with current technology. Indeed, while the optical, vibrational and magnetic properties have been extensively studied for these compounds, their electrical properties remain mostly unexplored.

Recently, several encouraging results indicated a spin state dependence of the charge transport in SCO molecules and nanoparticles. Nevertheless, in the majority of these studies the fabrication and the characterization of these devices are rather inadequate leading to several uncertainties in the interpretation of their results, in particular giving rise to a

1

strong discrepancy with the bulk properties. However, these results are extremely important from a fundamental point of view, pointing out exciting perspectives for applications in the fields of spintronics and molecular electronics. The pioneering result in electrical characterization of SCO materials has been the detection of the thermal variation of the real part of the dielectric permittivity, exhibiting a hysteretic and photoswitchable behavior in the same manner as the magnetic susceptibility [24, 25]. In this case the imaginary part of the permittivity, which is related to the electrical conductivity did not exhibit any spin state dependence. In order to overcome this drawback, by improving the conductivity of SCO materials, a new approach has been proposed by using the co-crystallization of molecular conductors and SCO complexes to form "conductor-SCO hybrids" [26]. This approach lead to an enhancement by several orders of magnitude the low conductivity of pure SCO materials, leading in some cases [27, 28] to a rather convincing spin state dependence with the LS state being more conductive than the HS state dependence of the electrical conductivity. The first report of a significant conductivity modulation due to spin crossover has been found in the pure $[Fe(HB(pyrazolyl)_3)_2]$ complex, however the complicated interplay between the structural and electronic degrees of freedom lead to irreversible changes of the physical properties after the first cycle [29, 30]. The unambiguous spin state dependence of the dc electrical conductivity has been reported on powder and nanoparticle samples of the compound $[Fe(Htrz)_2(trz)](BF_4)$ (Htrz = 1H-1,2,4-triazole). The dc conductivity presented a clear hysteresis loop, with a more conductive LS state, highlighting the interplay between the spin transition temperatures and the activation parameters [31]. The transport properties of SCO materials at the single molecule or single nanoparticle level have been studied in several recent papers, with promising results towards the application of these materials in molecular electronics and spintronics [32–35]. In each of these papers current-voltage characteristics have been used to characterize the molecular devices, however the results are rather uncertain due to the fact that the change in current might have other origins than the spin transition. The interpretation of these results are rather speculative due to the fact that different physical properties observed on a macroscopic ensemble of SCO particles has been extrapolated to single molecules and single nanoparticles.

In this context, the present thesis aims at presenting a more thorough analysis on the transport properties of SCO materials as well as their integration into micro- and nanoelectronic devices. Broadband dielectric spectroscopy has been used to reveal the **quasi-static and dynamic electrical properties of SCO materials at a macroscopic level**. Micrometric rods were integrated in a well-controlled manner between interdigitated gold electrodes in order to obtain **microelectronic devices** and to study their behavior in variable temperature, under light irradiation and the effect of an external electric field. The robustness and the stability of the sample and the electronic device have been also studied. The SCO based electronic devices have been scaled down to nanometric scale, obtaining a series of **thin film nanoelectronic devices**, which have been thoroughly characterized. All the electrical measurements are complemented by chemical and structural analysis of the compounds.

The manuscript is organized as follows:

The thesis begins with a general introduction and motivation.

Chapter 1 is structured in two main sections consisting of an introduction in the SCO phenomena, the physical principles behind the transition and the stimuli that induce the spin crossover followed by a short description of the techniques used to detect the spin transition. The second part of this chapter consists of an exhaustive review of the achievements in the field of electrical and charge transport properties of SCO materials

organized in three main categories: electrical properties of macroscopic samples, micro-and nanoscale devices and single molecule devices.

Chapter 2 starts with a short explanation of the working principle and the theory behind the broadband dielectric spectroscopy. Based on previous results from the team [31, 36] this technique has been used to analyze the static and dynamic electrical properties of the $[Fe(Htrz)_2(trz)](BF_4)$ complex and the Zn diluted series of the same compound as well as the role of the iron center in the charge transport mechanism. Various electric quantities that represent different facets of the charge carrier dynamics in these systems like conductivity, permittivity and electrical modulus have been analyzed. The electrical study is completed by optical and spectroscopic characterization of the samples in order to accurately determine the effect of Zn dilution on the structure, morphology as well as on the charge transport properties.

The fabrication of a microelectronic device is presented in **Chapter 3**, were micrometric sized rods of $[Fe(Htrz)_2(trz)](BF_4)$ have been organized by dielectrophoresis between interdigitated gold electrodes. Before the integration of the sample in the device, the robustness of the SCO phenomena has been tested through a considerable amount of thermal switches. The influence of different solvents on the spin transition has been also tested. Optimal parameters for dielectrophoresis were determined experimentally for this particular system. Then the effect of temperature, light irradiation and applied bias on the device has been investigated. An exceptional breakthrough towards the implementation of real spintronic devices would be the control of the spin state using an electrical stimuli, therefore, the effect of the electric field has been studied carefully. The results were then analyzed using a simple model based on the interaction between the electric field and the electric dipole moment of spin crossover complexes.

Chapter 4 describes an alternative approach for charge transport measurements in the tunneling regime based on robust, well-reproducible large-area vertical devices with thin SCO spacer layers. Electronic devices in vertical configuration were fabricated with the $[Fe(bpz)_2(phen)]$ (bpz = dihydrobis(pyrazolyl)borate and phen = 1,10-phenantroline) complex. We have chosen this complex because it is well known to give high quality films. We evaporated thin films of this complex with thickness of 10 nm, 30 nm and 100 nm. This approach allowed to probe the spin-state switching in the SCO layer by optical means while detecting the associated resistance changes both in the tunneling (thin junction) and injection-limited (thick junction) regimes. The high current intensity in the devices provided also possibility for mechanistic studies by means of temperature- and frequency-dependent dielectric spectroscopy. Electrical measurements have been completed by optical, magnetic, crystallographic, and spectroscopic measurements of the SCO complex in powder, thin film and in sandwich configuration, providing a complete study of the material and nanoelectronic devices.

The manuscript ends with general conclusions and perspectives.

Chapter 1

Introduction

This chapter consists of an introduction to the spin crossover phenomenon, presenting first the electronic and the thermodynamic phenomena that governs the spin transition, followed by the short presentation of the main stimuli that can be used to induce the spin transition, such as temperature, pressure, magnetic field and light irradiation. The first section ends with the presentation of the most common detection techniques including optical, magnetic, calorimetric, spectroscopic and crystallographic methods. The second part of this chapter provides a comprehensive review of the research about the electrical and charge transport properties of spin crossover complexes. This includes both the effect of spin-state switching on the dielectric permittivity and electrical conductivity of the material and vice-versa the influence of an applied electrical field (or current) on the spin-state of the system. The survey covers different size scales from bulk materials and thin films to nanoparticles and single molecules and embraces the presentation of several device prototypes and hybrid materials as well.

1.1 Spin crossover phenomena

The field of spin crossover (SCO) was initiated by Cambi and co workers in 1931 [37], where they have seen unusual magnetism of iron(III) derivatives of tris-dithiocarbamate complexes with a reversible conversion of the spin state as a result of temperature variation. Spin crossover phenomena occurs in some $3d^4 - 3d^7$ transition metal compounds with a pseudo-octahedral molecular symmetry, where six donor atoms form an octahedron around the metal ion, and depending on the electronic configuration, there can be two spin states called low spin (LS) and high spin (HS). The first occurrence of SCO phenomenon in a iron(II) complex was reported by Baker *et al* [38] in the [$Fe(phen)_2(NCS)_2$] (phen=1,10-phenanthroline) complex. This finding lead to countless other and the effect is currently found in iron(II), iron(III), cobalt(II) and not so often in nickel(II), cobalt(III) and manganese(III), however the majority of studied complexes have an iron(II) central ion.

If an iron(II) ion is set in a perfectly octahedral coordination, the five d orbitals are split into three orbital subsets, d_{xy}, d_{yz}, d_{xz}, which represent the basis of irreducible representation t_{2g}, and another subset of two orbitals, namely d_{z2} and d_{x2-y2} which are basis of e_g irreducible representation. The schematic representation of these orbitals are shown in Figure 1.1. The difference in energy between the two levels is given by the ligand field strength $10Dq$, and depends on the metal-ligand distance with $1/r^n$, where $n = 5 - 6$. In addition to this energy, the electron-electron repulsion, also called the spin pairing energy Π has to be taken into account. If Π is larger than $10Dq$ the electrons can occupy with ease

the orbitals with a higher energy, forming the paramagnetic high spin (HS=2) state. If the electron-electron repulsion is smaller than the ligand field strength, the electrons will populate in pairs the lower energy orbital t_{2g} forming the diamagnetic low spin state (LS=0). This difference in orbital occupation leads to a difference in metal-ligand bond lengths, in the HS state being with ca. 10 % longer than in LS state.
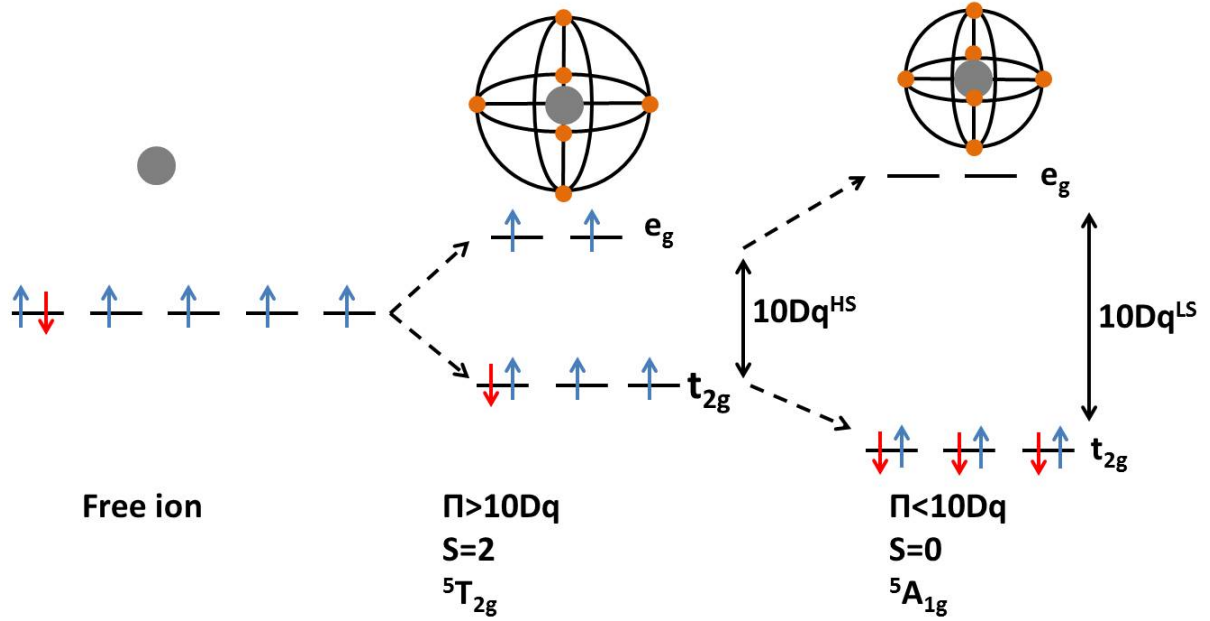
Figure 1.1: Electronic configuration of the two possible ground states for iron(II) ion in an octahedral complex.

The change in ligand field strength in the two states is described by the following equation:

$$\frac{10Dq^{LS}}{10Dq^{HS}} = \left(\frac{r_{HS}}{r_{LS}}\right)^n ; \tag{1.1}$$

with $n = 6$, and using an average value of $r_{LS} = 2.0\,\text{Å}$ and $r_{HS} = 2.2\,\text{Å}$, the ratio is estimated to be ~ 1.75.

In the case of a configurational coordinate diagram (Figure 1.2 [12]) one can see that the minima of the two potential wells are displaced, both horizontally and vertically, relative to each other, the condition for the phenomenon of a thermal spin transition becomes obvious: the zero point energy difference between the two states has to be of the same order as thermal energies:

$$\Delta E_{HL}^0 = E_{HS}^0 - E_{LS}^0 \propto k_B T. \tag{1.2}$$

Taking into account the bond length dependence of $10Dq$ and the fact that Π does not much vary with, the ground state energy ΔE_{HL}^0 between the HS and LS states can be estimated as a function of $10Dq^{HS}$ and $10Dq^{HL}$ respectively, as illustrated in Figure 1.3 [12], where three regimes can be observed:

   a) $10Dq^{HS} < 10000 cm^{-1}$, $\Delta E_{HL}^0 < 0$. Here the HS state is the quantum mechanical ground state and is thermodynamically stable at all temperatures at atmospheric pressure.

b) $10Dq^{LS} > 23000cm^{-1}$, $\Delta E_{HL}^0 > 2000cm^{-1}$. Here the LS state is the quantum mechanical ground state and is thermodynamically stable state up to very high temperatures.

c) $10Dq^{HS} = 11000 - 12500cm^{-1}$, $10Dq^{LS} = 19000 - 22000cm^{-1}$ and $\Delta E_{HL}^0 = 0 - 2000cm^{-1}$. This narrow region represents the area where thermal spin crossover may occur.
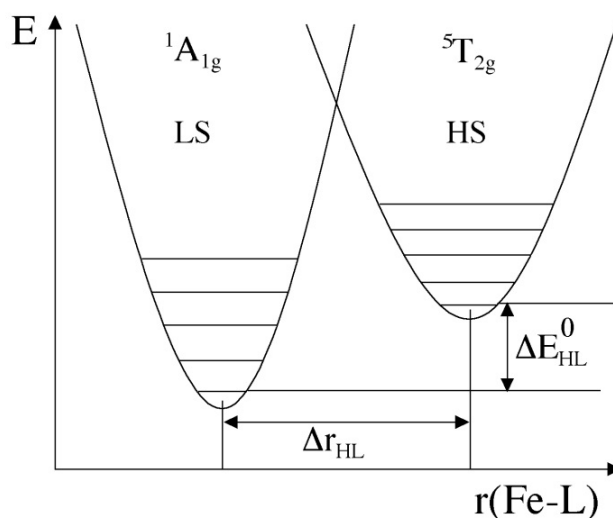
Figure 1.2: Adiabatic potentials for the HS and LS states as a function of the totally symmetric metal-ligand stretch vibration denoted $r(Fe - L)$ (after ref. [12]).
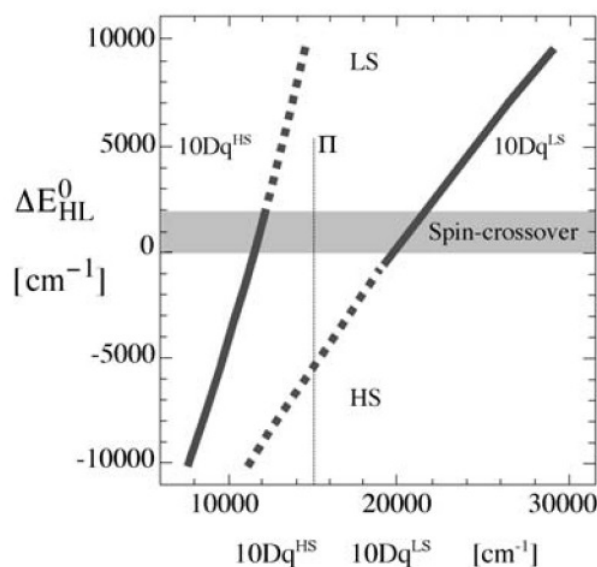
Figure 1.3: Stability regions of the LS and HS states as a function of $10Dq$ [12].

1.1.1 Thermally induced spin state change

The change in spin state can be induced by various stimuli like temperature variation, pressure, light irradiation, magnetic field, or electric field [13, 39, 40], however the most common way to detect spin transition is by temperature variation. The two spin states are in thermodynamic competition and calorimetric measurements provide important thermodynamic quantities such as entropy and enthalpy. The phase change that can be associated to the spin crossover phenomena reveals a change in the Gibbs free energy:

$$\Delta G = G_{HS} - G_{LS} = \Delta H - T\Delta S; \tag{1.3}$$

where $\Delta H = H_{HS} - H_{LS}$ represents the enthalpy variation and $\Delta S = \Delta H / T_{1/2}$ entropy variation. The thermally induced spin transition is an entropy driven process, and approximately 15-35% of the total entropy gain accompanying LS to HS transition arises from the change in spin degeneracy:

$$\Delta S_{mag} = R \cdot ln \frac{(2S+1)_{HS}}{(2S+1)_{LS}}; \tag{1.4}$$

where $2S + 1$ represents the spin degeneracy.
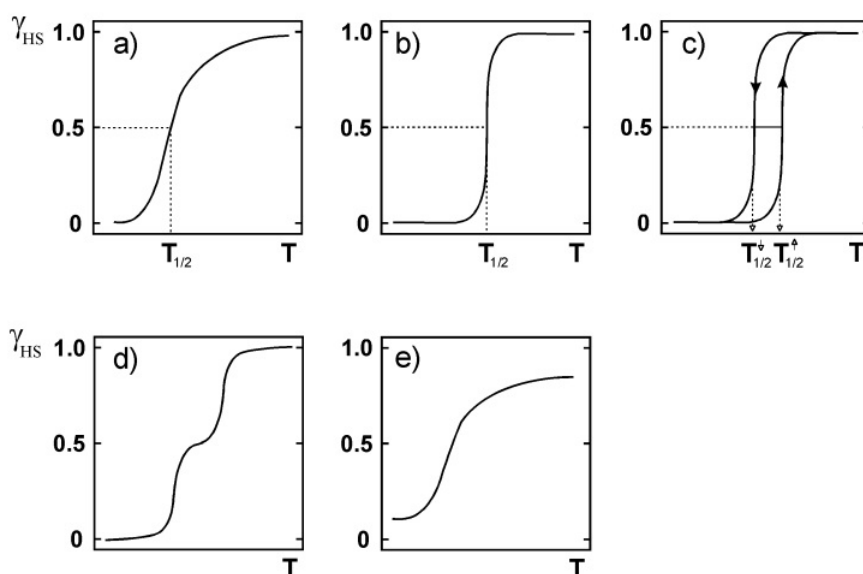
Figure 1.4: Representation of (a) gradual, (b) abrupt, (c) hysteresis, (d) two-step and (e) incomplete spin transition [12].

A spin transition curve plotted as high spin fraction (γ_{HS}) vs. temperature can provide plenty of information depending on its shape. Typical behaviors are presented in Figure 1.4. The main source of the variety of the presented spin crossover curves is the degree of cooperativity between the molecules, which is determined by the lattice properties and the way that metal-ligand deformations are propagated through the solid. One of the most common behavior found in SCO systems is the gradual conversion, denoting relatively weak cooperative interactions. If the degree of cooperativity in the system is increased, an abrupt transition can be found (Figure 1.4b). When a high degree of cooperativity is present in the system, the transition has a hysteretic behavior as illustrated in Figure 1.4c. The hysteresis may have two origins in such systems: one may be the association with a structural phase

change in the lattice and this change is the source of the hysteresis; while the second origin might be the intramolecular structural changes that occur along with a transition may be communicated to neighbouring molecules via a highly effective cooperative interaction between the molecules [12]. The hysteresis loop confers the system a bistability which can be exploited in different applications such as memory devices, molecular switches, sensors, or displays.

For a narrow category of materials, a transition that occurs in two or even three steps can be detected (Figure 1.4d). This behavior can be detected in systems where the metal ions occupy two or several different lattice sites in the material, or due to preferential formations of LS-HS pairs caused by the competition of long range and short range interactions. In the rare examples of 1D SCO complexes that present two step transitions, the plateau region is characterized by a 1:1 ratio between the LS and HS states [41–43].

The incomplete transition can be explained by the presence of some defects in the lattice sites capable of preventing the formation of LS and/or HS species. Another cause may be due to some kinetic effect found at low temperatures, when the conversion rate from one state to another is extremely low.

1.1.2 Pressure induced SCO

Pressure is another perturbation which can trigger or modify the spin transition. Due to the fact that the SCO molecule has a smaller molecular volume in the LS state than in the HS one, pressure is favoring the LS state [44, 45]. When pressure is applied the potential wells suffer a relative vertical displacement, and the gap between the LS and the HS states increases by $p\Delta V$ where ΔV represents the volume difference in the two spin states as showed in Figure 1.5. The energy gap between the two spin states can be expressed as:

$$\Delta E_{HL}^0(p) = \Delta E_{HL}^0 + p\Delta V_{HL}. \tag{1.5}$$

For iron(II) compounds the transition temperature variation per *kbar* is about 15-20 K [46].

1.1.3 Magnetic-field induced SCO

The application of an external magnetic field can stabilize the HS state accompanied with a downward shift in transition temperature due to the fact that the magnetic moment in the HS state is much more important than in the LS state. When the magnetic energy shift $-1/2\chi B^2$ (for *Fe(II)* complexes) is added to the free energy, the transition temperature is shifted according with the Equation 1.6.

$$\Delta T_{1/2} = -\frac{\chi B^2}{2\mu_0 \Delta S(T_{1/2})}; \tag{1.6}$$

where χ is the magnetic susceptibility, B represents the magnetic field, μ_0 is the is the magnetic moment, and $\Delta S(T_{1/2})$ is the entropy difference between HS and LS at transition temperature.

The effect of the magnetic field on [$Fe(phen)_2(NCS)_2$] complex has been studied for the first time by Qi et al. [47] where a temperature shift of $\Delta T_{1/2} = 0.1K$ of the spin transition has been obtained upon the application of an external magnetic field of 5.5 Tesla. the states
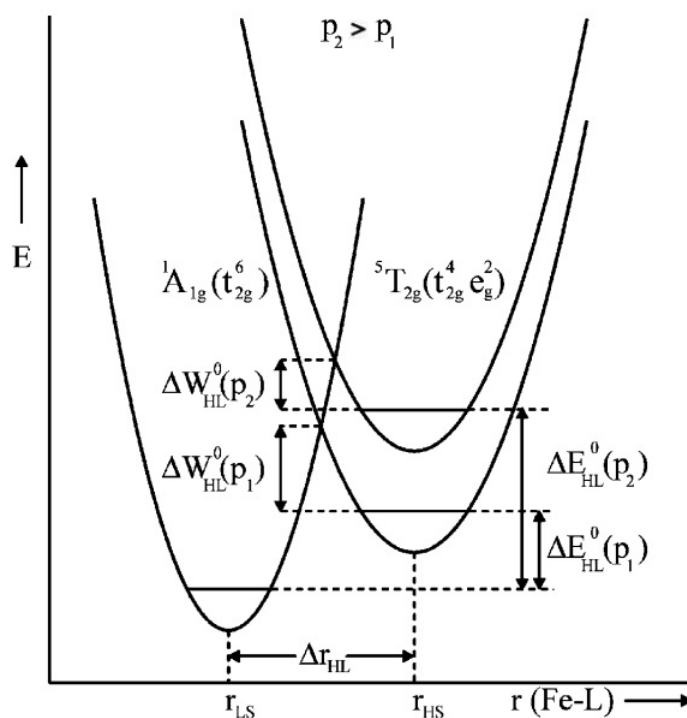
Figure 1.5: Schematic representation of pressure effect on LS and HS potential wells of *Fe(II)* compounds (after ref. [12])
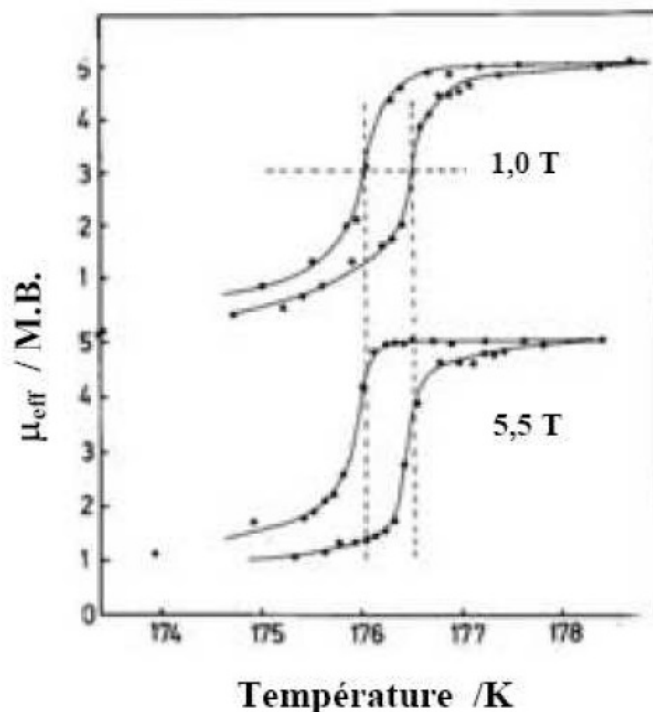
Figure 1.6: Effect of static magnetic field on [*Fe(phen)*$_2$*(NCS)*$_2$] transition temperature [46]

In a more recent paper Bousseksou et al [48] studied theoretically and experimentally the effect of a pulsed magnetic field of 32 Tesla on the same [*Fe(phen)*$_2$*(NCS)*$_2$] compound where they've seen a 2 K temperature shift. By applying the pulsed magnetic field on the

ascending branch of the hysteresis loop of the *Co(H$_2$(fsa)$_2$en)(py)$_2$* SCO complex, they have seen an incomplete and irreversible LS→HS transition, and a reversible effect on the descending branch [49].
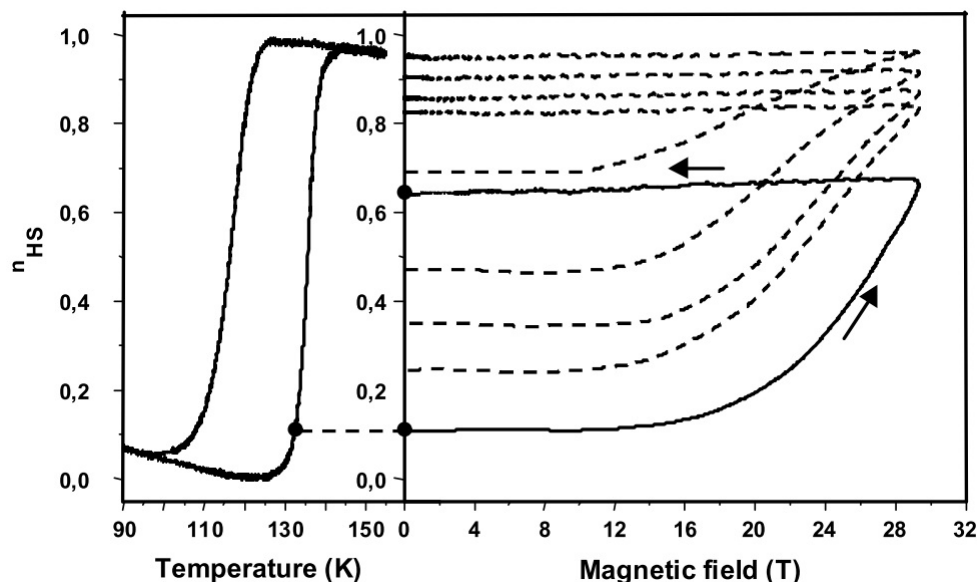
Figure 1.7: Irreversible triggering effect of *Co(H$_2$(fsa)$_2$en)(py)$_2$* in a pulsed magnetic field in the metastable LS state [48]

1.1.4 Light induced spin state change

The first occurrence of light induced spin crossover was reported by McGarvey and Lawthers [50], which had a big impact on the spin crossover research field. They have shown that by using a pulsed laser they could perturb the equilibrium between the two states in several *Fe(II)* SCO compounds in solution. Later, Decurtis [51] discovered that by irradiating a solid *Fe(II)* SCO sample with green *Ar$^+$* laser (λ =514.5 nm) he could excite the LS state into a metastable state until the complete population of the HS state, presenting a long lifetime at sufficiently low temperatures (10^6 s for *[Fe(ptz)$_6$(BF$_4$)$_2$]* at 20 K). This solid state effect was named "Light Induced Excited Spin State Trapping" or LIESST effect. The reverse of the LIESST effect was soon reported by Hauser [52], and was obtained by converting the HS state into LS state using red light (λ =820 nm). The Jablonski diagram (see Figure 1.8 [53]) illustrates the LIESST and reverse LIESST effects with vertical transitions and relaxation processes.

The light induced switching process is thought to occur with the excitation of the sample into the $^1T_1$ energy level, and suffers a first relaxation into the $^3T_1$ level. The second relaxation may occur into the $^5T_2$ (HS) state, where it remains trapped due to the large energy barrier between the two states. Because the energy level $^3T_1$ is below ^5E state for SCO compounds, this suggests a possible reversibility of LIESST effect. This is possible by irradiation with λ =820 nm, which induces a transition between the $^5T_2$ and ^5E levels, where it relaxes via $^3T_1$ to the $^1A_1$ (LS) state. It is worth underlying that the HS trapping was only efficient at low temperatures. This problem was ultimately overcome by Bonhommeau [54], by using a pulsed laser (532 nm) excitation of 8 ns inside the thermal hysteresis loop of the *[Fe(C$_4$H$_4$N$_2$)Pt(CN)$_4$]* complex at room temperature (see Figure 1.9).
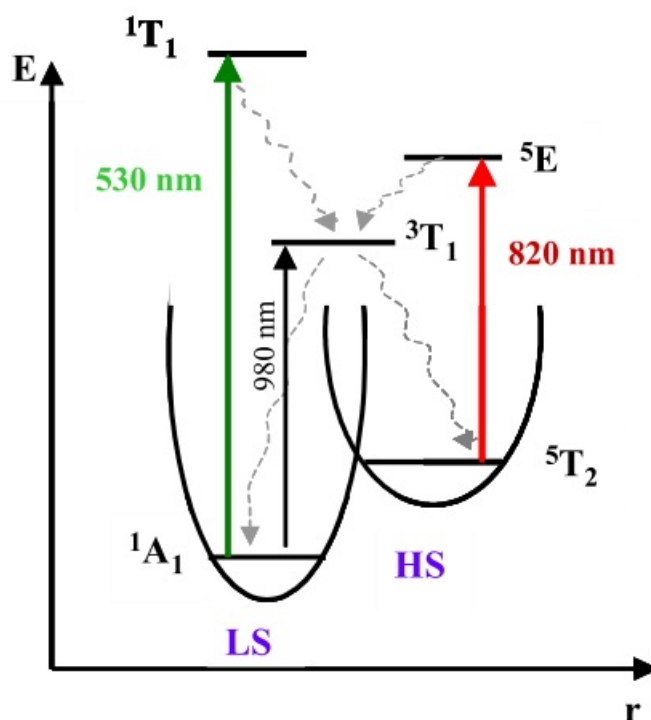
Figure 1.8: Jablonski diagram showing LIESST and reverse LIESST effects [52].

The possibility of a bidirectional spin transition in the same compound using a 4 ns single shot laser (λ =532 nm) pulse was demonstrated by Cobo [55] as illustrated by Figure 1.10. Even though these reports are extremely interesting, one must take into consideration that these phenomena are not purely photoinduced. Actually, these phenomena are probably caused by a mixture of thermal, light, and pressure induced effects.
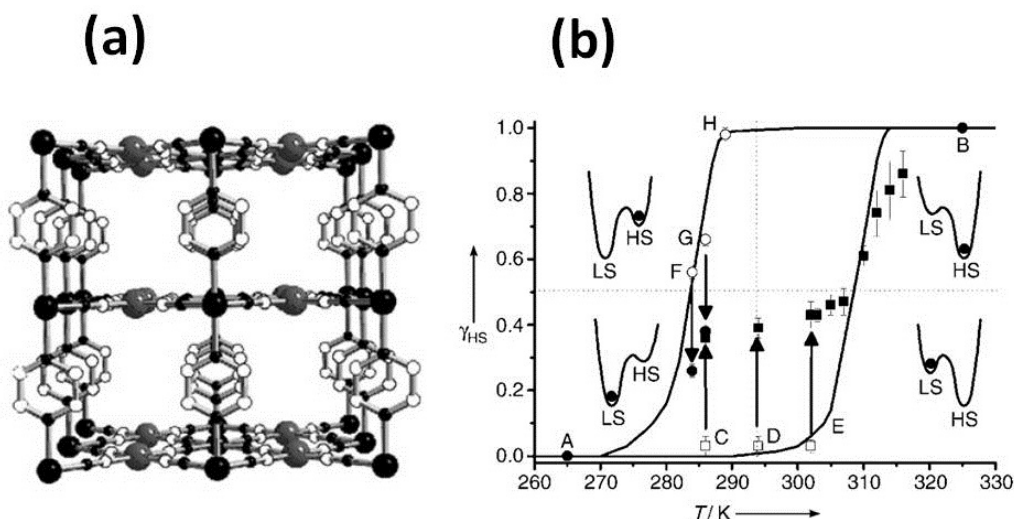
Figure 1.9: (a) Schematic structure of the [$Fe(pyrazine)Pt(CN)_4$] and (b) proportion of HS $Fe(II)$ ions after irradiation with nanosecond laser pulses on points A-H of the hysteresis loop [53]
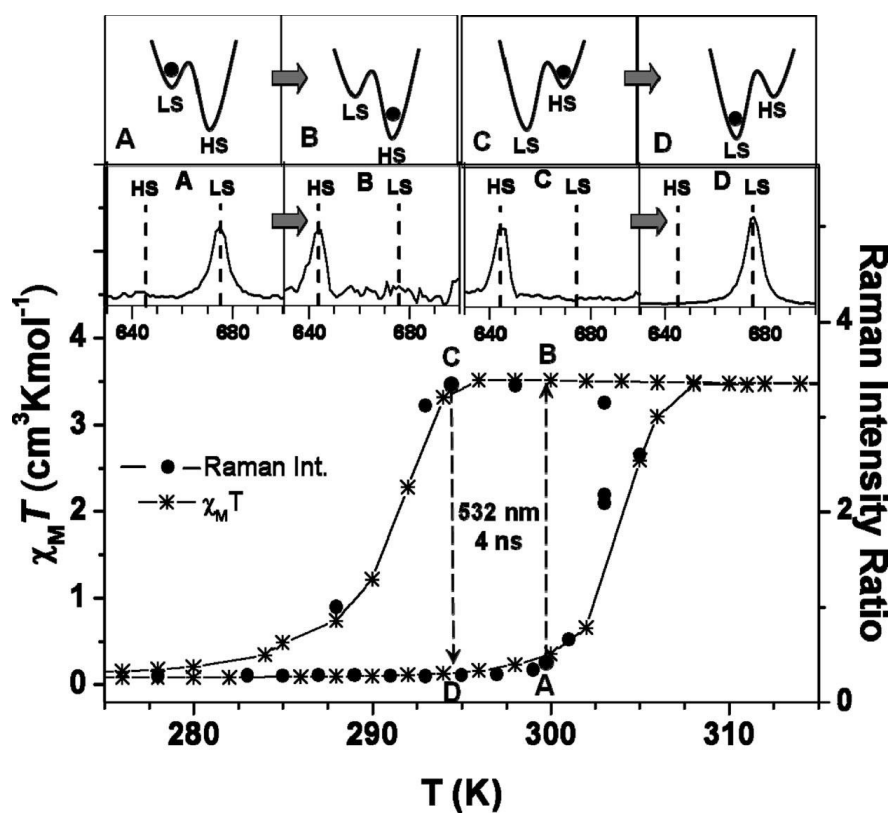
Figure 1.10: Thermal hysteresis loop of magnetic susceptibility, inset of schematic energy diagrams and Raman spectra in the defined points [54]

1.1.5 Detection of the spin transition

Optical measurements

Due to the fact that the bond lengths and bond angles varies between LS and HS states, the optical properties, namely the refractive index changes significantly. In addition the electronic structure change implies also a color change on the SCO. For many Fe(II) complexes, the change in color is from pink at low temperatures (LS state) to white at high temperatures (HS state) as illustrated in Figure 1.11.The setup for optical measurements is simple and can be done either in transmission or reflection modes.
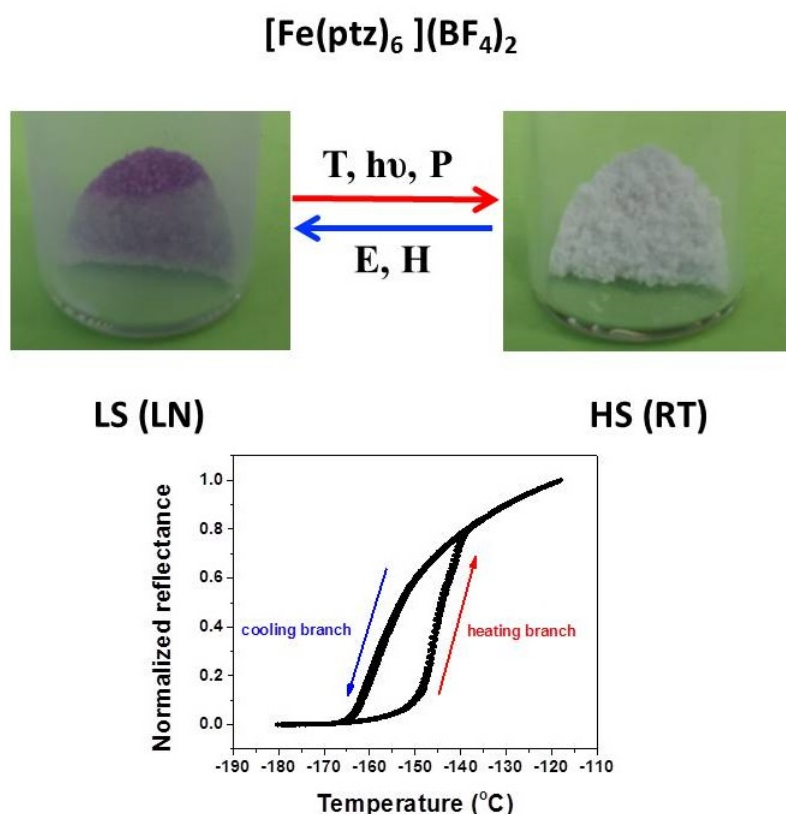
Figure 1.11: Color change in $[Fe(ptz)_6](BF_4)_2$ SCO compound. The LS state is dark purple at liquid nitrogen temperature and the HS state is white at room temperature.

Reflectance measurements are merely qualitative, meaning it will not provide the residual fraction of molecules that are switching from one state to another, however it will give information on the transition temperatures of the considered sample. Usually a filter is used to increase the contrast between the LS state and the HS state. Still, it has been shown that the wavelength of the filter can influence the shape of the hysteresis loop [56, 57].
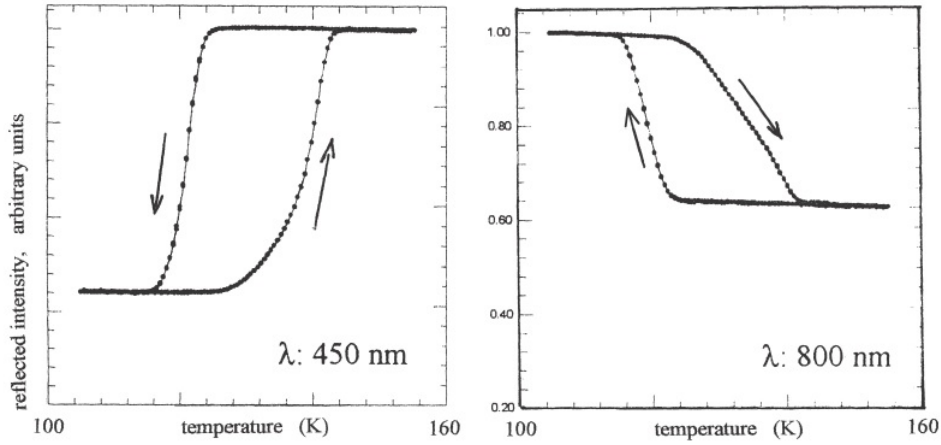
Figure 1.12: Thermal hysteresis loops of $[Fe_{0.64}Co_{0.36}(btr)_2(NCS)_2] \cdot H_2O$, observed by optical reflectivity at two different wavelengths [55].

The difference in the shape of the hysteresis loops is explained by Varret et al. [56] by the fact that at a wavelength of $\lambda = 450$ nm the thermal hysteresis registered is characteristic to the surface of the sample whilst the hysteresis loop registered at $\lambda = 800$ nm is characteristic of the bulk material. The reflectivity measurements are mainly used to confirm the existence of SCO phenomenon and the corresponding transition temperature(s) due to its simplicity and the speed of this method. Another technique used to quantitatively measure the optical density of a SCO materials is based on the transmission geometry. In order to obtain the absolute values of the optical density change due to SCO, the measurement can be performed only on high quality single crystals [58] or thin films [59].

Magnetic measurements

Magnetic measurements as a function of temperature are used to determine the change in the material from a strongly paramagnetic HS state to a weaker paramagnetic or diamagnetic (in case of Fe(II) and Co(III)) LS state. For solid samples, the χT product is determined using a superconducting quantum interface magnetometer (SQUID) and represents of a mixture of temperature dependent contributions of χ_{HS} and χ_{LS} as follows:

$$\chi(T) = \gamma_{HS}\chi_{HS} + (1 - \gamma_{HS})\chi_{LS} \tag{1.7}$$

With the known susceptibilities of both LS and HS states (χ_{LS} and χ_{HS} respectively) the transition curves are plotted as $\gamma_{HS}(T)$. In the case where the susceptibilities of LS and HS states are not well known or not accessible the χT vs. T plot is used. Also the magnetic moment can be determined using the following equation:

$$\mu_{eff} = (8\chi T)^{1/2} \tag{1.8}$$

Figure 1.13 presents different SCO curves as a function of temperature. In the left image the transition curve for $[Fe(dpa)(NCS)_2]_2bpym$ SCO complex is shown [60], with a gradual conversion between 50 K and 350 K making it suitable for temperature sensors [61]. The middle image illustrates a more exotic transition curve, namely two step transition for $[FeL_2][BF_4]_2 \cdot xH_2O$ [43]. The third thermal cycle presents a transition with hysteresis effect for $[Fe(Htrz)_{2.85}(NH_2trz)_{0.15}](ClO_4)_2$ [62] suitable for data storage applications.

15
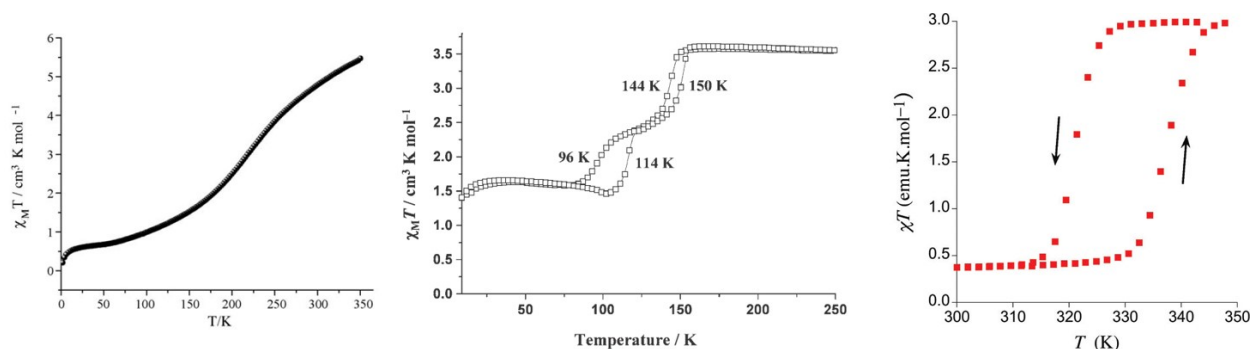
Figure 1.13: $\chi T\ vs.\ T$ plots for various SCO compounds [59-61].

Calorimetric measurements

Calorimetric measurements (most often Differential Scanning Calorimetry - DSC) are used to determine the changes in the heat capacity of the material under study, or in a more simple manner the enthalpy changes associated with the SCO. Due to the fact that that the reversible spin transition is entropy driven, calorimetric measurements are employed to determine entropy S and enthalpy H changes from the Gibbs equation:

$$\Delta G = \Delta H - T\,\Delta S \tag{1.9}$$

A typical calorimetric curve registered on a SCO compound in both heating and cooling mode is presented in Figure 1.14 where transition temperatures are visible as maxima [63]. It can be seen that the material presents a narrow thermal hysteresis.
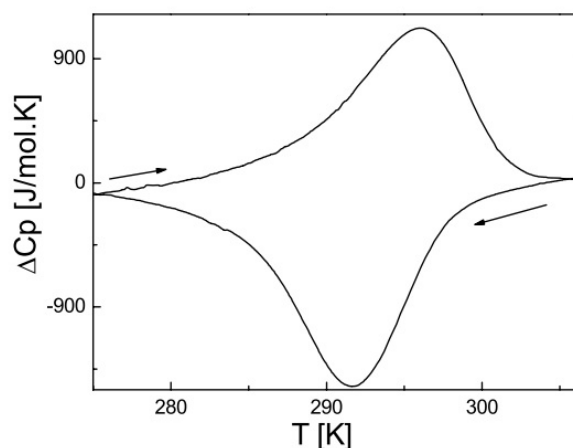
Figure 1.14: Typical calorimetric curve registered on [$Fe(Ethyl - 4H - 1, 2, 4 - triazole - 4 - yl - acetate)_3](ClO_4)_2$ [62].

Spectroscopic investigations

Among the different techniques (vibrational, electronic, X-ray, EPR, etc.), two of the most common spectroscopic investigations used for SCO compounds are Raman and ^{57}Fe Mössbauer spectroscopies. These techniques give information about the current spin state of the compound and the residual fractions in any given spin state.

In the case of Raman spectroscopy (schematic illustration of the experimental setup in Figure 1.15 [64]), the increase in metal-ligand bond lengths from LS to HS states is

accompanied by a lowering of the frequencies of the lattice vibrations. The most important changes generally occur between 250 cm^{-1} and 500 cm^{-1} [39], where different markers that indicate the spin state can be found. An example of such spectra in both LS and HS states for the $[Fe(Htrz)_2(trz)](BF_4)$ complex is presented in Figure 1.16. The characteristic markers of this complex are found, as reported in [65], around 135, 197, 211, 285 and 299 cm^{-1} for the LS state and 105, 136, 150 (shoulder), 180 and 190 cm^{-1} in HS state.
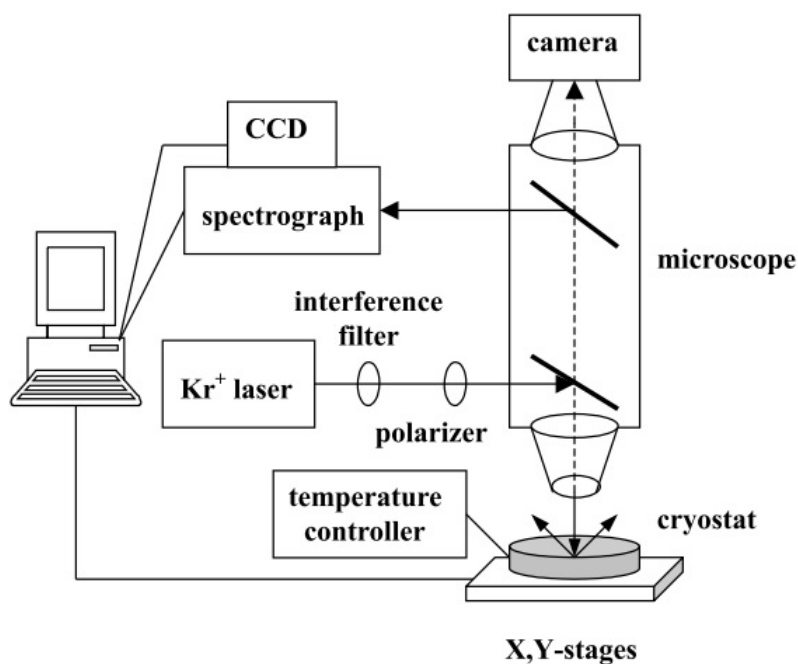
Figure 1.15: General diagram for Raman spectroscopy setup [63].
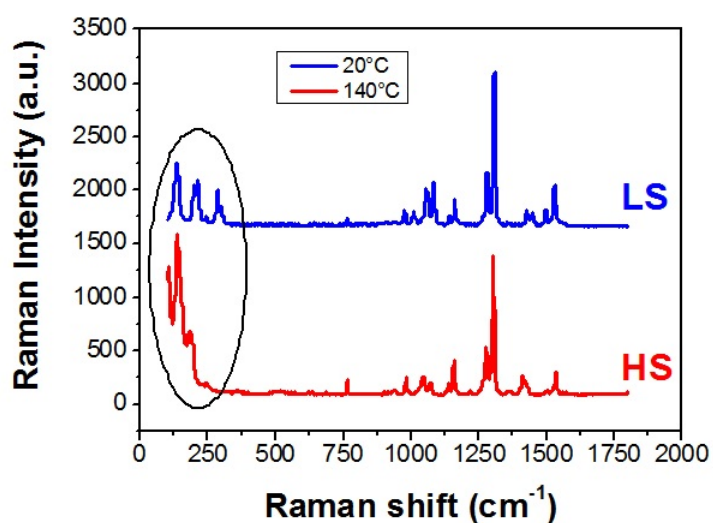
Figure 1.16: Raman spectra of the $[Fe(Htrz)_2(trz)](BF_4)$ SCO compound in the LS and HS states.

If the Raman spectra is recorded at different temperatures and the normalized fractions of specific markers are taken into account, the spin crossover thermal cycle (thermal hysteresis) can be built [66] as illustrated in the figure below. In the presented case the markers were considered at 1014 cm^{-1} and 1028 cm^{-1} ($I_{1014}/(I_{1014} + I_{1028})$) for the HS and LS states respectively.
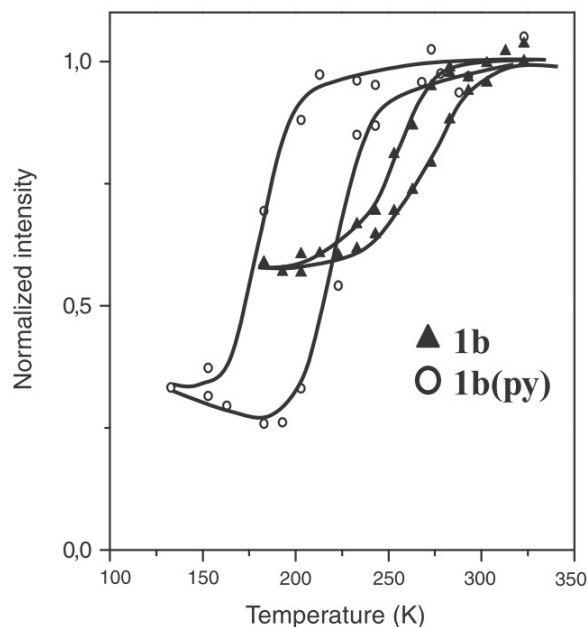
Figure 1.17: Temperature dependence of Raman intensity ratio for the desolvated form of $Fe(bpac)[Pt(CN)_4]$ (1b) and the pyridine doped form (1bpy) [65].

Raman spectroscopy has been also used to follow the SCO when registering the pressure dependency of the spin transition at fixed temperature [67] (Figure 1.18). This measurement has been made on a sample inside a pressure cell, being the only method (besides infrared spectroscopy) of assessing the change in vibrational entropy as a function of pressure [68].
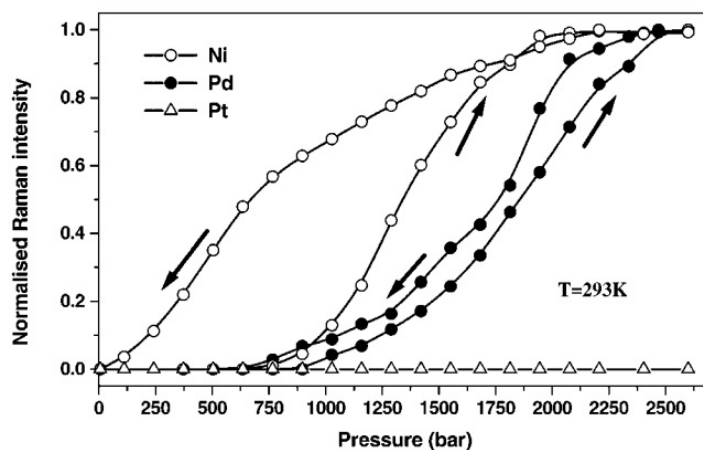
Figure 1.18: Pressure induced spin transition curves of $Fe(pyrazine)[X(CN)_4]$, where $X = Ni$, Pd, or Pt [66].

With the discovery of spin transition in Fe complexes, a new technique proved useful in the study of temperature and pressure induced spin crossover, namely ^{57}Fe Mössbauer spectroscopy.
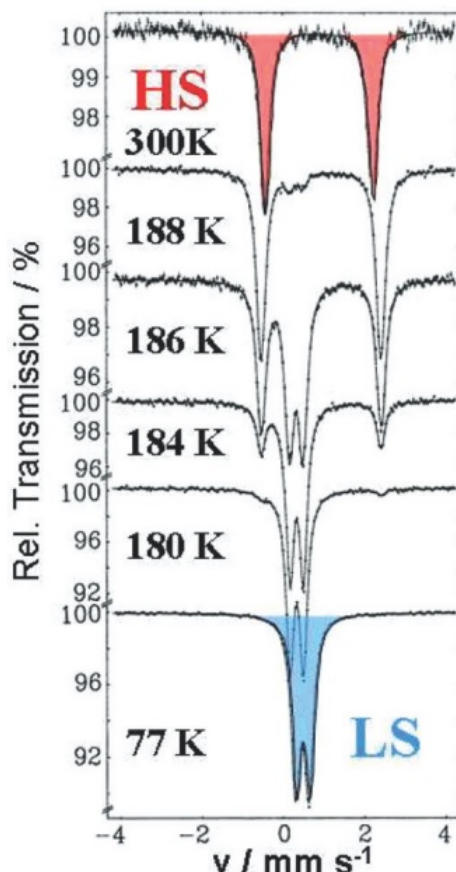
Figure 1.19: Mössbauer spectra of $[Fe(phen)_2(NCS)_2]$ at different temperatures [68].

^{57}Fe Mössbauer spectroscopy is used to study oxidation and spin states of iron in coordination compounds based on recoilless nuclear resonance absorption of γ radiation. When recording the corresponding spectra for LS and HS states there is a significant change in two important parameters. Figure 1.19 [69] illustrates the Mössbauer spectra for LS (at $77\,K$) and HS (at $300\,K$) states, as well as intermediary spectra for the $[Fe(phen)_2(NCS)_2]$ SCO complex. The two parameters taken into account are the isomer shift δ, which refers to the position of the baricenter of the absorption peak, and the quadrupole splitting ΔE_Q, which is the distance between the maxima of the two peaks of the dublet. The quadrupole doublet observed in the HS state presents a larger splitting and higher δ than the LS state, which is typical for $Fe(II)$.

Crystallographic investigations

Another technique used to determine the nature of the spin transition is the variable temperature X-ray structural studies. This method exploits the change in metal-ligand bond length due to spin transition. X-ray structural studies can be made on single crystals as well as powder samples, and can reveal the nature of the spin transition (gradual or abrupt) as well as the volume change by following the changes in the lattice parameters [70, 71].

1.2 State of the art in charge transport and electrical properties of SCO materials

1.2.1 Macroscopic samples

The first report on the thermal bistability in the (quasi-static) dielectric constant, i.e. the relative permittivity, as a consequence of the reversible LS↔HS transition was presented in 2003 by Bousseksou et al. for a series of spin crossover materials [24]. Figure 1.20 shows the thermal hysteresis of the dielectric constant associated with the spin transition for the $[Fe(NH_2trz)_3](NO_3)_2$, $Fe[5NO_2$-sal-N(1,4,7,10)] and $Fe_{0.8}Ni_{0.2}(btr)_2(NCS)_2 \cdot H_2O$ spin crossover compounds, together with the associated thermal variation of the proportion of the HS molecules measured through magnetic susceptibility and reflectivity measurements. The change in dielectric constant upon the spin transition is due to a large change in electronic polarizabilities caused by the concomitant effect of electronic structure change and local symmetry distortion. Interestingly, it can go both ways: the dielectric constant of the HS state can be either superior (more frequent) or inferior to that of the LS state [24, 72]. The transition temperatures measured through dielectric techniques follow the values found by other well-known methods to study the SCO phenomena (magnetic susceptibility and optical measurements). Moreover, these temperatures are independent of the frequency of the applied field (up to at least 1 MHz), which is characteristic of a system in absence of electron transfer.
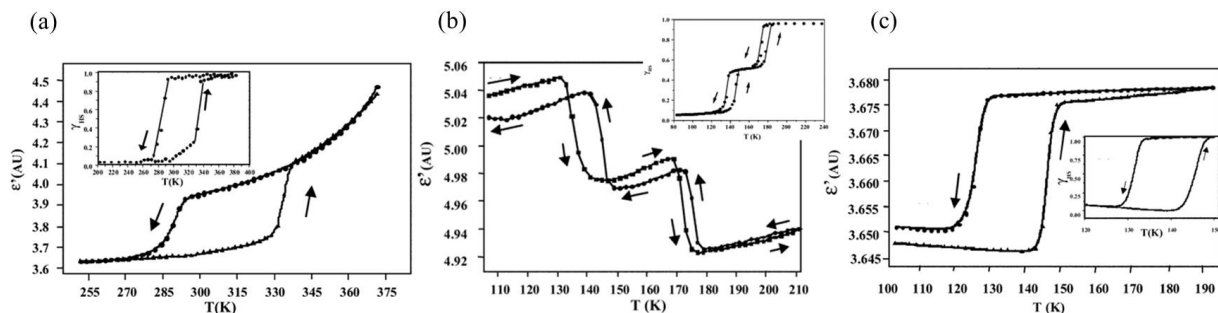
Figure 1.20: Thermal hysteresis of the dielectric constant associated with the spin transition for (a) $[Fe(NH_2trz)_3](NO_3)_2$, (b) $Fe[5NO_2 - sal - N(1, 4, 7, 10)]$ and (c) $Fe_{0.8}Ni_{0.2}(btr)_2(NCS)_2 \cdot H2O$ spin crossover compounds. The insets illustrate the thermal variation of the proportion of the HS molecules measured trough (a) and (b) magnetic susceptibility and (c) optical reflectivity measurements [24].

Later, in 2006 Bonhommeau et al. [25] showed the possibility of switching the dielectric constant of $[Fe(L)(CN)_2] \cdot H_2O$ by light irradiation (where L is a Schiff base macrocyclic ligand). The switching of a SCO material using light involves quantitative trapping of the molecules in the excited HS state (light induced excited spin state trapping, LIESST), which can remain in the metastable state for several days at low temperatures (usually below 50 K). The corresponding change in dielectric constant was attributed, based on density functional theory (DFT) calculations, to different polarizabilities in the LS and the HS states caused by the structural modifications which accompany the spin transition.

The change of the dielectric constant of SCO materials provides perspectives towards the use of these materials in micro/nanoelectronic devices, for example in capacitive memory devices. Nevertheless one must note that the absolute values of the dielectric constant
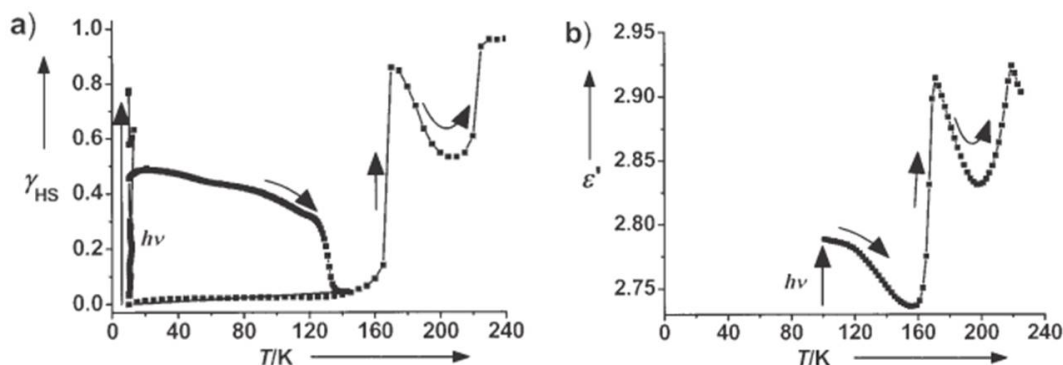
Figure 1.21: (a) LIESST effect performed at 10 K and thermal variation of the HS fraction measured through magnetic susceptibility. (b) Thermal and light induced permittivity switching performed at 100 K for $[Fe(L)(CN)_2]H_2O$ complex [25].

remain moderate in these compounds and the reported changes on the SCO are usually not very high (from a few percent to a few tens of percent).

From a practical point of view the switching of the electrical conductivity represents also an interesting scope. The first report on the conductivity switching of a bulk SCO solid was published in 2009 [29]. In this work, Salmon et al. re-investigated the spin crossover phenomenon in the [Fe(HB(pz)3)2] (pz = pyrazolyl) complex by magnetic, calorimetric, optical, crystallographic and electrical means. The magnetic and optical properties revealed irreversible phenomena occurring at the LS to HS transition upon the first heating. This effect has been attributed to a crystallographic change from tetragonal to monoclinic structure. For further cycling the magnetic moment displayed a reproducible gradual variation between ca. 290 K (LS) and 450 K (HS) as illustrated in Figure 1.22.
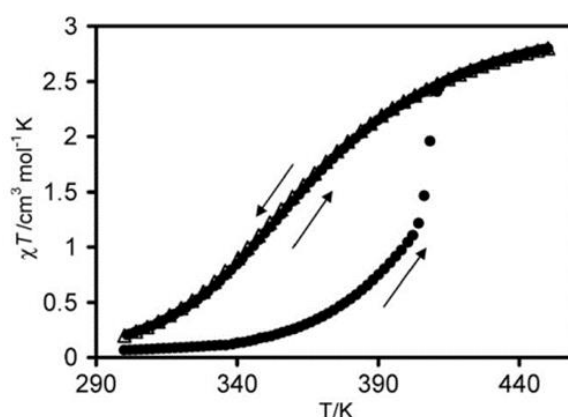
Figure 1.22: χ_M vs. T plot for $[Fe(HB(pz)_3)_2]$ SCO complex. First cycle is represented with closed circles and second cycle with open triangles [29].

Using a broadband dielectric spectrometer the complex conductivity of the sample was also recorded over two consecutive thermal cycles and the irreversible character of the first (magneto-structural) transition was clearly evidenced in the electrical measurements around 410 K where an abrupt, ca. 3 orders of magnitude decrease in conductivity was registered (Figure 1.23). The next thermal cycle followed exactly the conductivity variation of the first cooling curve. Charge hopping process has been proposed as the main transport mechanism for this material with the LS state being more conductive. In the case
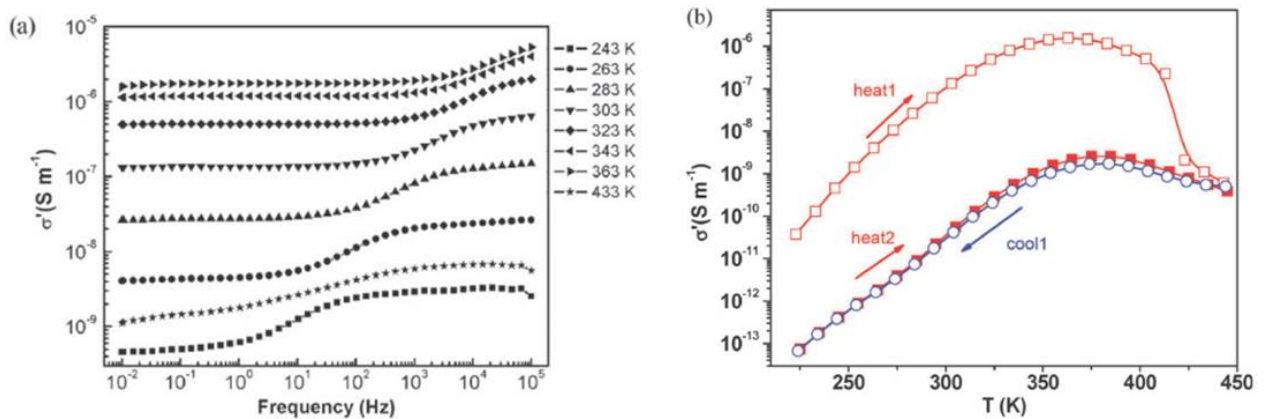
Figure 1.23: (a) Frequency dependency of the real part of ac conductivity of the $[Fe(HB(pz)_3)_2]$ complex, recorded between 243 K and 433 K during the first heating. (b) Temperature dependence of the real part of the ac conductivity recorded after two successive thermal cycles for the $[Fe(HB(pz)_3)_2]$ complex [29].

of $[Fe(HB(pz)_3)_2]$ the analysis of electrical properties was complicated by the simultaneous electronic, crystallographic and morphologic transformations of the sample.

A more clear-cut situation is presented by the spin-state dependence of the electrical conductivity of the $[Fe(Htrz)_2(trz)](BF_4)$ (Htrz = 1H-1,2,4-triazole) SCO compound [31]. Different synthesis batches of this complex were analyzed and each sample presented a spin transition with wide hysteresis loops above room temperature, with slightly different transition temperatures depending on their morphology. DC electrical measurements were performed on the powders compacted between two stainless steel electrodes. The conductivity of the samples was rather low, typically between 10^{-8} and 10^{-10} S/cm at room temperature. The electrical conductivity plotted as a function of temperature revealed a clear hysteresis loop for each sample with transition temperatures that correspond to the values found by optical reflectivity measurements. Figure 1.24 shows an example where a strong thermal activation of the conductivity is observed in the heating mode (LS state) followed by an abrupt (reversible) drop of ca. 2 orders of magnitude around 372 K, corresponding to the $LS \leftrightarrow HS$ transition.Even if the samples were found systematically more conductive in the LS state, the analysis of thermal activation energies suggested that in some circumstances the opposite behavior might be also expected to occur. The low conductivity and strong thermal activation indicate that the charge transport takes place through a polaron hopping process. In this framework, the change in conductivity upon the spin transition was attributed to a modification of the vibrational frequencies. Indeed, the LS to HS transition is accompanied by a decrease in the phonon frequencies, which is expected to result in a lower charge carrier hopping rate.

Overall, bulk SCO solids can be considered as nearly perfect (i.e. low loss) dielectric materials characterized by very low conductivity values. It is thus not surprising that the conductivity changes associated with the SCO have been observed only in samples with spin transitions above room temperature, where the thermal activation allows for raising the conductivity to detectable levels. To overcome this problem several groups attempted to enhance charge transport in SCO compounds by synthesizing hybrid materials comprising both SCO and conducting bricks. This has been achieved both at the microscopic and macroscopic levels.

Hybrid materials containing SCO complexes as well as conducting molecular species
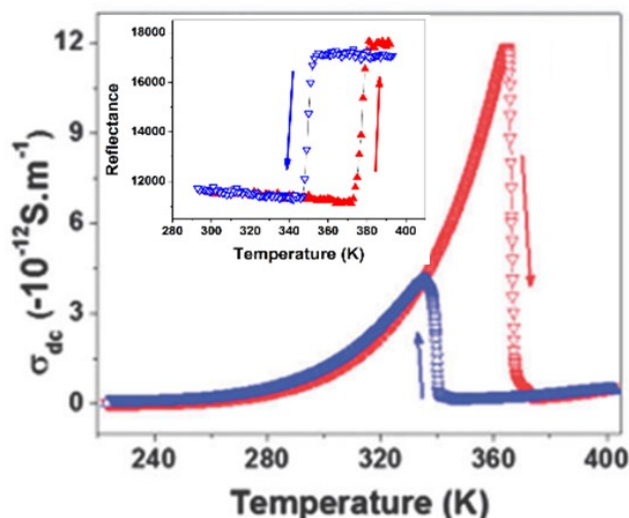
Figure 1.24: Temperature dependence of the dc conductivity in the heating and cooling modes for the $[Fe(Htrz)_2(trz)](BF_4)$ sample. The inset shows the temperature dependence of the high spin fraction [31].

in the same crystal lattice were reported by several teams [26–28, 73–82]. Most of these compounds exhibit either SCO or semiconducting behavior or both in the same time, but (in our opinion) a clearly discernible interplay between the two phenomena has been achieved only in two cases. The first indication of an interplay between the two phenomena were reported in 2006 by Takahashi et al. [27]. They synthesized and characterized the $[Fe(qsal)_2][Ni(dmit)_2]_3 \cdot CH_3CN \cdot H_2O$ complex (qsalH = N-(8-quinolyl)-salicylaldimine, dmit = 4,5-dithiolato-1,3-dithiole-2-thione), which presents a gradual spin conversion from room temperature to 120 K in a multi-step process. The electrical resistivity behavior as a function of temperature is characteristic to a semiconductor, with a relatively high value at room temperature (2 S/cm) and presents a hysteresis loop between 90 and 120 K similar to the magnetic measurements. A correlation appears thus between the SCO phenomenon and the electrical conduction, but the complicated temperature dependence of the spin crossover and the lack of structural characterization did not allow for an unambiguous conclusion. A more clear-cut result was later obtained by the same group [81] with the compound $[Fe(qnal)_2][Pd(dmit)_2]_5 \cdot$acetone [qnalH=N-(8-quinolyl)-2-hydroxy-1-naphthaldimine]. This compound displayed a quasi-complete spin transition around 220 K as shown by the magnetic measurements in Figure 1.25a. The electrical measurements revealed a rather high conductivity value at room temperature (ca. 10^{-2} S/cm), and even more importantly a discontinuity was observed in the temperature dependence of the resistivity around 220 K, which is in the same range as the spin transition. The activation energy before the resistivity change is 0.37 eV (LS state), while after the "anomaly" the activation energy is 0.24 eV (HS state). Looking at the temperature dependence of the cell parameters shown in Figure 1.25b, a significant change at 220 K can be observed for the a axis. The authors suggested this uniaxial strain might be the origin of the conductance switching upon the SCO.

A similar result was obtained by Nihei et al. [28] by mixing Fe(II) SCO complexes with tetrathiafulvalene conductive moieties. They synthesized and characterized the compounds $[Fe(dppTTF)_2](BPh_4)_2 \cdot MeNO_2 \cdot 0.5Et_2O$ and $[Fe(dppTTF)_2][Ni(mnt)_2]_2(BF_4) \cdot PhCN$ (dppTTF = 1-2-(1,3-dithiol-2ylinene)-1,3-dithiolyl-2-2,6-bis(1-pyrazolyl)pyridyl-

ethylene, mnt = maleonitriledithiolate). The magnetic susceptibility measurement of the second compound is presented in Figure 1.26, wherein a spin crossover around 250 K can be depicted. The electrical measurements performed on a single crystal revealed a rather high conductivity of ca. 10^{-3} S/cm at, room temperature and a change in the R vs. T slope between 160 K and 280 K, which correspond to the spin crossover region of the complex. In the low temperature region (LS), the activation energy was measured to be 129 meV, while in the high temperature region (HS) the activation energy is 119 meV.
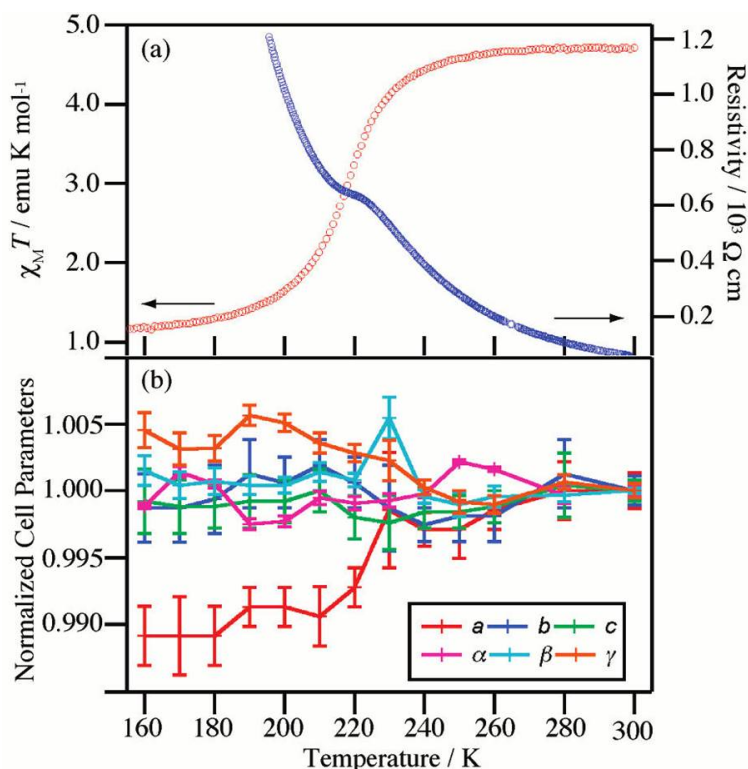
Figure 1.25: Temperature dependence of (a) the $\chi_M \cdot T$ product and resistivity and (b) the cell parameters normalized at 300 K [28].

In the previous examples hybrid conducting SCO materials were synthesized by co-crystallization of molecular bricks. This elegant approach offers very interesting prospects from a fundamental point of view, but the synthesis of these compounds is rather challenging. On the other hand, hybrid materials were also obtained at a more macroscopic level by "physically mixing" the constituents. A remarkable synergy between a SCO complex and a piezoresistive polymer has been reported by Koo et al. [83] by studying the response of a composite consisting of polypyrrole (ppy) and $[Fe(Htrz)_2(trz)]BF_4$ and/or $[Fe(NH_2 - trz)3]SO_4$ (NH2-trz = 4-amino-1,2,4-triazole). The composites have been prepared by mixing ppy and the bulk SCO material(s), then pressing at 0.01 GPa to obtain films with thickness greater than 0.5 mm. Electrical measurements were performed using the four probe technique and revealed room temperature conductivity of ca. 10^{-2} S/cm. The conductivity as a function of temperature reveals the same hysteresis loop as the magnetic measurements (Figure 1.27). The HS state is ca. 60 % more conducting in this sample. In a similar composite containing both $[Fe(NH_2 - trz)_3][SO_4]$ and $[Fe(Htrz)_2(trz)][BF_4]$ complexes, the system presents multiple thermal hysteresis and a relative conductivity change as high as 300 %. Doped ppy is a highly conductive polymer and, more importantly, it has piezoresistive properties, i.e. its conductivity changes by applying a pressure. In this case it
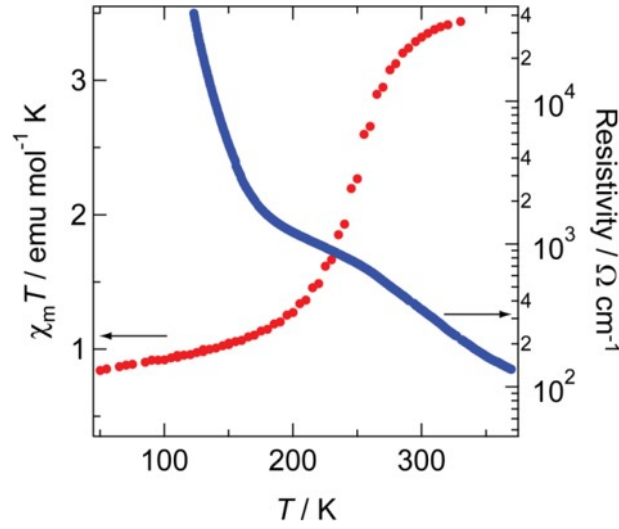
Figure 1.26: Temperature dependence of the magnetic susceptibility and resistivity of $[Fe(dppTTF)2][Ni(mnt)_2]_2(BF_4) \cdot PhCN$ [28].

is assumed that the pressure originates from the mechanical stress and strain associated with the spin transition. (The volumetric stain due to SCO is ca. 0.11 in $[Fe(Htrz)_2(trz)]BF_4$.) These results provide important perspectives for obtaining highly conductive plastic films with switching properties at technologically relevant temperatures. We anticipate interesting developments in this direction by developing synergy between SCO and polymer materials with various electrical properties and promising new functionalities. In particular electro-active polymers are very appealing for the development of SCO-based actuators [23, 84, 85].
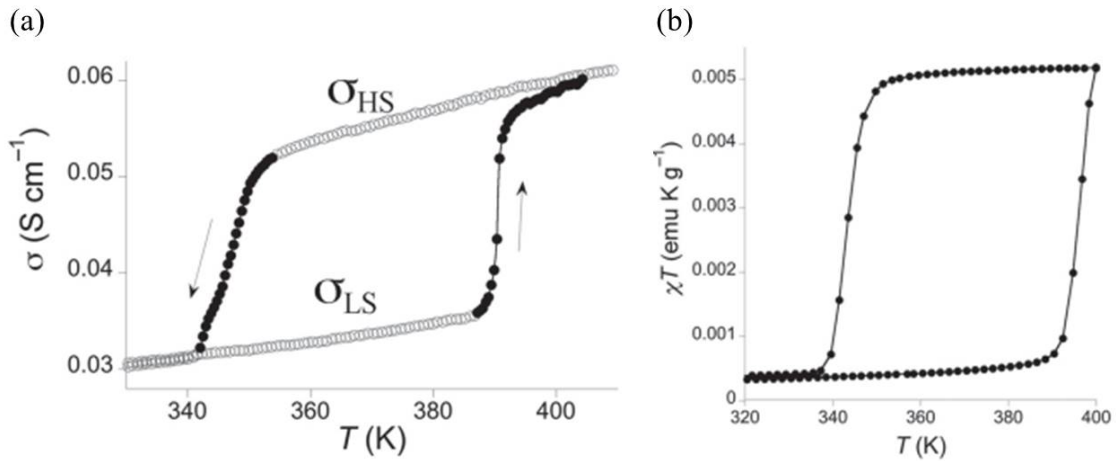
Figure 1.27: Temperature dependence of (a) the electrical conductivity and (b) the magnetic properties of a composite consisting of polypyrrole and $[Fe(Htrz)_2(trz)][BF_4]$ [82].

Hybrid conducting SCO materials have been also fabricated at a truly macroscopic level, by combining SCO polymer composites with electroactive polymers in bilayer structures [84, 85]. Chen et al. [84] achieved electrical bistability using a bilayer cantilever consisting of a $[Fe(Htrz)_2(trz)](BF_4)$/polycarbonate (PC) composite and a polyimide/constantan alloy/polyimide strain sensitive plate (Figure 1.28). The temperature dependence of the

voltage measured through a Wheatstone bridge presented a hysteresis loop characteristic to the spin transition. It is clear that the measured voltage is related to the metallic conductor not to the SCO/PC composite, however the SCO phenomena is clearly visible through mechanical coupling between the two polymer layers. On the other way around, Guralskiy et al. [85] described an electro-thermomechanical actuator, which consists in a bilayer cantilever combining [Fe(Htrz)2(trz)](BF4) with poly(methylmethacrylate) (PMMA) for the first layer and a polymer composite with silver nanoparticles for the second layer. This bilayer cantilever uses the spin crossover phenomenon to convert electrical energy into mechanical motion through Joule heating.
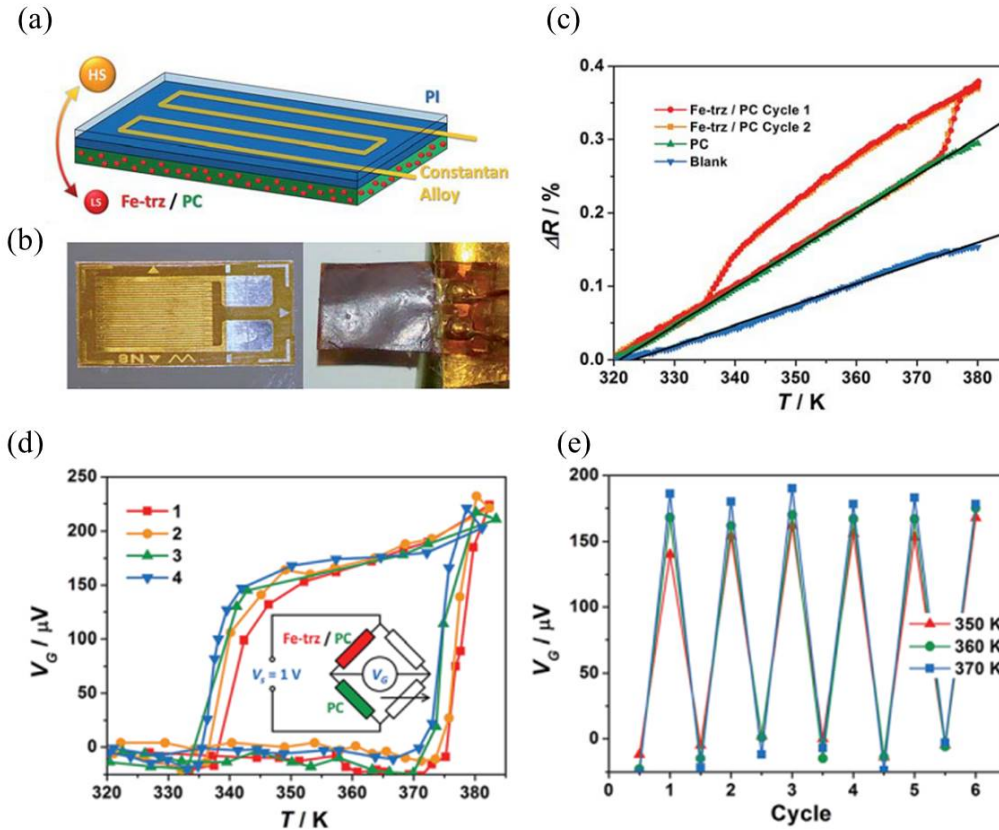
Figure 1.28: (a) Schematic representation of the SCO/PC heterostructure. (b) Experimental device before and after SCO/PC composite deposition. (c) Normalized temperature-dependent electrical resistance of the heterostructure, chosen compensator (PC) and blank plate. (d) Thermal hysteresis cycles recorded from Wheatstone bridge. (e) Recorded voltages at various temperatures during several consecutive thermal cycles [83].

1.2.2 Micro- and nanoscale devices

Spin crossover thin films and nanoparticles have been integrated recently into electronic devices either to investigate the charge transport properties of the SCO compounds and/or to obtain new device functionalities (switch, memory, etc). Matsuda et al. used spin crossover materials to modulate the electroluminescence (EL) of an OLED device ITO/[$Fe(dpp)_2$](BF_4)$_2$:Chl-a/Al (dpp=2,6-di(pyrazol-1-yl)pyridine), Chl-a = chlorophyll a). The fluorescent SCO layer was deposited by spin coating on ITO and covered by a thin Al layer in a vertical device configuration. The device presented EL in the HS state,

while in the LS state the EL was suppressed as shown in Figure 1.29 [86]. The authors proposed a model where in the LS state the electrons injected from the Al electrode passed through the SCO complex into the ITO electrode, preventing the formation of excited-state Chl-a. [22].
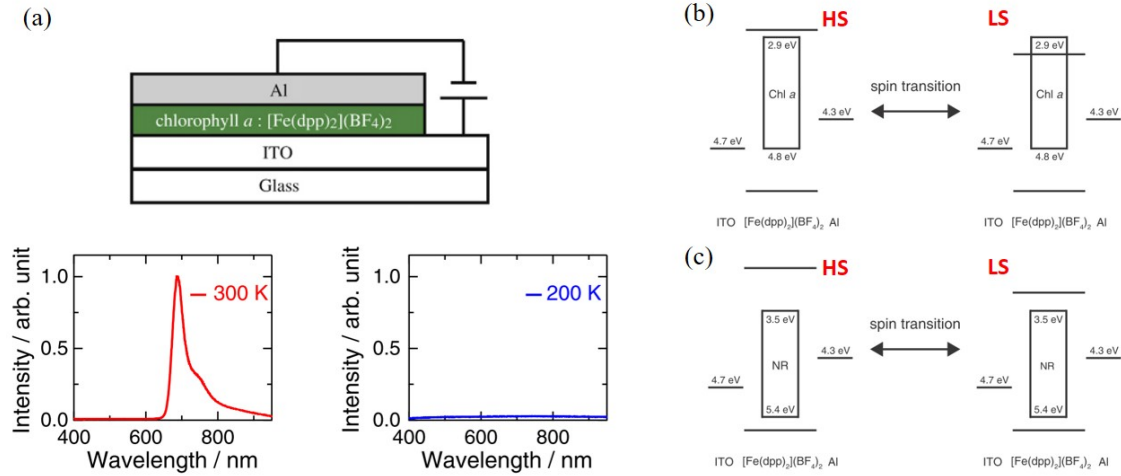
Figure 1.29: (a) Scheme of the OLED device ITO/[$Fe(dpp)_2$](BF_4)$_2$:Chl-a/Al and its electroluminescence intensity in the HS and LS states. (b) Schematic representation of the mechanism proposed for the switching of EL intensity upon SCO. (c) Energy level diagram for an analog device with NR dye [86].

On the other hand, when the SCO material is in the HS state, the electrons and holes combine, therefore EL is registered (Figure 1.29b). In order to test this hypothesis, a poly(N-vinylcarbazole) (PVK) layer was deposited between the ITO electrode and active layer. PVK is used as a hole transport and electron blocking layer. Indeed the insertion of this layer created an accumulation of charges in the active layer and the EL occurred in both spin states. In a second stage of the experiment, the SCO material was doped with nile red (NR) dye as an emitting dopant instead of Chl-a. In this case also, EL was detected in both spin states, which was explained by the lower lying electron transport orbitals in NR vs. Chl-a (Figure 1.29c).
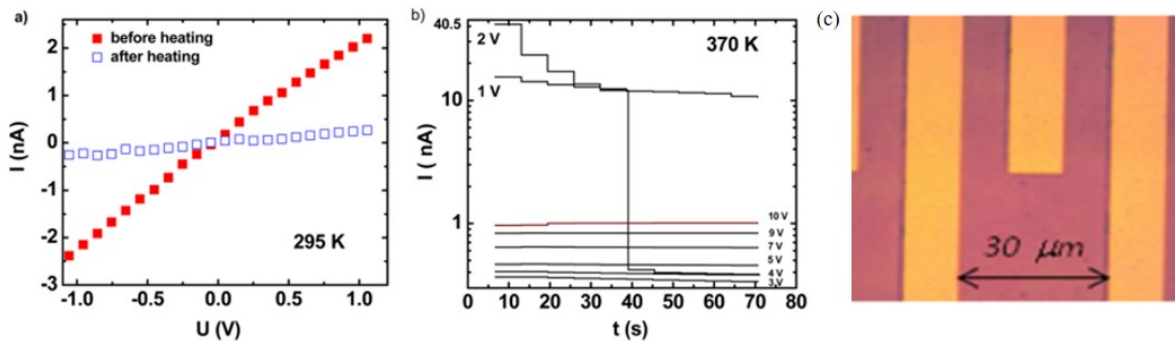
Figure 1.30: (a) Current-voltage characteristic of the ROM device with [$Fe(HB(pz)_3)_2$] recorded at 295 K before and after heating the device to 408 K. (b) Reading and writing process of the ROM device performed at 370 K. (c) Bright field microscopy picture of the micro-electrodes after the deposition of the [$Fe(HB(pz)_3)_2$] film [30].

Mahfoud et al. presented the proof of concept for a read-only memory (ROM) containing the $[Fe(HB(pz)_3)_2]$ SCO complex [30]. In this work the complex has been thermally evaporated in thin film form onto interdigitated microelectrodes. The current-voltage (I-V) characteristic of the device presents an Ohmic variation, before and after heating the device to 408 K (Figure 1.30a). This represent the read operation of the device before and after the writing. An all-electrical read-write process is shown in Figure 1.30b, where different voltage bias has been applied for ca. 1 min to the device at 370 K. When a voltage bias of 1 V was applied no effect occurred. This can be considered as the read operation of the ROM. By increasing the voltage to 2 V the measured current decreases abruptly after 40 s and remains at a very low value. This irreversible effect, attributed to a Joule heating induced structural transition in the material, corresponds to the writing of the memory.

A somewhat similar process was used to fabricate devices with $Fe(phen)_2(NCS)_2$ (phen = 1, 10-phenanthroline) thin films by Shi et al. [87]. The temperature dependence of the magnetic susceptibility of a 280 nm thin film revealed an abrupt spin transition at 175 K, similar to the bulk powder sample (see Figure 1.31). For the electrical characterization a thin film of 240 nm has been deposited between gold electrodes and characterized at room temperature. The logarithmic representation of the I-V curve revealed two linear regions: one region at low voltages with a slope of 1.17, suggesting Ohmic conduction and a second linear region above 1.4 V with a slope of 2.04 characteristic to space charge limited current regime. From these data a charge carrier mobility of 6.53×10^{-6} $cm^2/V \cdot s$ has been deduced. Temperature-dependent transport measurements were not reported, presumably due to the very low current levels around the spin transition temperature.
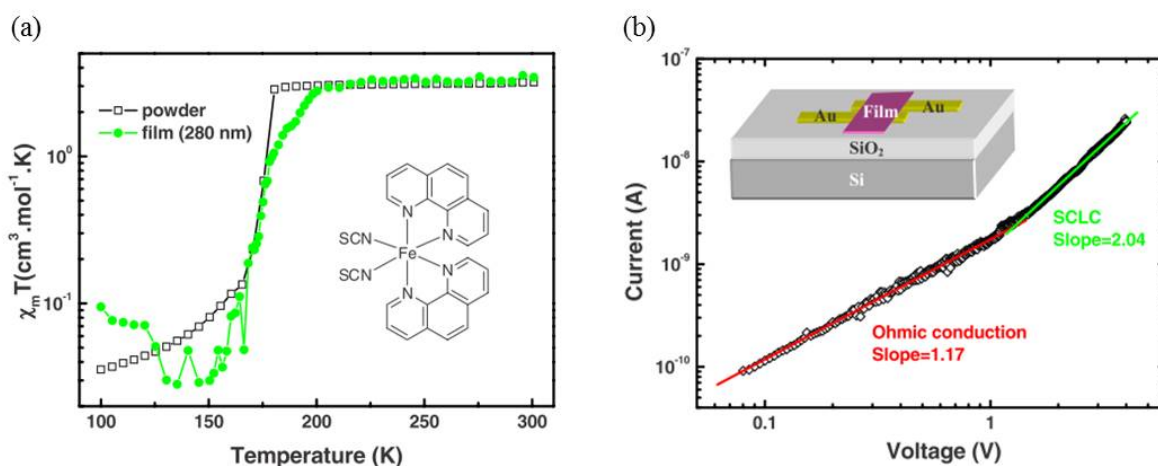
Figure 1.31: (a) $\chi_M \cdot T$ for $Fe(phen)_2(NCS)_2$ powder and 280 nm thin film on silicon substrate. The inset represents a schematic representation of the molecular structure. (b) I-V characteristic of device and linear fit at room temperature. The inset is a schematic representation of the electronic device [86].

The control of the spin state of $[Fe(H_2B(pz)_2)_2(bipy)]$ (where bipy = 2,2'-bipyridine) thin films deposited by thermal evaporation on organic ferroelectric polyvinylidene fluoride with trifluoroethylene (PVDFTrFE) was demonstrated by Zhang et al., by changing the electric field at the interface of the two layers [88]. Magnetometry studies performed on the thin film stack revealed compelling evidence of voltage control of the spin state of the SCO layer. As a reference, the magnetic properties of the SCO powder are depicted in Figure 1.32a, showing the paramagnetic HS state at 300 K and the diamagnetic LS state at 100 K. In the case of the thin films (ca. 25 molecular layer), the paramagnetic

behavior (characteristic to high temperatures) could be measured down to 100 K when the PVDFTrFE film was polarized "up", while the diamagnetic behavior (characteristic to low temperatures) was observed up to room temperature when the ferroelectric film was polarized "down" (Figure 1.32b).
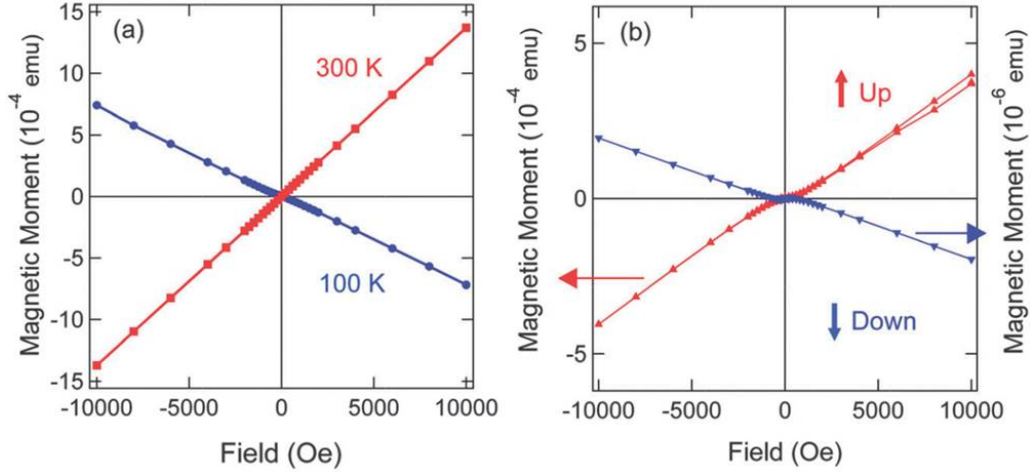
Figure 1.32: (a) Magnetic properties of $[Fe(H_2B(pz)_2)_2(bipy)]$ powder at 100 K (LS) and 300 K (HS). (b) Magnetic properties of the films of $[Fe(H2B(pz)_2)_2(bipy)]$ on the ferroelectric PVDFTrFE substrate for different polarizations [87].
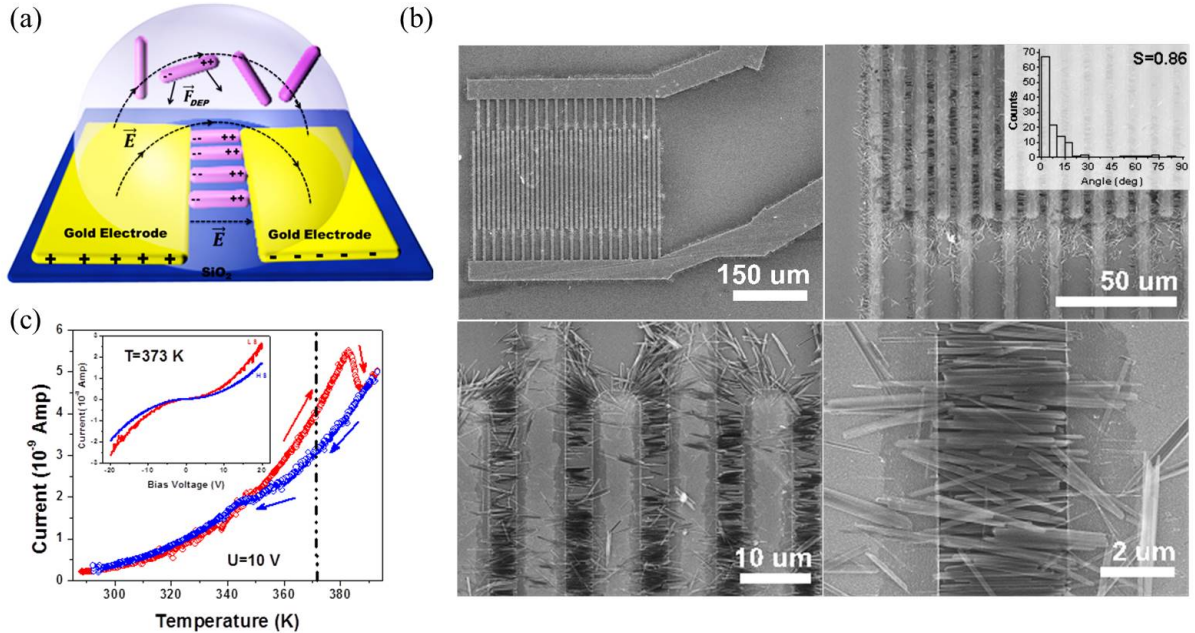
Figure 1.33: (a) Schematic representation of the dielectrophoresis process used to align $[Fe(Htrz)_2(trz)](BF_4)$ particles between electrodes. (b) SEM images of a device with the insert showing the orientation order parameter. (c) Temperature dependence of the measured current in the device over a heating-cooling cycle under 10 V bias. Inset: I-V characteristic recorded at 373 K in the LS and HS states [31].

Rotaru et al. used a different approach wherein micro- and nanoparticles of $[Fe(Htrz)_2(trz)](BF_4)$ have been organized between interdigitated electrodes using dielec-

trophoresis [31]. The particles were dispersed in ethanol and drop-casted on interdigitated gold electrodes. By applying an ac voltage, the electric field gradient induced in the solution attracted the SCO objects to the gaps between electrodes (Figures 1.33a-b). By using high aspect ratio particles the orientation order parameter has been drastically improved, reaching S = 0.86 where $S = < 2cos^2\theta - 1 >$, and θ is the angle between a particular object and the mean orientation of any other object. This value was obtained for particles with 4 μm length and 300 nm in diameter deposited from a 0.2 g/L suspension using 7 V_{rms} and 10 kHz ac bias for dielectrophoresis. The temperature dependence of the measured current (Figure 1.33c) revealed a similar behavior as that obtained for the powder sample (see Figure 1.24a), i.e. the device presents a wide thermal hysteresis loop centered around 370 K with the LS state being more conductive. The I-V characteristics recorded at 373 K in both spin states showed a non-linear behavior, which probably originates in a voltage activation of the charge transport. Overall, fairly similar results were reported later by Dugay et al. [89] for $[Fe(Htrz)_2(trz)](BF_4)$ nanoparticles integrated in a similar device.

Another interesting effect has been observed by Etrillard et al. [32] on the photoconduction in $[Fe(Htrz)_2(trz)](BF_4) \cdot H_2O$ nanocrystals, which have been positioned between sub 100 nm gap gold electrodes. The particles were randomly dispersed on the substrate from an ethanol solution and effectively bridged the gaps between electrodes. A first experiment has been performed on the as-prepared device and no photocurrent has been measured. Then the electrodes were subjected to voltage poling. The current of the poled device increased considerably upon light irradiation and dropped to the same level when the light excitation was removed (Figure 1.34). Even though the experimental results are intriguing, it is not clear if the effect is characteristic of the SCO material.

(a)   (b)
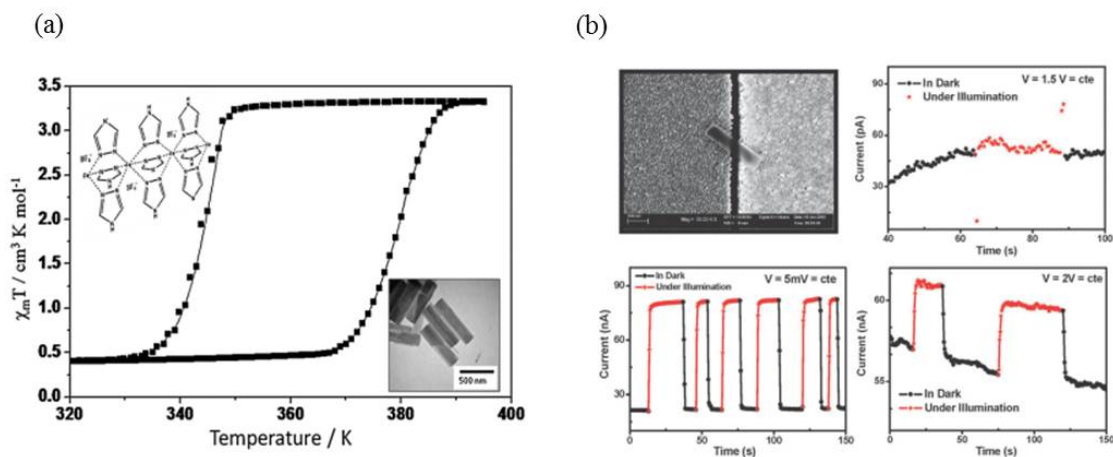
Figure 1.34: (a) Thermal hysteresis loop recorded using magnetic susceptibility measurements of the $[Fe(Htrz)_2(trz)](BF_4) \cdot H_2O$ complex. The insets show the schematic representation of the molecular structure and the TEM micrograph of the obtained nanocrystals. (b) SEM picture of a SCO crystal bridging the electrode gap and the initial experiment showing the absence of photocurrent. In the bottom part of the panel there are two examples of photoconductance after electrode polling [32].

One of the most intriguing results on electrical properties of SCO materials was reported by Prins et al. [35] where they showed the possibility of addressing a SCO nanoparticles. The SCO system is formed of $[Fe(Htrz)_2(trz)][BF_4]$ nanoparticles coated with a surfactant shell. A solution of the particles was deposited between gold electrodes with an electrode gap of 5-10 nm as it is schematically illustrated in Figure 1.35a. The current-

voltage characteristics (Figure 1.35b) show the difference before (green line) and after (red line) particle deposition by a clear increase in the measured current for two different devices (electrode width of 1 μm and 100 nm respectively). Multiple I-V characteristics were recorded at different temperatures in the temperature range of 300-400 K and by plotting the conductance (I/V) of the device at 0.4 V as a function of temperature, a hysteretic behavior similar to the one obtained in the magnetic susceptibility measurements was found (Figure 1.35c). It is important to note that in both devices the conductance in the HS state is several times higher than the conductance in the LS state and the switching between the low-conductance and higher conductance states was also achieved by voltage cycling (Figure 1.35d). The authors suggested that the origin of this conductance difference could be the expansion of the $Fe - N$ bond length that accompanies the spin transition. By assuming a single electron tunneling phenomena in the device, the increase in bond length upon the spin transition can reduce the tunnel barrier width, thus leading to an increase of the conductance.
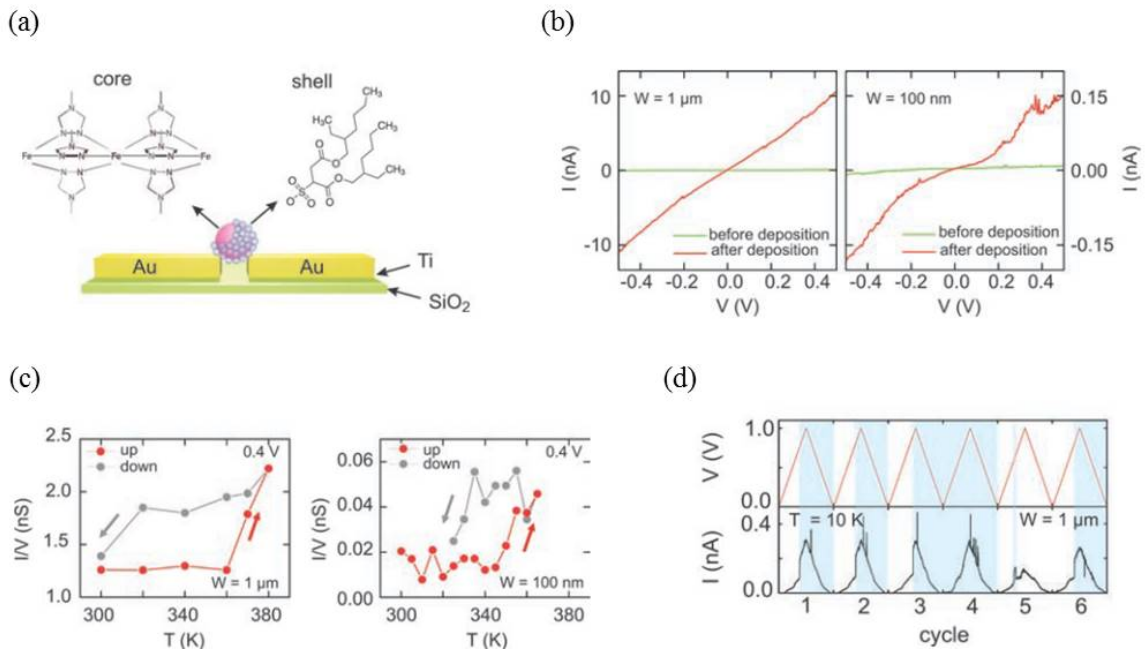
Figure 1.35:   (a) Schematic representation of a device with surfactant coated $[Fe(Htrz)_2(trz)](BF_4)$ nanoparticles in the electrode gap. (b) Current-voltage characteristic of two different devices (with an electrode width of 1 μm and 100 nm respectively) recorded before and after particle deposition. (c) Temperature dependence of the conductance plotted for 0.4 V bias. (d) Conductance switching (1 μm device) using a triangular voltage at 10 K [35].

1.2.3 Single molecule studies

As a matter of fact, the above mentioned work of Prins et al. [35] on single SCO nanoparticles represents an intermediate situation between the investigation of SCO materials and single SCO molecules. These latter have been recently studied by several groups using either scanning tunneling microscopy (STM) or planar, two- or three terminal, "nanogap devices". Working with such single-molecule electronic and spintronic devices is obviously a very attractive and challenging topic. Nevertheless, a word of caution is necessary for the spin crossover community as for the interpretation of the data obtained by these techniques. In most cases there is only indirect evidence for the spin-state switching in these devices. From a fundamental point of view, the mains issue is that the connection of the molecules to the electrodes will always alter to some extent their properties. Hence a direct comparison with the bulk properties becomes often meaningless. From a practical point of view the key problem is that the experimental characterization of the molecule in the junction is nearly impossible by any other means than the tunneling current. From this point of view STM offers somewhat more flexibility than nanogaps, nevertheless, a series of careful control experiments and theoretical calculations are indispensable in each case to rationalize the observations.
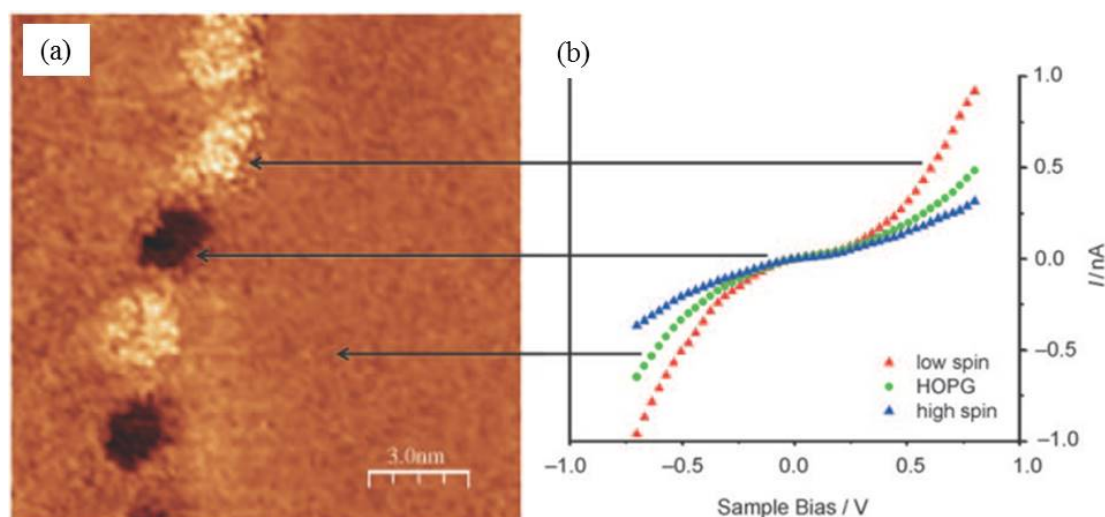
Figure 1.36: (a) CITS current image for a chain of 5 $[Fe^{II}(L)_2](BF_4)_2$ (L = 2,6-di(1H-pyrazol-1-yl)-4-(thiocyanato-methyl)pyridine) molecular clusters in different spin states grafted on HOPG. (b) I-V characteristic for three different positions marked with arrows [33].

The first STM study on a SCO compound was published by Alam et al. [33] who investigated the $[Fe^{II}(L)_2](BF_4)_2$ (L = 2,6-di(1H-pyrazol-1-yl)-4-(thiocyanato-methyl)pyridine) complex (**1**). The compound has been deposited from solution on highly oriented pyrolytic graphite (HOPG) surfaces for current-imaging tunneling spectroscopy (CITS). This technique has been used to map the nanometric chain structures formed on the surface. Two different types of molecular clusters were observed with I-V curves situated either higher or lower than the reference curve of the HOPG surface. The two types of signals were attributed to LS molecules (more conductive) and HS molecules, respectively (see Figure 1.36). The study of $[Fe^{II}(L')_2](X)_2$ complexes was completed later by Grohmann et al. [90]. In this article they studied two complexes with L' = 2,6-di(1H-pyrazol-1-yl)pyridine and X = BF_4 (complex **2**) and X = PF_6 (complex **3**). In bulk polycrystalline form, only

the former exhibits spin crossover, while the latter is a high spin complex. However, the I-V characteristics of both complexes deposited on the HOPG surface present different features, which could be assigned to the coexistence of HS and LS molecules on the surface (see Figure 1.37).
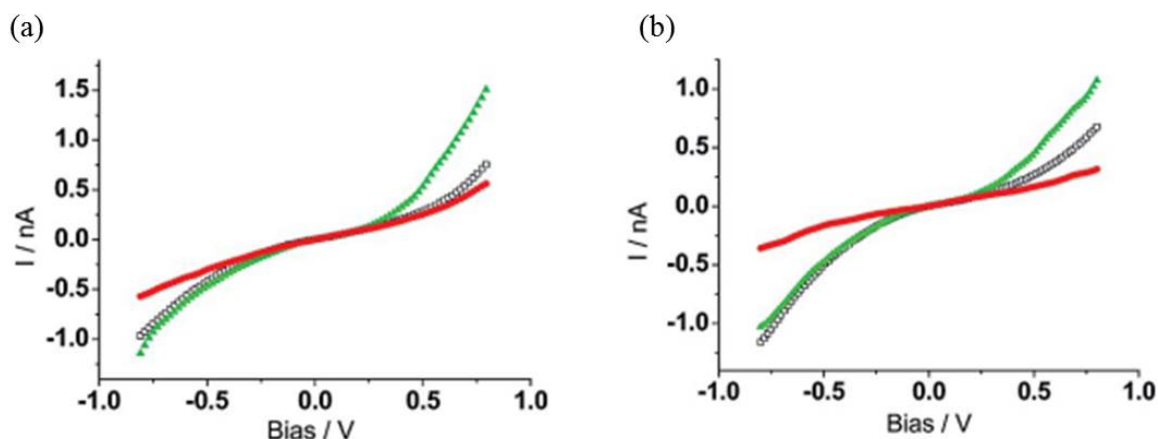
Figure 1.37: (a) I-V characteristic of complex **2** and (b) **3**. Green triangles: LS state, red circles: HS state, black squares: HOPG background [89].

An interesting perspective has been published by Palamarciuc et al. by performing STM imaging on isolated molecules of the $[Fe(H_2B(pz)_2)_2(bipy)]$ SCO complex obtained by evaporation on a Cu(111) surface [91]. They observed a series of isolated molecules with different orientations from which they deduced the possible adsorbate conformation of the molecule on the surface (Figure 1.38).
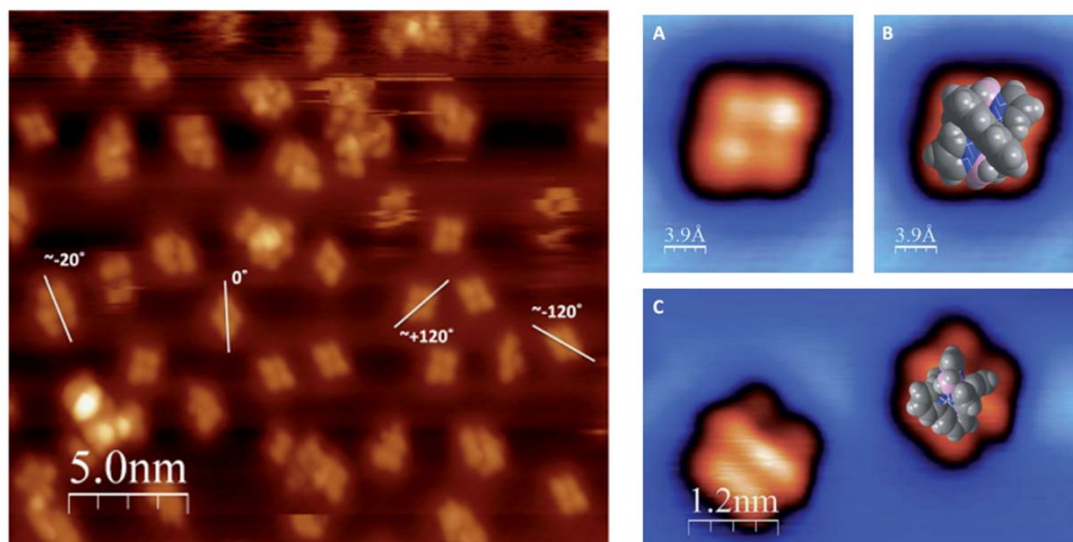
Figure 1.38: SEM image of several isolated molecules in different orientations (left panel). Molecule of $[Fe(H_2B(pz)_2)_2(bipy)]$ (a) in configuration 1 and (b) with an overlay of the possible orientation. (c) Molecule in configuration 2 without and with the overlay of the possible orientation [90].

The same family of compounds has been also investigated by other groups. Pronschinske et al. [92] studied by STM bilayer $[Fe(H2B(pz)2)2(bipy)]$ films on Au(111) surfaces and observed in the conductance maps the coexistence of two different molecules,

but no significant temperature effect between 130 and 300 K on the relative population of the two species. From a comparison of the tunneling spectra and DFT calculations they concluded on a temperature independent coexistence of molecules in the two spin states, the HS state exhibiting a reduced conductance gap with respect to the LS state. The STM investigation of the closely related compound $[Fe(H_2B(pz)_2)_2(phen)]$ on Au(111) has been presented by Gopakumar et al. [93]. Remarkably, they showed a reversible and selective switching of single molecules in a densely packed bilayer of molecules by injecting electrons from the STM tip. The switching process involved a significant change of the differential conductance spectra and showed correlation with DFT calculations, indicating in both cases (i.e. theory and experiment) a decreased gap between the highest-occupied and lowest-occupied molecular orbitals (HOMO-LUMO). In addition a Kondo resonance was also reported in the "reduced gap" molecular state. On this basis the observed switching process was described as a transition between the LS and HS states.

The operation of a nanoscale molecular switch containing a single molecule to store information has been presented by Miyamachi et al. [94]. In this work they studied $Fe(phen)_2(NCS)_2$ spin crossover molecules deposited on metallic surfaces and they observed a field-induced switch between a low and high conduction state. Remarkably this switch could be obtained only when the molecules were decoupled from the metallic substrate by a nitrogen insulating layer highlighting the outmost importance of the electronic coupling between the molecules and the substrate. The hysteretic I-V characteristic of a single molecule is presented in Figure 1.39a.
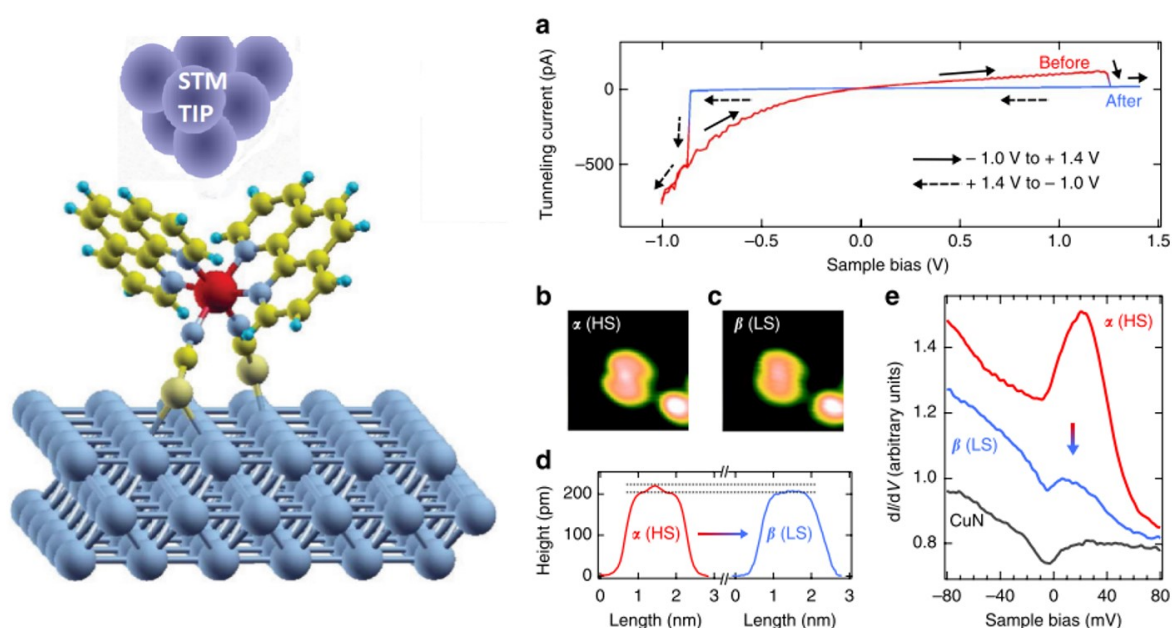
Figure 1.39: (a) I-V characteristic of an isolated $Fe(phen)_2(NCS)_2$ molecule on CuN/Cu(100) surface. STM image for the (b) HS and (c) LS states with the corresponding (d) height profile. (e) Differential conductivity of the molecule in the HS and LS states as well as that of the CuN insulating layer [93].

The higher and lower conduction states can be obtained reversibly by applying a bias of +1.2 V and -0.8 V, respectively. The switching of the tunneling current with the bias ramping is also accompanied by a structural change observed in the STM images as well as in the height profiles as shown in Figure 1.39. The difference between the two states

can be highlighted by plotting the differential conductance (dI/dV) as illustrated in Figure 1.39e. The difference between the two states is clear here, as only one of the two states present a Kondo peak, characteristic of a magnetic impurity on a conductive surface. On this basis the high (low) conductance state is assigned to the HS (LS) state of the molecule. This switching phenomena has been also used to demonstrate a memristor operation in these devices. Gruber et al. [95] continued the work on the same complex deposited on Cu(100) surface with coverages ranging from 0.1 to 1.8 monolayers on which STM measurements were performed. A coverage-independent coexistence of both spin states at low temperatures (4 K) on the first monolayer has been reported. In the case of the second-layer molecules, the influence of the substrate is reduced and a switching between the two states was observed when cycling the bias voltage. Gueddida et al. [96] have calculated by DFT the STM pictures of $Fe(phen)_2(NCS)_2$ on transition metal surfaces and pointed out the importance of electronic coupling with the substrate.

The low temperature charge transport mechanism in a three terminal device containing a Mn-transition metal complex ($[Mn(terpy - O - (CH_2)6 - SAc)_2)]^{2+}$) has been studied by Osorio et al. [97]. Using this configuration the authors demonstrated the direct electrical control of the molecular spin state of a single metal complex. To this aim the molecule was bonded to two gold electrodes obtained by electromigration. By adjusting the gate-voltage the terpyridine ligand was reduced leading to an increase of the ligand-field on the central metal ion, which allowed for a transition between the $S = 5/2$ and $S = 1/2$ spin states of the molecule. A more comprehensive study has been presented by Meded et al. [34] where they show theoretically and experimentally the possibility of electrically controlling the spin-state of a single molecule. Using DFT calculations they predicted that the spin transition can be triggered when two electrons are added to the ligands in the complex $[Fe^{II}(bpp)_2]^{2+}$ [bpp: 2, 6-bis(pyrazol-1-yl)pyridine]. From an experimental point of view they used a three-terminal device configuration with a single molecule of the $[Fe - (L)_2]^{2+}]$ complex [L = 4'-(4'''-pyridyl)-1,2':6'1''-bis-(pyrazolyl)pyridine] as shown in Figure 1.40a. Figure 1.40b illustrates a typical differential conductance map as a function of the source-drain and gate voltages, which exhibits a classical single-electron transport trough a nano-object. The shift in the gate voltage ΔV_g of the Coulomb edges is a consequence of the modification of the electrostatic environment of the molecule. These transport measurements reveal a double-quantum-dot behavior combined with a split Kondo peak, which can be interpreted as an indication of an SCO behavior.
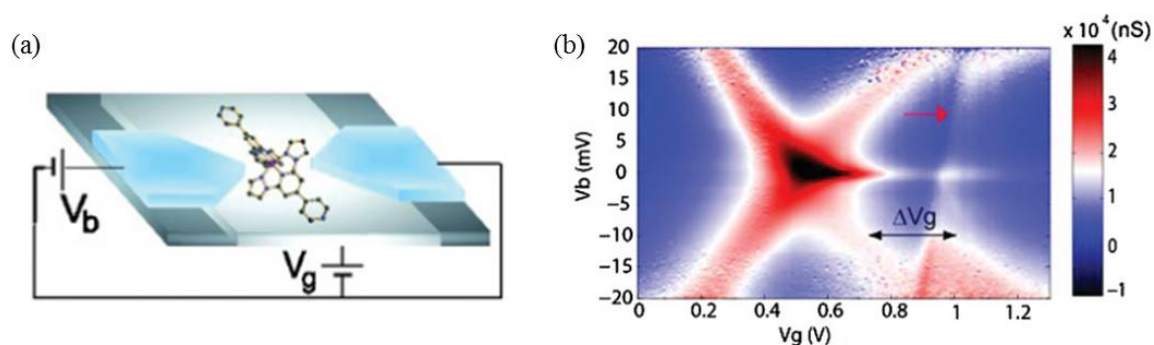
Figure 1.40: (a) Schematic representation of the three-terminal device containing a SCO molecule. (b) Differential conductance as a function of source-drain (V_b) and gate (V_g) voltages [34].

In the first case the considered complex was $[Fe(AcS-BPP)_2](ClO_4)_2$, where AcS-BPP = (S)-(4-[[2,6-(dipyrazol-1-yl)pyrid-4-yl]ethynyl]phenyl)ethanethioate) [98]. Molecules were attached to gold nanoparticles of 8.5 nm in diameter, which were then arranged in a 2D network, as shown in Figure 1.41. The particular interest of such well-organized molecule-nanoparticle networks is that the occurrence of SCO phenomena in the junctions could be confirmed by independent control techniques (Raman spectroscopy and magnetization measurements). Charge transport measurements as a function of temperature have been performed on four devices, three of which contained passive "control" molecules. Figure 1.41 shows the temperature dependence of the resistance of a few devices. The monotonic decrease of the resistance and the formation of the plateau at higher temperatures is an indication of a Coulomb blockade due to the small size of the nanoparticles. This was observed for each device. On the other hand an increase of resistance above 280 K was observed only in the case of the SCO-gold nanoparticle arrays. The charge transport behavior of the device containing SCO molecules was explained through a percolation model that assumes that the HS state is more resistive than the LS state, assumption that has been confirmed also by theoretical calculations.
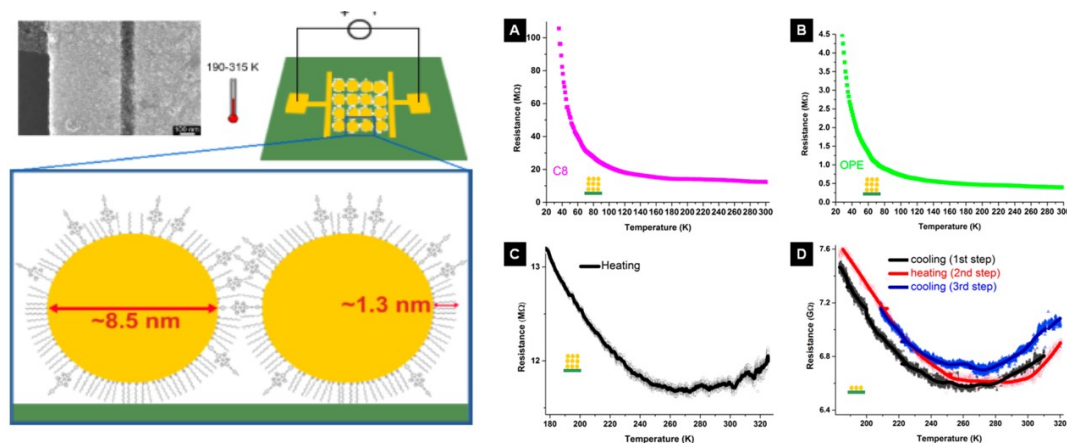
Figure 1.41: Left panel: SEM image and schematic drawing of the SCO molecule gold nanoparticle 2D array for single molecule conductance studies. Right panel: Resistance as a function of temperature of a gold nanoparticle network with (a) octanethiol molecules, (b) dithiolated oligo(phenylene ethynylene) molecules, (c) SCO molecules (three layers) and (d) SCO molecules (monolayer) [97].

Spin state switching using a voltage of a single $[Fe^{II}(tpy)_2]$ molecule placed in a mechanically controlled break junction has been demonstrated by Harzmann et al. [99]. This experiment is based on the sensitivity of spin state of this complex to the spatial arrangement of the ligands. By applying an electric field across the molecule, a mechanical distortion of the coordination sphere occurs leading to a change of the ligand field. A schematic representation is shown in Figure 1.42. The experimentally observed typical I-V characteristics are also illustrated in Figure 1.42. The three main I-V characteristics found in 28 devices are as follows. In four of them a hysteretic behavior has been observed, displaying a current jump at 0.7 V upon sweeping forward and a second jump at -0.5 V by sweeping in the opposite direction (Figure 1.42a). In the remaining 24 junctions a negative differential conductance (Figure 1.42b) or current jumps (Figure 1.42c) have been recorder in both sweeping directions. This variety of characteristics may be the result of different orientations of the molecule in the junction with various extents of electrode-molecule interactions.
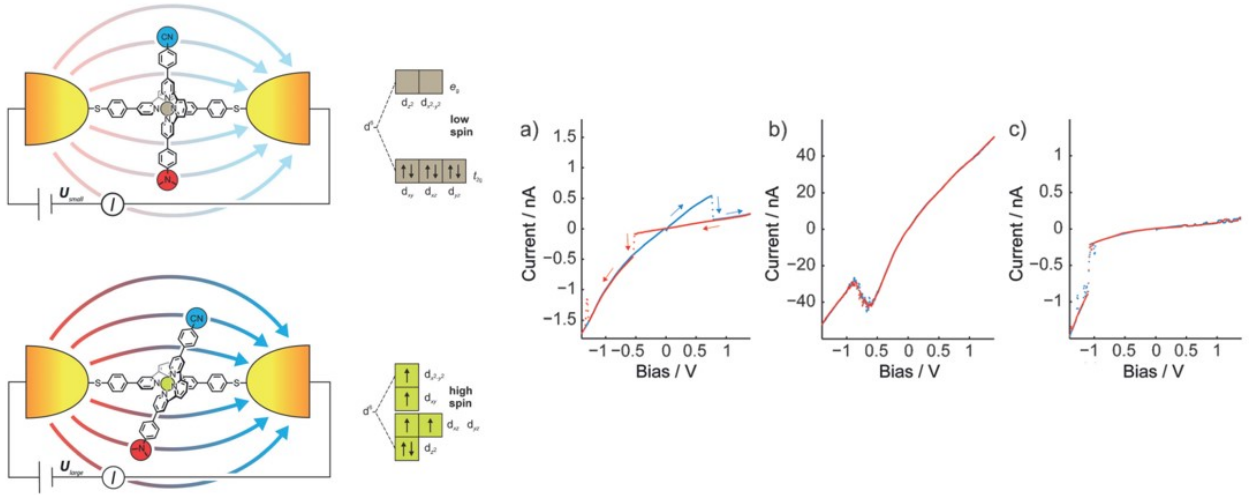
Figure 1.42: Schematic representation of the voltage triggered spin transition of the $[Fe^{II}(tpy)_2]$ complex. I-V characteristic showing (a) hysteresis, (b) negative differential conductance and (c) a jump in current [98].
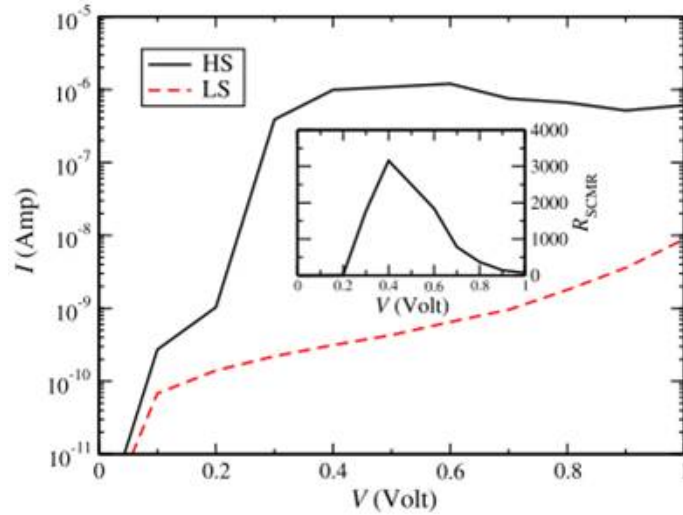
Figure 1.43: Simulated I-V characteristic for a FeL_2 molecule connected to gold electrodes [99].

The change of the resistance of single SCO molecules connected to metallic electrodes has been theoretically studied by Baadji and Sanvito [100] using a combination of density functional theory and the non-equilibrium Green's function methods for quantum transport. They have determined a magnetoresistance ratio of 200 % at zero bias and around 3000 % at higher voltage biases. The simulated I-V characteristic (see Figure 1.43) showed a current intensity difference between the HS and the LS states of three orders of magnitude. In the LS state the current has a tunnel-like characteristic in the whole voltage range and increases monotonically with bias. In the HS state, however, the I-V characteristic is different since the both the HOMO and the LUMO transmission resonances are bridged by a relatively small voltage bias of 0.4 V. These results not only prove that the molecule in the two spin states possesses very different conductivities, but also that the mechanism of the molecular switching is not only associated to a change in the

molecule geometry, but has an electronic origin as well. A similar theoretical approach has been adopted by Aravena et al. [101] to compute the I-V characteristics of a trans-bis(3-(2-pyridyl)[1,2,3]triazolo[1,5-a]-pyridine)bis(isothiocyanato)iron(II) molecule connecting two gold electrodes. They predicted a higher current in the HS state with respect to the LS state and made some comparisons with the available experimental data as well.

1.3   Conclusions

Concluding this chapter one can easily see the versatility of SCO materials due to their change of magnetic, optical, mechanical and structural properties, which can be in different forms ranging from gradual crossover to transition with hysteresis. Also, the wide variety of useful stimuli and chemical composition makes these materials extremely attractive for various technological applications. To this end, the necessity of electrically controlling the two magnetic states using electrical stimuli is essential, hence a good understanding of their charge transport properties is needed. Starting from the pioneering works on the bistability of the dielectric constant of bulk SCO powders to the voltage-triggered spin transition in a single molecule, this field has advanced considerably in the past decade. At the macroscopic scale the spin-state dependence of charge transport and dielectric properties offers new opportunities for the investigation of the charge carrier dynamics and electronic structure of these compounds. In addition, these properties open up perspectives for the development of micro- and nano-electronic devices with spin-state switching functionality. The highly insulating nature of SCO compounds represent, however, an obstacle for a number of applications. This problem has been overcome by the development of hybrid SCO-conductor systems, which provide in addition also interesting synergy between different electronic phenomena. Hybrid materials were first synthesized by the co-crystallization of molecular SCO and conductor units, which proved to be a fundamentally very interesting, but also very challenging synthetic task. In a more pragmatic manner, SCO complexes were also mixed with piezoresistive polymers, which lead eventually to bistable conducting composite materials. Other possible approaches to overcome the insulating nature of SCO compounds are based on the device design. For example devices with different competing charge transport channels can be constructed wherein the spin crossover phenomenon can lead to a switching in the nature of molecular orbitals involved in the charge carrier transport. Another interesting possibility is the fabrication of tunneling devices with large area SCO tunnel junctions, which may open up also prospects for spintronic devices. Another field in fast development is the study of charge transport in SCO complexes at the single molecule level. In the case of single molecule devices, it has been shown that the coupling between the SCO molecule and the metallic electrode has a major impact on the electronic structure and switching properties of the molecule. Nevertheless, by carefully controlling this interface, remarkable results have been presented on single molecules or molecular clusters including also their electrical addressing. Further work is, however, necessary to clarify the microscopic details of the different phenomena reported at the single molecule level.

Chapter 2

Electrical properties of spin crossover compounds in powder form

Electrical characterization of SCO materials is essential in understanding their behavior, and their potential applications in micro/nanoelectronic devices. In this chapter the quasi-static and dynamic electrical properties of the $[Fe(Htrz)_2(trz)](BF_4)$ spin crossover complex were analyzed using broadband dielectric spectroscopy. We have chosen this compound based on its outstanding charge transport properties previously identified in our team [31, 36]. In the first part of this chapter, the broadband dielectric spectroscopy technique is shortly presented, along with some general considerations on the electrical parameters which can be extracted from this measurement. The second section of this chapter is dedicated to the study of the $[Fe(Htrz)_2(trz)](BF_4)$ complex in bulk nanocrystalline form. The temperature and frequency dependence of the complex electrical conductivity, dielectric permittivity and electric modulus were analyzed to better understand the dynamics of the charge carriers. In order to get further insight into the charge transport properties of this complex, a series of microcrystalline powder samples of formula $[Fe_{1-x}Zn_x(Htrz)_2(trz)](BF_4)$ were synthesized wherein a part of the "active" iron centers were replaced by "inactive" zinc ions. A thorough physico-chemical analysis has been performed on all the samples to ensure that the compounds are isostructural and isomorphic. Then, their dielectric spectra were compared and analyzed in detail.

2.1 AC electrical characterization by broadband dielectric spectroscopy: theoretical considerations

One of the most efficient methods to analyze the dielectric and charge transport properties of a material is broadband dielectric spectroscopy (BDS) [102]. This technique provides information about various electric properties like conductivity, permittivity, electric modulus, impedance and much more, on a multitude of materials, like organic and inorganic solids, crystals, amorphous materials or liquids in a wide range of frequencies (usually from 10^{-4} Hz to 10^{10} Hz). BDS can be also fitted with heaters and cryogenic systems which provide wide temperature ranges from liquid nitrogen to several hundred degrees Celsius.

In order to analyze a specific material, special electrodes have to be made. In most

cases, where the sample is in powder form, or can be grown as thin films on substrates, a parallel electrode configuration is used. The capacitor-like device is placed in the sample holder of the BDS and a sinusoidal voltage $v(t) = V_0 sin(\omega t)$ is applied to the cell and the generated current $i(t) = I_0 sin(\omega t + \delta)$ is measured. The phase difference δ between the applied voltage and the measured current is registered. This phase change is explained by the fact that by applying a periodic electric field $E(t)$ to a dielectric material, the material is polarized $P(t)$ and the measured current suffers a phase shift as illustrated in Figure 2.1.
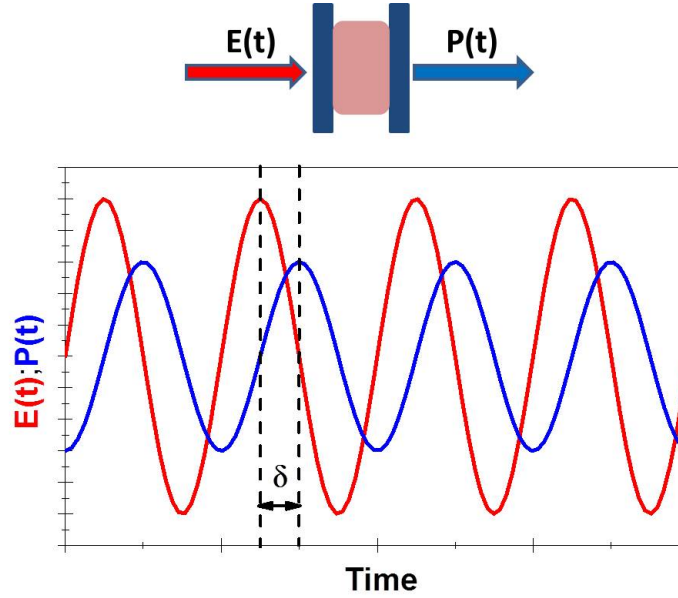
Figure 2.1: Schematic representation of a BDS sample (top) and the input and output parameter variation.

The periodic electric field and the polarization response can be written as:

$$E(t) = E_0 sin(\omega t) \tag{2.1}$$

and

$$P(t) = P_0 sin(\omega t + \delta) \tag{2.2}$$

A relation between the polarization and the electric field can be written as:

$$P(\omega) = \epsilon_0 [(\epsilon' - i\epsilon'') - 1] E(\omega) \tag{2.3}$$

and

$$tan\, \delta = \frac{\epsilon''}{\epsilon'} \tag{2.4}$$

where ϵ' is the real part of the complex permittivity, which is a measure of the stored charge [103] and ϵ'' is the imaginary part of the complex permittivity ϵ^*, which represents the dielectric loss, respectively, and ϵ_0 is the permittivity of free space.

Having defined the complex permittivity one can further extend the quantities that characterize not only the device, but the material itself. The complex impedance of the device can be written as:

$$Z^* = \frac{1}{i\omega\epsilon^* C_0} \tag{2.5}$$

where C_0 is the capacitance of the empty cell.

Another important parameter in the study of the electrical properties of materials is the electric modulus $M^* = 1/\epsilon^*$. The parameter of interest is the imaginary part of electric modulus, M'', and is used to circumvent possible interference of electrical conduction and/or electrode polarization which can mask charge carrier relaxation processes [104–106]. The complex modulus M^* can also be written as:

$$M^* = M' + iM'' = \frac{\epsilon'}{(\epsilon')^2 + (\epsilon'')^2} + i\frac{\epsilon''}{(\epsilon')^2 + (\epsilon'')^2} \tag{2.6}$$

The typical frequency dependence of the electric modulus is illustrated in figure 2.2 [107] for $0.5Li_2O - 0.5Na_2O2B_2O_3$ (LNBO) glasses . The spectrum presents a maximum which corresponds to the relaxation frequency of charge carriers when passing from long-range to short-range mobility. The temperature dependence of the spectra denotes also that this relaxation is a thermally activated process.
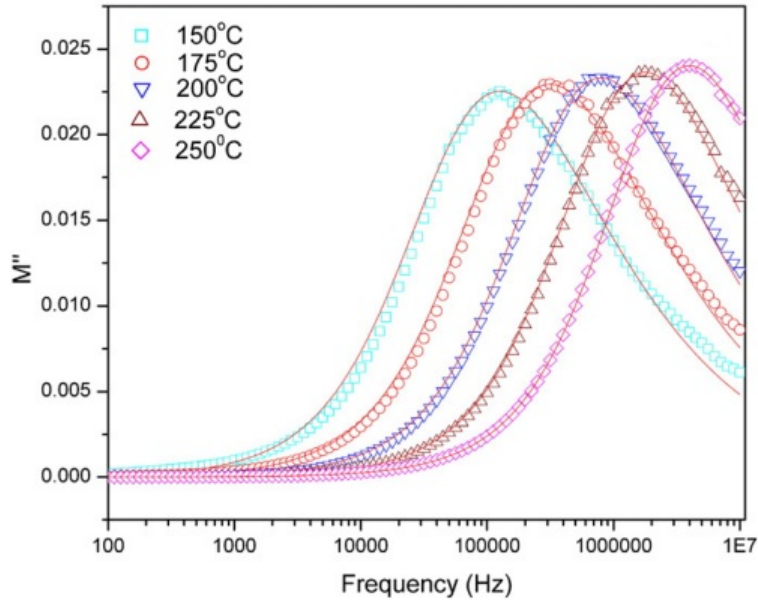
Figure 2.2: Typical frequency dependency of M'' for the LNBO glasses.

The complex electric modulus can be fitted either with the Debye model or (more frequently) with the Havriliak-Negami empirical equation to extract the relaxation time τ_M^* and the parameters characterizing their distribution α and β.

$$M^* = M_\infty - \frac{M_\infty - M_0}{[1 + (i\omega\tau_M^*)^\alpha]^\beta} \tag{2.7}$$

The complex conductivity σ^* is defined as:

$$\sigma^* = \sigma' + i\sigma'' = \omega\epsilon_0\epsilon'' + i(\omega\epsilon_0\epsilon') \tag{2.8}$$

where σ' represents the real part of the complex conductivity and it is the frequency dependent or AC conductivity. The conductivity dependence on frequency (or angular frequency) was discussed by Jonscher [108] and is considered as being a universal AC conduction in

41

disordered solids [109, 110], which obeys the following expression:

$$\sigma' = \sigma_{DC} + A\omega^n = \sigma_{DC}\left[1 + \left(\frac{\omega}{\omega_c}\right)^n\right] \tag{2.9}$$

where σ_{DC} is the DC conductivity, A is a pre-exponential factor and n is a frequency and temperature dependent exponent. ω and ω_c are, respectively the angular frequency and the cutoff angular frequency. The cutoff frequency represents a change in the slope of the conductivity, which indicates a change in the charge transport mechanism from long-range or delocalized conduction to short range, or localized conduction. Above ω_c the conductivity increases with increasing frequency, since the localized charge carriers take maximum advantage on well conducting regions, while at low frequencies, charge carriers must move through larger distances including poorly conducting regions and bottlenecks. This dependence is illustrated in the figure below the dianhydride 3,4,3',4'-biphenyltetracarboxylic dianhydride (BPDA) and 4, 4'-oxydianiline (ODA).
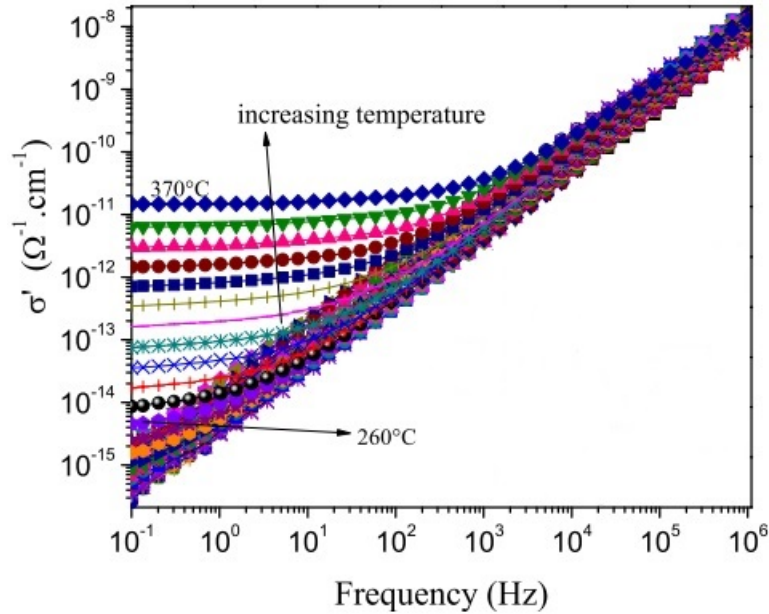
Figure 2.3: Frequency dependency of the real part of conductivity σ' at different temperatures for BPDA/ODA.

Another way that broadband dielectric spectroscopy data can be interpreted is by plotting the master curves for the electrical conductivity and the modulus as a function of frequency for various temperatures. The real part of conductivity is divided by the dc conductivity ($\sigma'/\sigma_D C$), while the imaginary part of the modulus is divided by the maximum value (M''/M''_{max}), whilst the frequency is divided by the frequency at which the maximum of M'' is found (f/f_{max}). This scaling is done to better observe slight deviations from the "universal" behavior of the disordered solids, which can be hidden by the thermal variation of these quantities.

2.2 Charge transport mechanism of $[Fe(Htrz)_2(trz)](BF_4)$ bulk compound

2.2.1 Physico-chemical characterization of the sample

Scanning Electron Microscopy (SEM) micrograph and Transmission Electron Microscopy (TEM) images of the powder sample of $[Fe(Htrz)_2(trz)](BF_4)$ reveal that the sample consists of particles with a size of about 10-15 nm, which form larger aggregates with a size of about 200 nm (Figure 2.4).
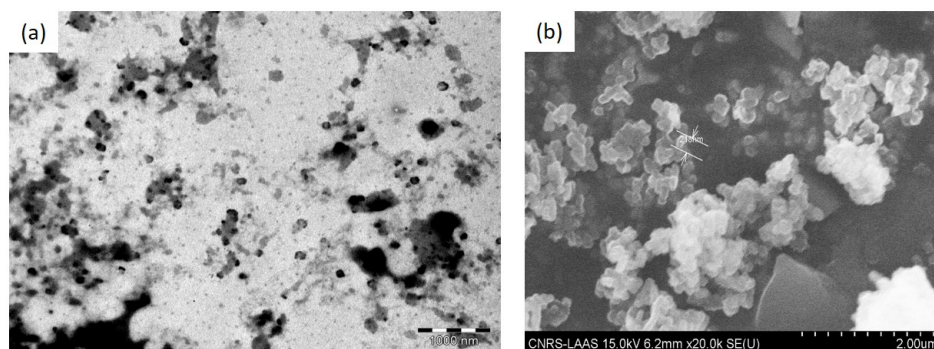
Figure 2.4: (a) SEM micrograph and (b) TEM image of the bulk sample $[Fe(Htrz)_2(trz)](BF_4)$.

In order to determine the temperature range in which the sample presents the spin crossover, variable temperature optical reflectance measurements were carried out. The measurements were done in reflectivity mode (green light) using an Olympus BX51 optical microscope equipped with a CCD camera. The heating and cooling of the sample was done inside a Linkam THMS600 variable temperature stage by varying the temperature at a rate of 2 K/min. The resulting characteristic reveals the transition temperatures around 380 K for the LS to HS transition, whereas the HS to LS transition occurs around 370 K as illustrated in Figure 2.5.
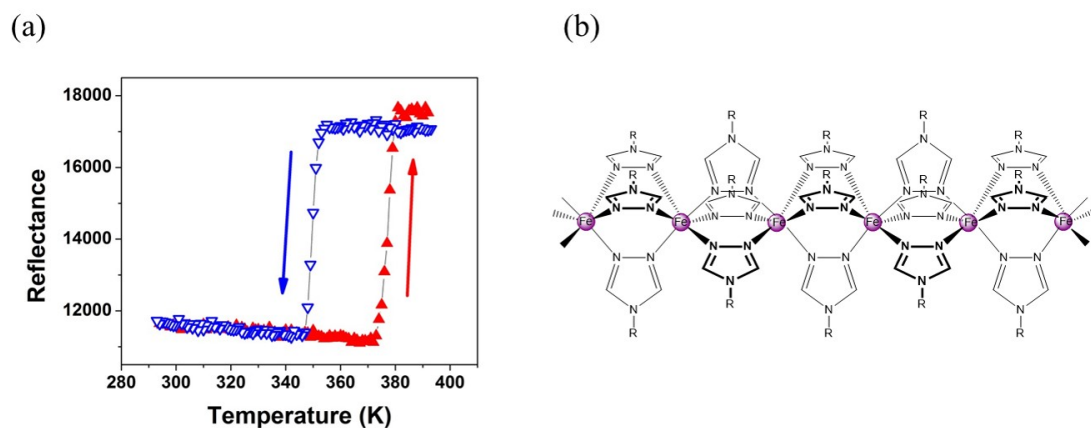
Figure 2.5: (a) Thermal variation of the optical reflectance (λ =540 nm) and (b) the schematic representation of the chemical structure for the bulk sample $[Fe(Htrz)_2(trz)](BF_4)$.

43

IR spectroscopy performed at room temperature (Figure 2.6) and X-Ray crystallography data (Figure 2.7) recorded in the LS (at 300K) and HS (at 420K) states reveal the same markers found by Rotaru et al. in ref [31] for this compound confirming its structure, composition and SCO properties. Similar to other SCO compounds, the LS to HS transition involves a shift of the diffraction peaks towards lower 2θ angles, due to the lattice expansion, in particular the shifts of the Bragg peaks around $24^o - 26^o$ upon the SCO are rather important confirming that the sample used for this experiment is the same as the one used in ref [31]. It is important to note also that XRD patterns in the two spin state are very similar (apart from peak shifts) suggesting they are closely isostructural.
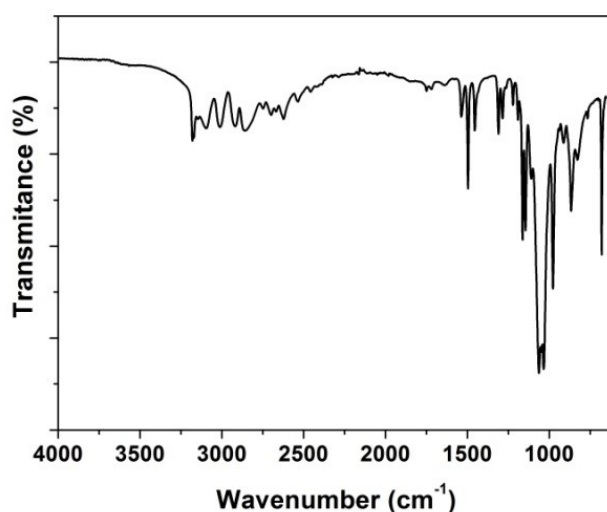
Figure 2.6: IR-ATR spectra of the bulk sample at room temperature.
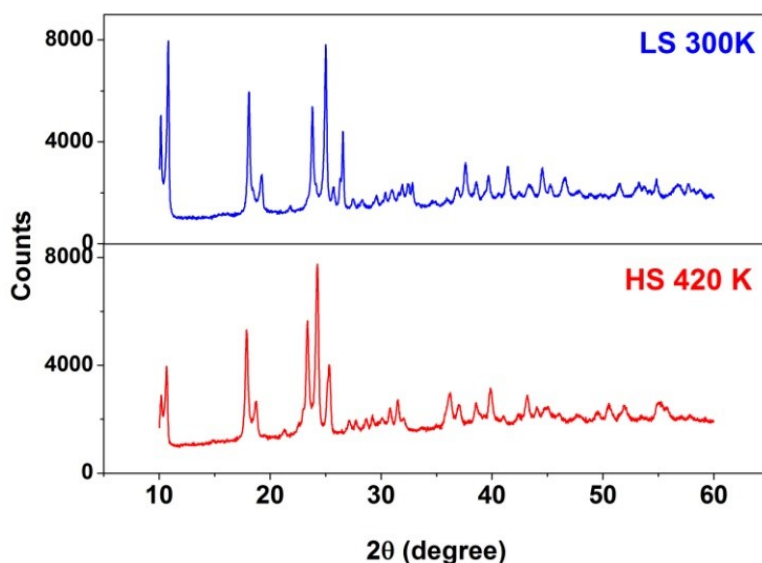
Figure 2.7: Powder XRD patterns obtained on $[Fe(Htrz)_2(trz)](BF_4)$ in the LS and HS states respectively.

2.2.2 Electrical characterization of $[Fe(Htrz)_2(trz)](BF_4)$ bulk compound

Charge transport mechanism was investigated using broadband dielectric spectroscopy on the nanocrystalline sample (ca. 10-15 nm sized nearly spherical particles which forms aggregates of around 200 nm). The powder was pressed inside a Teflon sample holder between two stainless steel electrodes (see Figure 2.8a) and its complex impedance was determined using a Novocontrol BDS 4000 broadband dielectric spectrometer (Figure 2.8b) between 320 K - 380 K both in cooling and heating in a frequency range of 10^{-2} Hz - 10^6 Hz. The analysis of the frequency and temperature dependency of the real part of electrical conductivity, σ', dielectric permittivity ϵ' and the imaginary part of the electric modulus M'' has been performed.
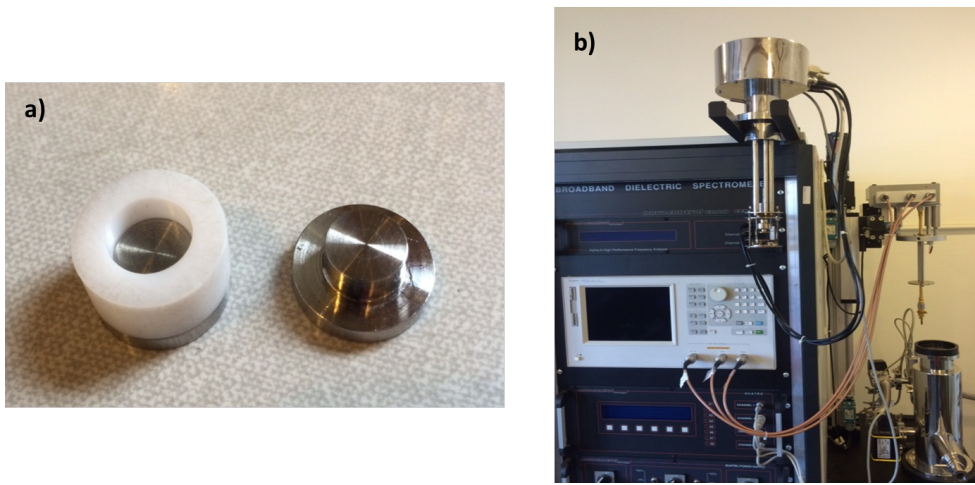
Figure 2.8: a) Teflon sample holder and electrodes. b) Novocontrol BDS 4000 broadband dielectric spectrometer.

The real part of the AC conductivity (σ'), recorded in the heating and cooling modes, is reported in Figure 2.9. Starting from a cut-off frequency, which depends both on the temperature and the spin-state of the compound, the AC conductivity obeys a power law at high frequencies. This behaviour is characteristic to low mobility, disordered systems where σ' obeys the "universal dielectric response (UDR)" described by Jonscher [108]:

$$\sigma' = \sigma_{DC} + A\omega^n = \sigma_{DC}\left[1 + \left(\frac{\omega}{\omega_c}\right)^n\right] \qquad (2.10)$$

where n ($0 < n \leq 1$) was interpreted by means of many body interactions among charge carriers [108]. The cut-off frequency ω_c can be assimilated with the charge hopping frequency [111]. As shown in Figure 2.9c, the values of exponent n are very close (0.47 and 0.44, respectively) in the HS and LS states, which indicates that the conduction mechanism at high frequencies is probably the same in the two spin states. Below ω_c, the AC conductivity increases slowly with increasing frequency depending of the spin state. In the LS state, $\sigma'(\omega)$ exhibits more clearly a step-like increase in the range 1 - 10^3 Hz, which can be a signature of a Maxwell-Wagner type contribution of depletion layers at grain boundaries of the powder [112]. This behavior is clearly observed in Figure 2.9b at 320 K and 330 K in the LS state. In this case the interfacial polarization effectively reduces the conductivity by one decade at low frequencies. The values of the AC conductivity measured at 10^{-2} Hz

are in good agreement with those obtained from the previous DC electrical measurements in our team ($\sim 10^{-9}$ $S \cdot cm^{-1}$ at 355 K, heating mode) [31]. The important finding here is that the electrical conductivity displays a spin state dependence in the whole studied frequency range, showing a thermal hysteresis loop (see Figure 2.9d) characterized by the same switching temperatures as detected in the optical measurements (see Figure 2.5a). The conductivity of the LS state exceeds by more than one order of magnitude that of the HS state both in the DC and AC regimes, which is of primary importance for applications requesting fast data rate.
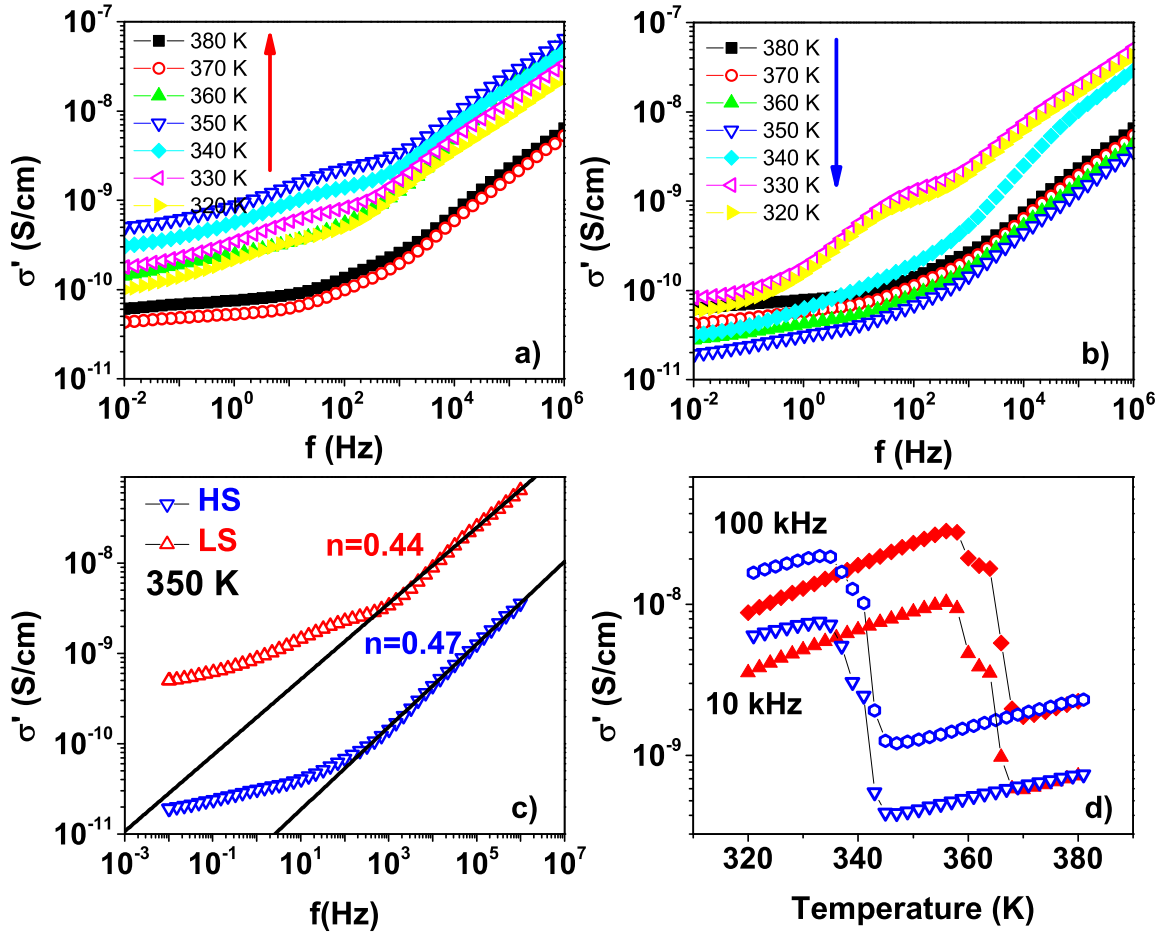
Figure 2.9: Real part of the AC conductivity of the $[Fe(Htrz)_2(trz)](BF_4)$ as a function of the frequency, measured at selected temperatures in the a) heating and b) cooling modes. c) Conductivity spectra at 350 K in the HS and LS states. The fits of the high-frequency part of the spectra are also shown. d) Thermal hysteresis of σ' recorded at 10 kHz and 100 kHz.

Figure 2.10 displays the frequency dependence of the real part of the complex dielectric permittivity, which is a measure of stored energy. The region at low frequencies is dominated by an important dispersion caused by electrode polarization. The measured value of ϵ' increases with decreasing frequency at each temperature. The temperature dependence of the dielectric permittivity (real part) exhibits a wide hysteresis loop of 25 K (see the inset of Figure 2.10) and the value of the permittivity (recorded at 1 kHz) decreases

by 5 times when the compound is switched from the LS to the HS state. The strong decrease of the permittivity in the HS state is rather unusual in SCO compounds [24] and should be linked to the charge transport properties of this complex. This important variation of the permittivity (even if partly extrinsic as related to the electrode polarization) makes this sample an attractive material for electronic capacitive storage devices.
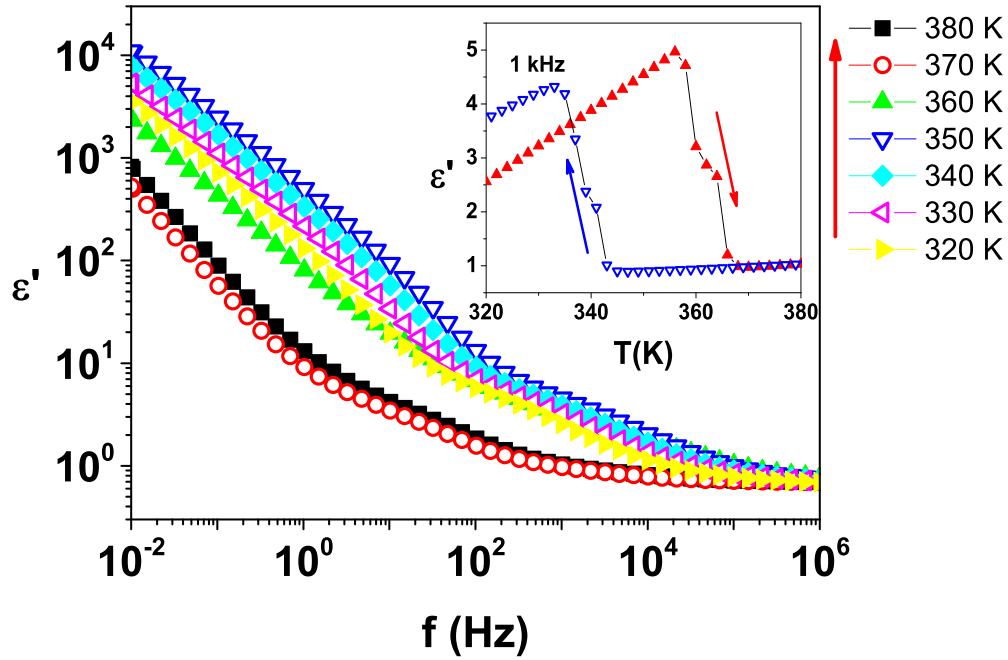
Figure 2.10: Real part of the dielectric permittivity as a function of the frequency, measured at selected temperatures in the heating mode. The inset shows the thermal hysteresis loop of ϵ' recorded at 1 kHz.

For a better understanding of the relaxation process with respect to the material properties the electric modulus formalism ($M^*(f) = 1/\epsilon^*(f)$) has been considered for our analysis. This approach enables us to circumvent the effects of electrode and space charge polarization, which might mask the dielectric relaxation. The frequency dependence of M'' recorded at different temperatures reveals two loss peaks, which characterize the two spin states (Figure 2.11a). Remarkably, when switching the material from the LS to the HS state the loss peak frequency exhibits a spectacular drop by about three orders of magnitude (Figure 2.11b). When the transition is in progress (for example at 340 K) the two loss peaks coexist. This is the clear sign of a phase separation as expected for a first-order phase transition. Figure 2.11c displays the scaled electric modulus vs. the scaled frequency. A perfect overlap of the scaled relaxation peaks in a given spin state has been observed, however a significant difference exists between the HS and LS curves. This means that the dynamical processes are the same at each temperature in a given phase, but change with the spin state of the compound.
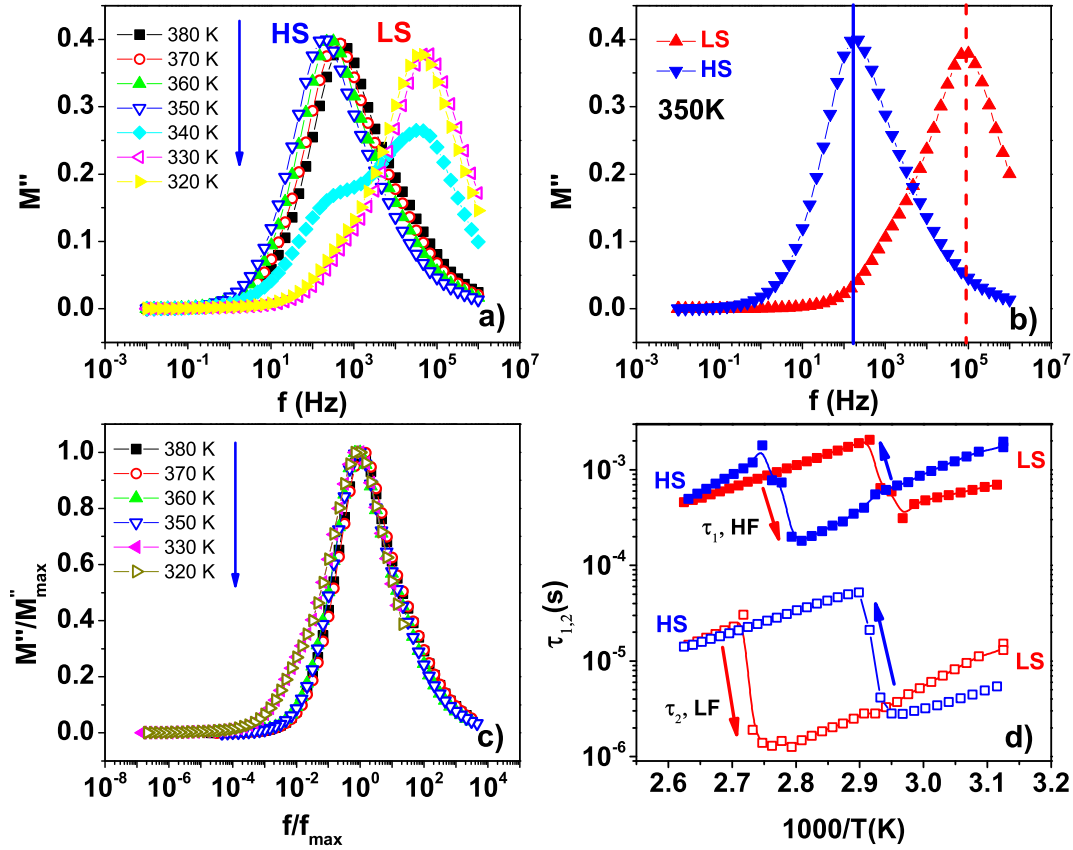
Figure 2.11: a) Dielectric loss modulus M'' at selected temperatures in the cooling mode. b) Spin state dependence of M'' at 350 K. c) Plot of the normalized loss modulus (M''/M''_{max}) as a function of the reduced frequency (f/f_{max}). d) Thermal hysteresis loops of the HN relaxation times ($\tau_{1,2}$).

A Havriliak-Negami (HN) empirical equation [113] was used to describe the frequency dependence of the loss peak as follows:

$$M^* = M_\infty - \frac{M_\infty - M_0}{[1 + (i\omega\tau_M^*)^\alpha]^\beta} \qquad (2.11)$$

where M_{inf}, M_0, are the modulus at the high and low frequency limits respectively, τ_M is the HN characteristic relaxation time, while the parameters α and β describe the distribution of relaxation time. The experimental loss modulus data has been fitted by two HN functions. The plot of the two HN (mean) relaxation times, τ_1 and τ_2, as a function of the reciprocal temperature (Figure 2.11d) reveals the same thermal hysteresis as observed also for σ' and ϵ'. The same temperature behavior was obtained for the other HN parameters ($\Delta M = M_{inf} - M_0$, α and β) as well. While a quantitative link is difficult to establish between the relaxation and charge transport phenomena it is tempting to correlate the drop of the relaxation frequency with that of the conductivity, i.e. in the HS state the electrical conduction mechanism is governed by a long range hopping process (lower frequency), while the charge transport in the LS state occurs by a short range hopping (higher frequency) mechanism. Similar to what was reported for other phase change materials [114] the higher hopping frequency and thus the higher conductivity of the LS form might be related to the significant stiffening of the crystal lattice in this phase.

2.3 Zinc dilution effect on charge transport properties of $[Fe(Htrz)_2(trz)](BF_4)$ microrods

In this section we present the analysis on the metal substitution effects on the structural, morphological, charge transport and spin transition properties of the $[Fe_{1-x}Zn_x(Htrz)_2-(trz)](BF_4)$ ($trz = triazole$, x = 0, 0.26 or 0.43) compound using electron microscopy, powder X-ray diffraction, optical reflectivity, Raman, ^{57}Fe Mössbauer and broadband (10^{-2} to 10^6 Hz) dielectric spectroscopies.

The aim of the zinc(II) dilution in the present work is to break the supposed chain of conduction along the one dimensional (1D) structure by exploiting the fact that the 3d orbitals of Zn(II) are fully occupied. On the other hand, the ionic radius of Zn(II) is close to the ionic radius of HS Fe(II) allowing for an isostructural substitution of the ferrous ions. Indeed, this type of metal dilution approach has been intensively used in spin crossover research in order to study the role of the cooperativity on the spin crossover phenomena [53, 115–117]. The study of the charge transport properties of three different powders with formulae $[Fe_{1-x}Zn_x(Htrz)_2(trz)](BF_4)$ ($trz = triazole$, x = 0, 0.26 or 0.43) has been performed. Hereafter the sample with x = 0 is denoted as **S1**, x = 0.26 is denoted **S2** and the sample with x = 0.43 is denoted **S3**. In order to compare the results one must first control that the resulting samples are isomorphic, isostructural and the Zn ions are not segregated but homogeneously distributed.

2.3.1 Spectroscopic and optical characterization of the samples

Representative transmission electron microscopy (TEM) images of the samples are shown in Figure 2.12. Each sample displays similar particle morphology forming microrods with an average length of *ca.* 2 μm and a diameter of $200 - 300$ nm. The same size and shape of the particles of the different samples is very important in order to be able to compare their conductivity.
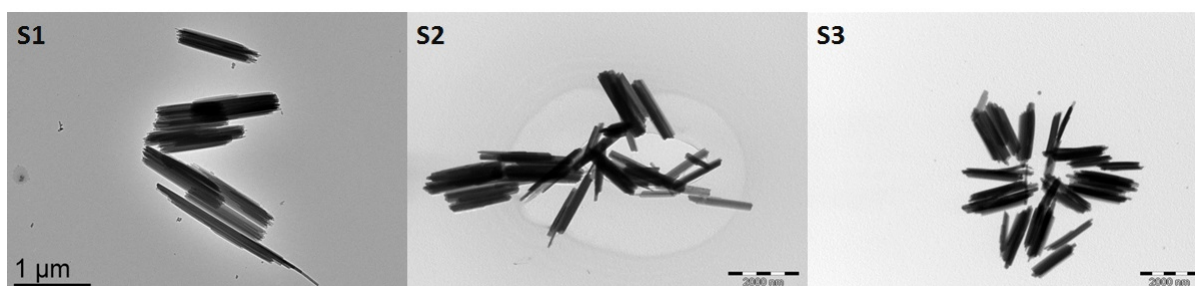
Figure 2.12: Selected TEM images of the samples **S1 - S3**.

In conjunction with the TEM observations, energy dispersive X-ray spectroscopy (EDX) was also carried out in order to evaluate the Zn/Fe ratio in the samples and to investigate the spatial distribution of the metal ions.
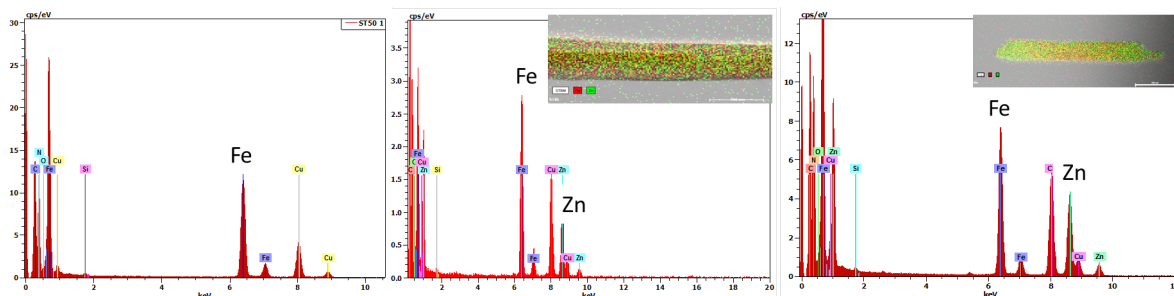
Figure 2.13: EDX spectra for the samples **S1 - S3**. The insets show the distribution of metal ions in a representative sample. (Red/green dots stand for Fe/Zn atoms).

The analysis results performed on different rods for each sample revealed an average of 26 *at.%* of Zn in **S2** and 43 at.% of Zn in **S3**, which are therefore identified as $[Fe_{0.74}Zn_{0.26}(Htrz)_2(trz)](BF_4)$ and $[Fe_{0.57}Zn_{0.43}(Htrz)_2(trz)](BF_4)$, respectively. The TEM-EDX analysis revealed also a homogeneous distribution of the Zn and Fe ions within the volume of the micro-rods and no sign of ion segregation was observed (see Figure 2.13).

The insertion of Zn ions within the crystal structure was investigated through X-ray diffraction (PXRD) and multiple spectroscopic techniques (Raman, Mössbauer spectroscopies). The powder X-ray diffractograms Figure 2.14 show a globally similar pattern for each compound, with some differences for sample **S3**.
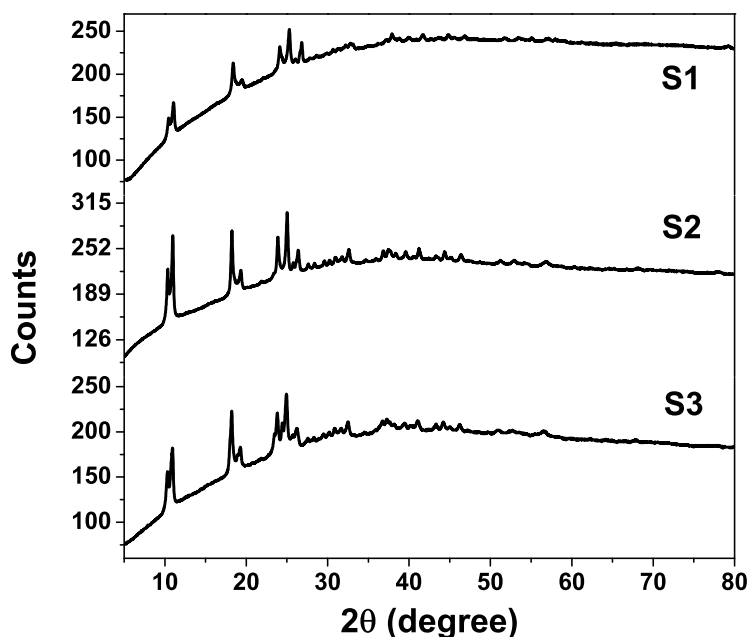
Figure 2.14: Room temperature powder X-ray diffractograms of samples **S1 - S3**.

For samples **S1** and **S2** the main diffraction peaks are grouped for values of 2θ at 10 and 11 degrees, 18 and 19 degrees and 24, 25 and 26 degrees. The additional diffraction

peaks visible in the spectra of sample **S3** are consistent with a small HS fraction at room temperature in this compound. Indeed, as it was shown in Figure 2.11 the LS to HS transition involves a shift of the diffraction peaks towards lower 2θ angles, due to the lattice expansion. In particular the shifts of the Bragg peaks around $24^o - 26^o$ upon the SCO are rather important. This effect is clearly observed in sample **S3** with the shoulders at lower angles. Overall these PXRD results can be interpreted in agreement with the EDX analysis indicating that the Zn ions do not form important segregation in these compounds and instead replace some of the Fe centers to give closely isostructural compounds.

The most relevant conclusions can, however, be inferred from the temperature dependent low-frequency Raman spectra, which are shown in Figure 2.15. As discussed previously (Figure 1.16) the Raman spectra of the compound $[Fe(Htrz)_2(trz)](BF_4)$ exhibit characteristic changes between 100 - 300 cm^{-1} due to the spin transition. At 293 K (LS state) the sample **S1** displays intense Raman modes around 135, 197, 211, 285 and 299 cm^{-1}. When going to the HS state (413 K) one observes Raman peaks around 105, 136, 150 (shoulder), 180 and 190 cm^{-1}. These spectra are essentially the same as reported before. The same peaks and the same changes also appear in the Zn diluted compounds confirming their similar structure.
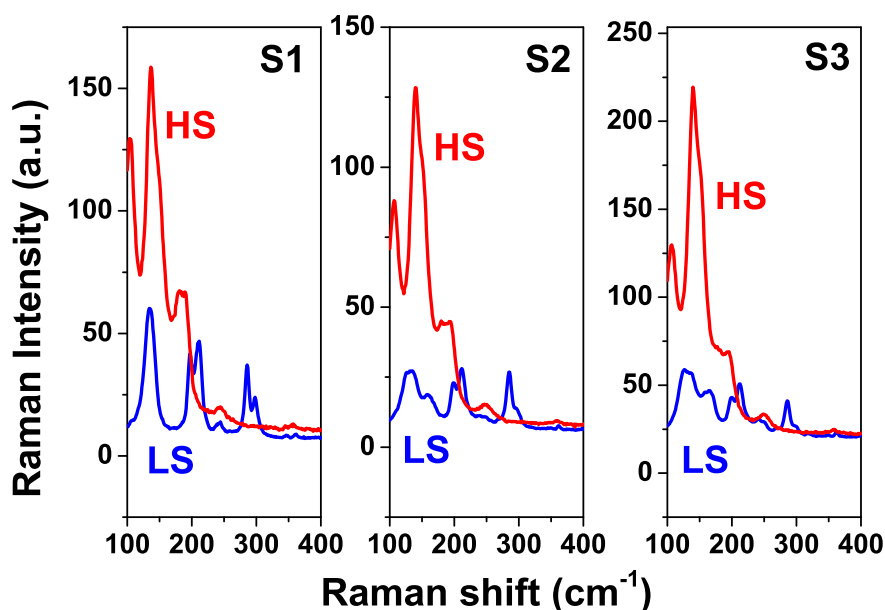
Figure 2.15: Low-frequency Raman spectra of samples **S1 - S3** in the two spin states (293 K: LS, 413 K: HS).

While the HS spectra of the three compounds are almost identical, in the LS state spectra of the diluted compounds, additional peaks are observed around 160 - 166 cm^{-1} and a broadening of the peaks at 135 and 245 cm^{-1} in both samples (**S2** and **S3**). This difference between the HS and LS spectra can be explained by the fact that the ionic radius of Zn(II) matches that of the HS Fe(II). The high temperature Raman spectra are characteristic to the HS state for each sample without any significant residual LS fraction, which can be inferred clearly from the complete disappearance of the Raman peaks at 285 and 299 cm^{-1}. On the other hand, even if the low temperature Raman spectra are clearly characteristic of the LS state, it is difficult to estimate if the transition is complete in this direction due to the spectral overlaps. To verify if there is a residual HS fraction in the samples,

[57]Fe Mössbauer spectra at low temperatures (i.e. in the LS state) was registered. These spectra are shown in Figure 2.16 and the hyperfine parameters are collected in Table 2.1. In each case the spectrum can be properly fitted by only one doublet, characteristic of the LS form of Fe(II). From these Mössbauer and Raman data one can thus conclude that the spin transition of the ferrous ions is complete in both the heating and cooling modes for each sample.
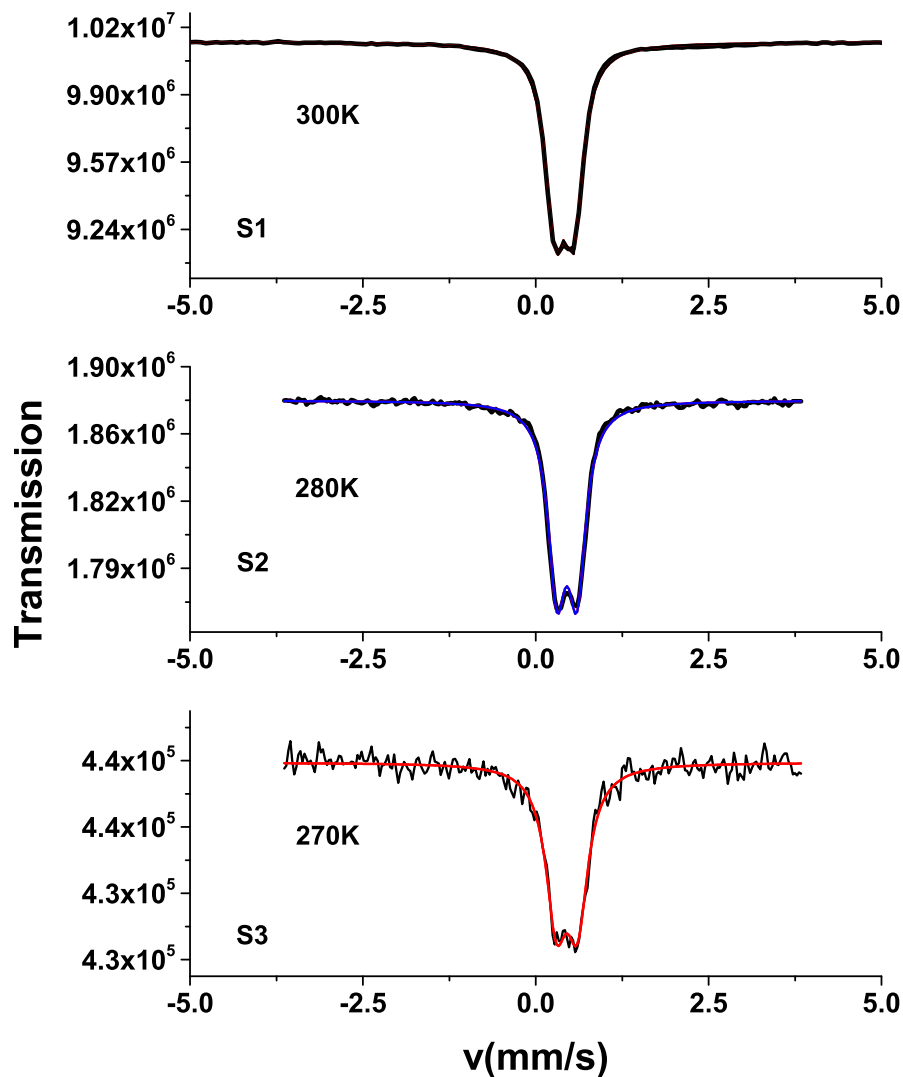
Figure 2.16: [57]Fe Mössbauer spectra of samples **S1 - S3** recorded in the LS state.

Table 2.1: ^{57}Fe Mössbauer parameters of the spectra shown in Figure 2.16. The spectrum analysis was performed by assuming a single low-spin ferrous species and Lorentzian line shapes.

Sample ref.	δ [mm/s]	ΔE_Q [mm/s]	$\Gamma/2$ [mm/s]
S1	0.412(1)	0.270(1)	0.161(1)
S2	0.451(2)	0.289(3)	0.155(3)
S3	0.45(1)	0.31(2)	0.19(2)

(δ - isomer shift vs. α - Fe at room temperature; ΔE_Q - quadrupole splitting; $\Gamma/2$ - half-width at half maximum.)

This spin transition in the samples is also visible through their optical properties since their color turns from violet to white upon heating. This bleaching of the $^1A \rightarrow{}^1T$ ligand-field absorption band (centered at ca. 545 nm) is completely reversible and provides thus a convenient way to follow the SCO phenomena in the samples. The thermal variation of the optical reflectance in the green spectral region is shown in Figure 2.17 for each sample.
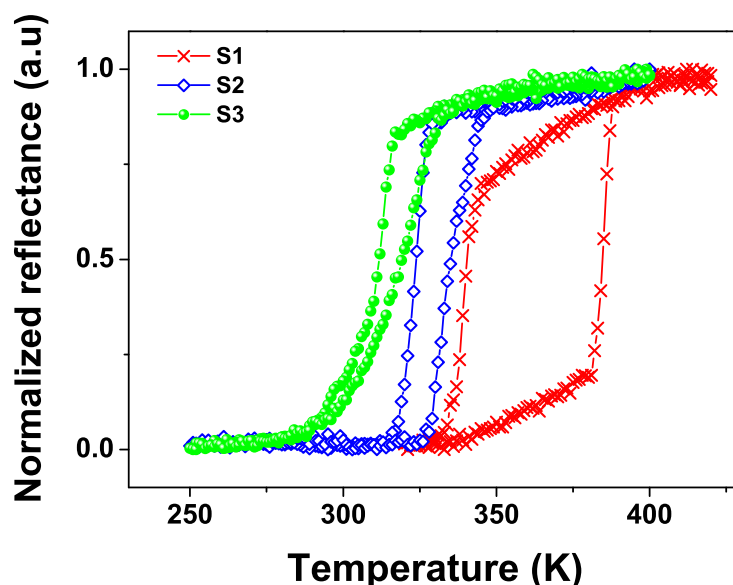
Figure 2.17: Temperature dependence of the optical reflectance at 543 nm for samples **S1-S3** presenting hysteresis loops between the heating and cooling modes.

As expected, the spin transition is shifted towards lower temperatures and the hysteresis width decreases for increasing Zn substitution (Table 2.2). $T_{1/2}\uparrow$ and $T_{1/2}\downarrow$ represents the temperature at witch the complex is at half of the transition in heating and cooling modes, respectively. Such metal dilution effects are well-known and widely used by the spin crossover community to tune and investigate the spin transition properties [65, 116–120]. A short report on the Zn dilution of the title compound was previously reported for a 20% Zn doping [121], wherein a similar - though somewhat less pronounced - shift of the spin transition was observed. The downshift of the spin transition upon Zn doping can be explained by the fact that the ionic radius of the Zn^{2+} ion (96 pm) is much closer to the

ionic radius of Fe^{2+} ions in the HS state (92 pm) than in the LS state (75 pm) [122], i.e. the LS lattice is destabilized due to the misfit of the Zn ions. On the other hand, the hysteresis in SCO compounds is known to occur due to the elastic interactions between the SCO centers. Since the Zn dilution leads to a decrease of the concentration of the SCO active iron ions, the cooperativity of the system decreases, which is reflected by the shrinking of the hysteresis as well as by an increasingly gradual transition [65, 116–123].

Table 2.2: Spin transition temperatures of the samples **S1 - S3** in the cooling and heating cycles and the corresponding hysteresis loop widths from optical reflectivity ([a]) and dc conductivity ([b]).

Sample ref.	$T_{1/2} \uparrow$ [K]	$T_{1/2} \downarrow$ [K]	ΔT [K]
S1	$340^a/348^b$	$386^a/377^b$	$45^a/29^b$
S2	$324^a/324^b$	$336^a/331^b$	$12^a/7^b$
S3	$312^a/314^b$	$320^a/320^b$	$8^a/6^b$

2.3.2   Charge transport properties of diluted series

The frequency dependence of the real part, $\sigma'(\omega)$, of the complex conductivity is reported in Figure 2.18 for each compound at different temperatures both in the heating and cooling branches. The shape of the dispersion curves and the sample conductivity are strongly dependent on the spin state and the Zn dilution. For **S1** the frequency dispersion of the electrical conductivity is strongly dependent on the spin-state and temperature (Figure 2.18a in good agreement with our observation on the nanocrystalline powder presented in the previous Section 2.2.2. The conductivity shows, at all temperatures, a typical low frequency plateau, characteristic to a non-localized or a long-range charge carrier mobility. Above the crossover frequency, ω_c, the real part of the conductivity increases with increasing frequency obeying Jonscher's power law from equation 2.10.

For **S2** and **S3** the plateau at low frequency is strongly reduced and the dispersion of the AC conductivity shifts to lower frequency, *i.e.*, ω_c decreases (Figure 2.18b and c), in agreement with the more insulating character of the diluted samples. Indeed, the conductivity σ' of the samples at 10^{-2} Hz (DC regime) and at 293 K (LS state) is ca. 10^{-10} $S \cdot cm^{-1}$ for **S1**, 10^{-13} $S \cdot cm^{-1}$ for **S2** and 10^{-16} $S \cdot cm^{-1}$ for **S3**. This huge decrease in conductivity upon Zn substitution is observed in the whole investigated frequency and temperature range, i.e., in both spin states and conductivity regimes (AC and DC).
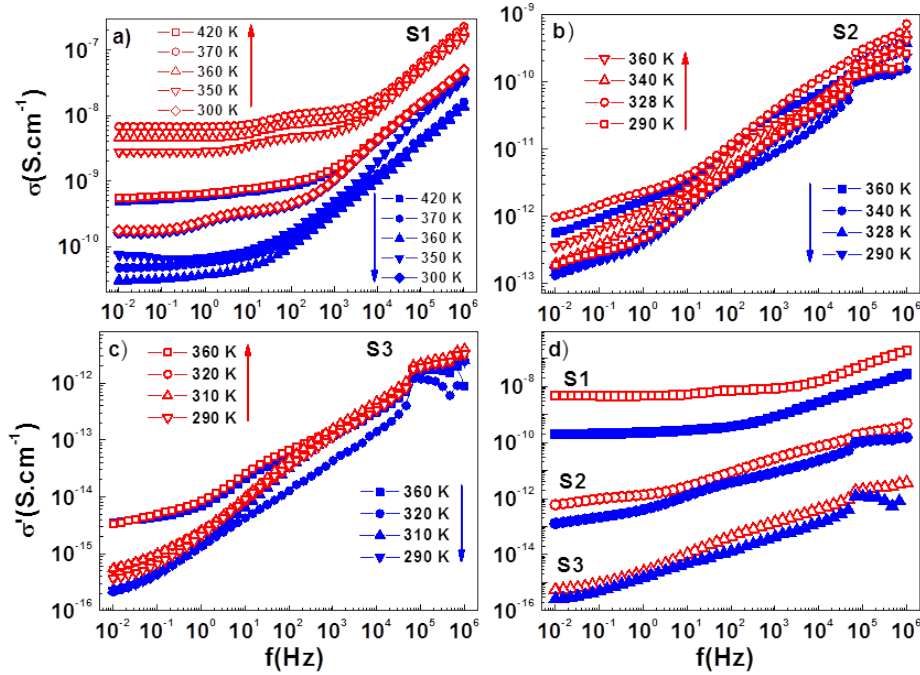
Figure 2.18: Frequency dependence of the AC conductivity at different temperatures in the heating (red open symbols) and cooling (blue full symbols) modes for samples **S1** (a), **S2** (b) and **S3** (c). Characteristic conductivity spectra in LS state (red symbols) and HS state (blue symbols) for each sample (d).
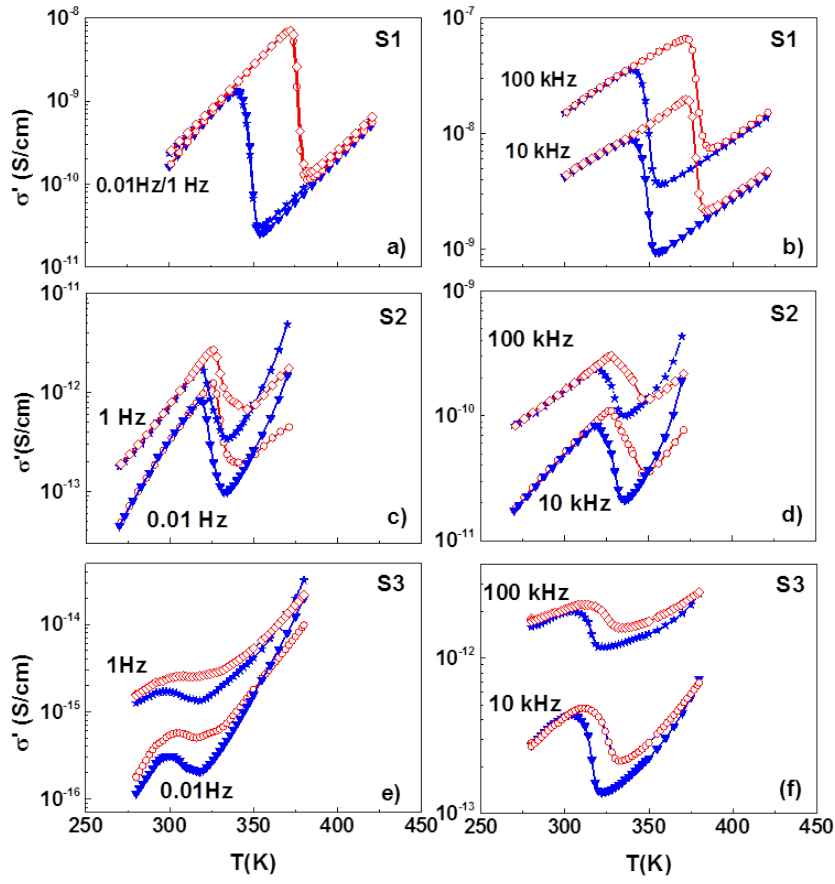
Figure 2.19: Temperature dependence of the AC conductivity for samples **S1 - S3** at low (a, c, e), and high frequencies (b, d, f).

The thermal dependence of the real part of conductivity at fixed frequencies (see Figure 2.19) shows a thermally activated behavior as well as a hysteresis loop, the width of which is strongly dependent on the Zn dilution level. Upon increasing the Zn fraction, the conductivity hysteresis loops become narrower, in reasonably good agreement with the optical reflectivity measurements (Table 2.2). At the LS-HS transition the conductivity drops by two orders of magnitude for sample **S1**, one order of magnitude for **S2** and less than one order of magnitude for **S3**. In other words the LS state is more conductive than the HS state in each sample, but as it can be expected the Zn substitution attenuates the conductivity difference between the two states. The activation energies of the conductivity were extracted at different frequencies using the Arrhenius law (see equation 2.12) as represented in Figure 2.20.

$$\sigma' = \sigma_0 exp\left(-\frac{E_\sigma}{k_B T}\right) \tag{2.12}$$

where σ_0 is the pre-exponential factor and E_σ the activation energy of the conduction process. For the three samples, the different values of E_σ obtained from the Arrhenius fit in the LS and HS states at different frequencies are reported in Figure 2.21.

56
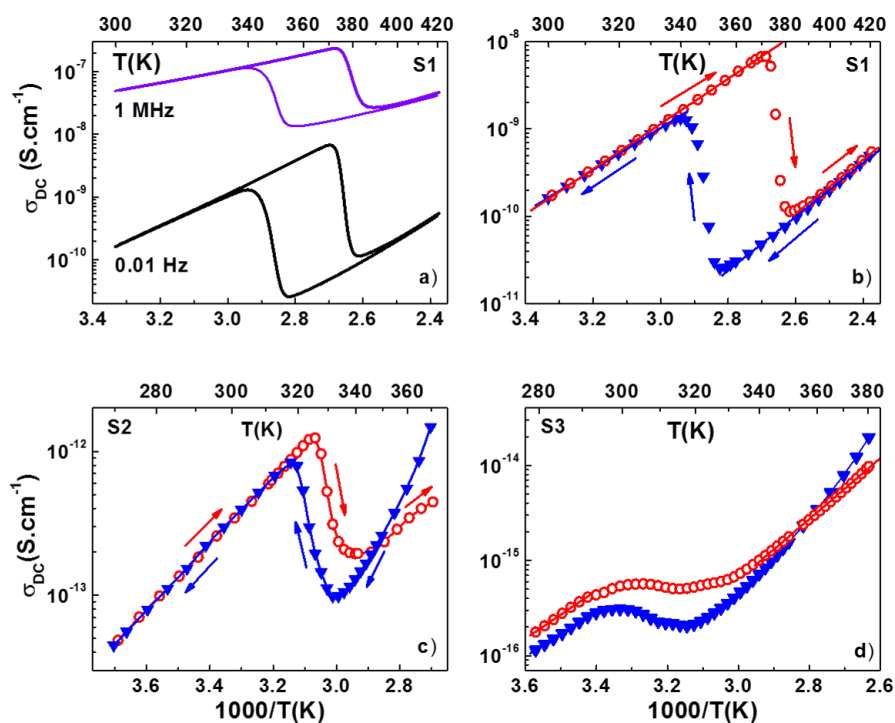
Figure 2.20: Arrhenius plots of the electrical conductivity: AC conductivity at 10^{-2} Hz and 1 MHz for sample **S1** (a), DC conductivity for samples **S1** (b), **S2** (c) and **S3** (d).
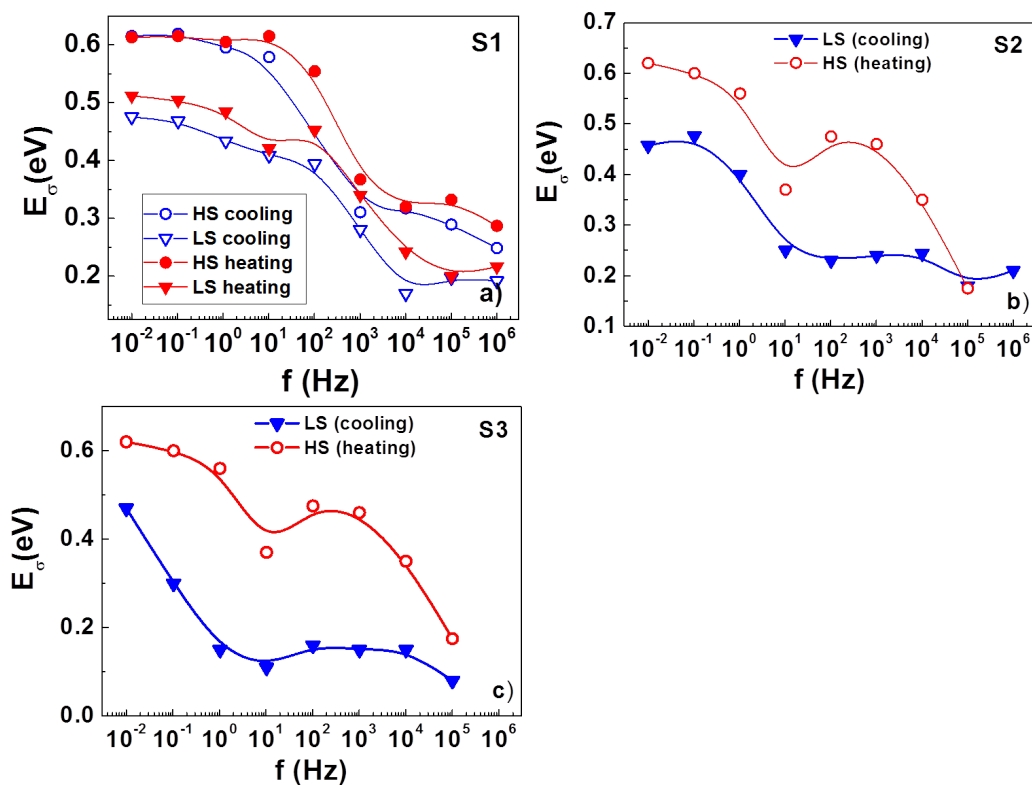
Figure 2.21: Frequency dependence of the conductivity activation energy for samples **S1** - **S3** in the two spin states.

Even if the quality of the fit becomes rather poor for samples **S2** and **S3** one can draw several important conclusions. First, the activation energy in the LS state is systematically lower than in the HS state. Second, the Zn dilution does not influences considerably the activation barriers of the conductivity. The activation energy has no frequency dependence below the cut-off frequency ω_c, but decreases strongly for higher frequencies in each sample and in both spin states. The frequency at which the activation energy varies, decreases with increasing the percentage of the Zn dilution. This observation is in good agreement with the decrease of ω_c with the dilution.

The values of ω_c and n have been extracted by a non-linear fitting procedure using equation 2.10 for each sample and each temperature. The temperature dependence of these two parameters are presented in Figure 2.22. In this figure one can observe the same hysteretic behavior related to the spin transition phenomenon. There is a clear decrease of the power law exponent n when going from the LS to the HS state, but no clear correlation exists with the Zn dilution. At room temperature (LS state) the values of n fall between 0.5 and 0.6 for each sample. The thermal variation of the hopping frequency ω_c brings more information about the charge transport mechanism in the samples. Most importantly, the hopping frequency decreases very significantly with the Zn dilution. In the LS state, the hopping frequency has been found to be 138 s^{-1} for **S1**, 0.12 s^{-1} for **S2**, and 0.01 s^{-1} for **S3**. Furthermore ω_c is always higher in the LS state, but its variation on the SCO is decreasing with increasing amount of Zn impurities. Overall the behavior of ω_c shows a clear correlation with that of the conductivity σ'. One can thus suggest that the strong decrease of the conductivity with the Zn dilution as well as by the LS to HS transition is primarily governed by the decrease of the hopping frequency.

The dispersion behavior of the electrical conductivity in the frequency domain can also be interpreted in terms of conductivity relaxation time using the electric modulus representation. The frequency spectrum of the imaginary part of the electrical modulus M", can be related to the mobility of the charge carriers [113, 114, 124, 125]. In particular the broad relaxation peak, which is often seen in the M_σ vs. f curves, represents the separation between long range (or non-localized) and short range (localized) conduction. Figure 2.23 shows the frequency response of the electric modulus at selected temperatures. It is important to notice that the spectra for each sample clearly present two overlapping peaks, which has been fitted using the Havriliak-Negami (HN) formula (equation 2.11).

The inverse of the maximum peak frequency of the M_σ spectra represents the time scale of the transition from the long-range to short-range mobility and is defined as the characteristic conduction relaxation time ($\tau_M = 1/\omega_M$). The temperature dependence of the relaxation peak frequencies is shown in Figure 2.23. For each sample, one can observe the hysteresis associated with the spin transition due to a decrease of ω_M when going from the LS to the HS state, even if this variation is attenuated for increasing Zn doping level. One can note also that the relaxation frequencies for the same temperature and same spin state decrease drastically when Zn impurities are inserted. In the LS state the values of ω_{M1} and ω_{M2} are $5 \cdot 10^2$ s^{-1} and $4 \cdot 10^4$ s^{-1} for sample **S1**, $4.5 \cdot 10^{-1}$ s^{-1} and $2.7 \cdot 10^1$ s^{-1} for sample **S2** and $8 \cdot 10^{-2}$ s^{-1} and $2.3 \cdot 10^1$ s^{-1} for sample **S3**. It is tempting to correlate in a more quantitative manner the thermal behavior of ω_M, ω_C and σ_{DC}, which are all thermally activated and show qualitatively similar evolution both with the spin transition and Zn dilution. Indeed the temperature dependence of both ω_M and ω_C obeys to an Arrhenius law

which can be described by the following equations:

$$\omega_C = \omega_{0h} exp\left(-\frac{E_h}{k_B T}\right) \tag{2.13}$$

$$\omega_M = \omega_{0M} exp\left(-\frac{E_M}{k_B T}\right) \tag{2.14}$$
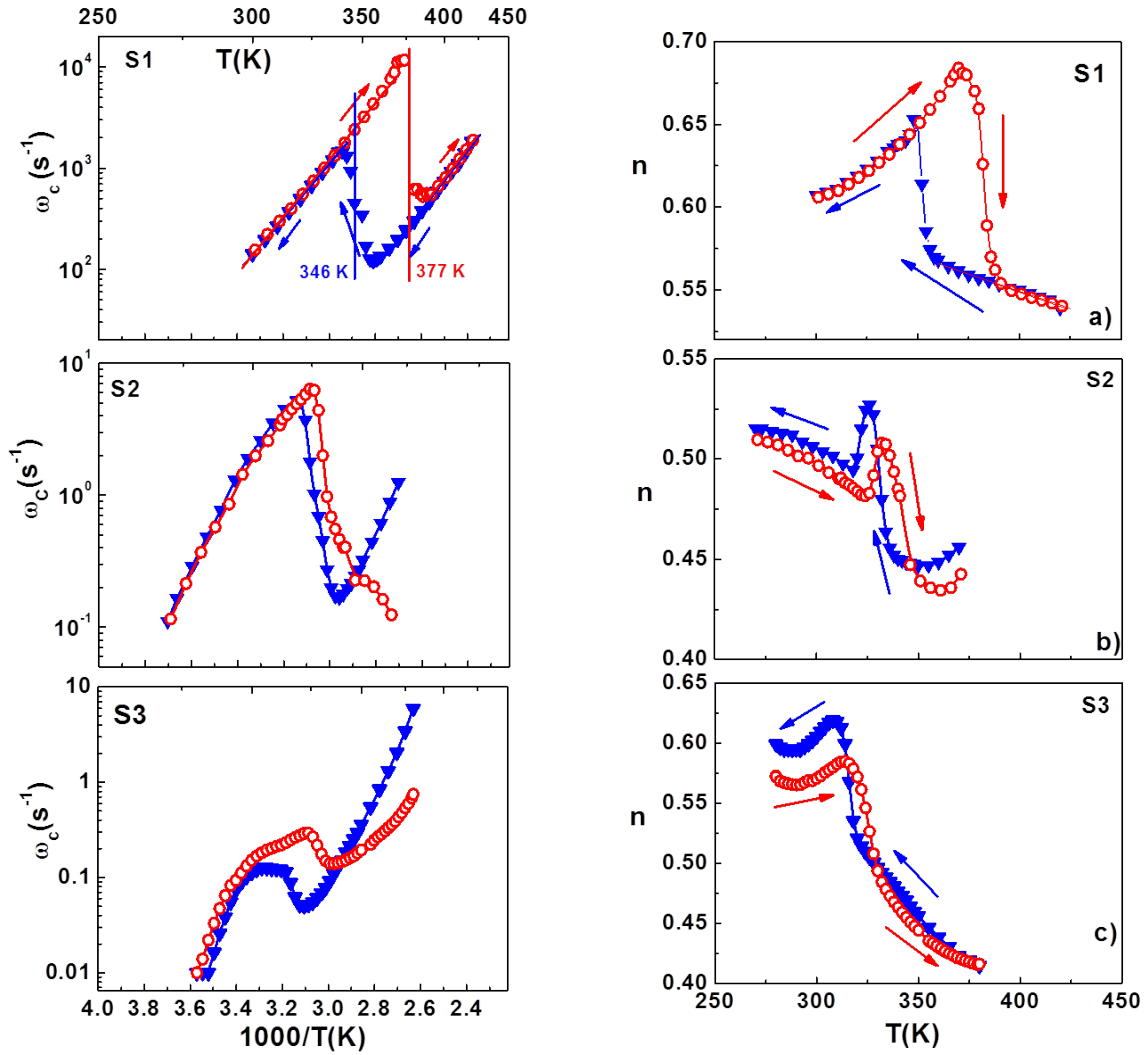
Figure 2.22: Thermal behavior of the crossover frequency ω_c extracted by fitting the real part of the complex conductivity and of the frequency exponent n for **S1**, **S2** and **S3** in both heating and cooling modes.
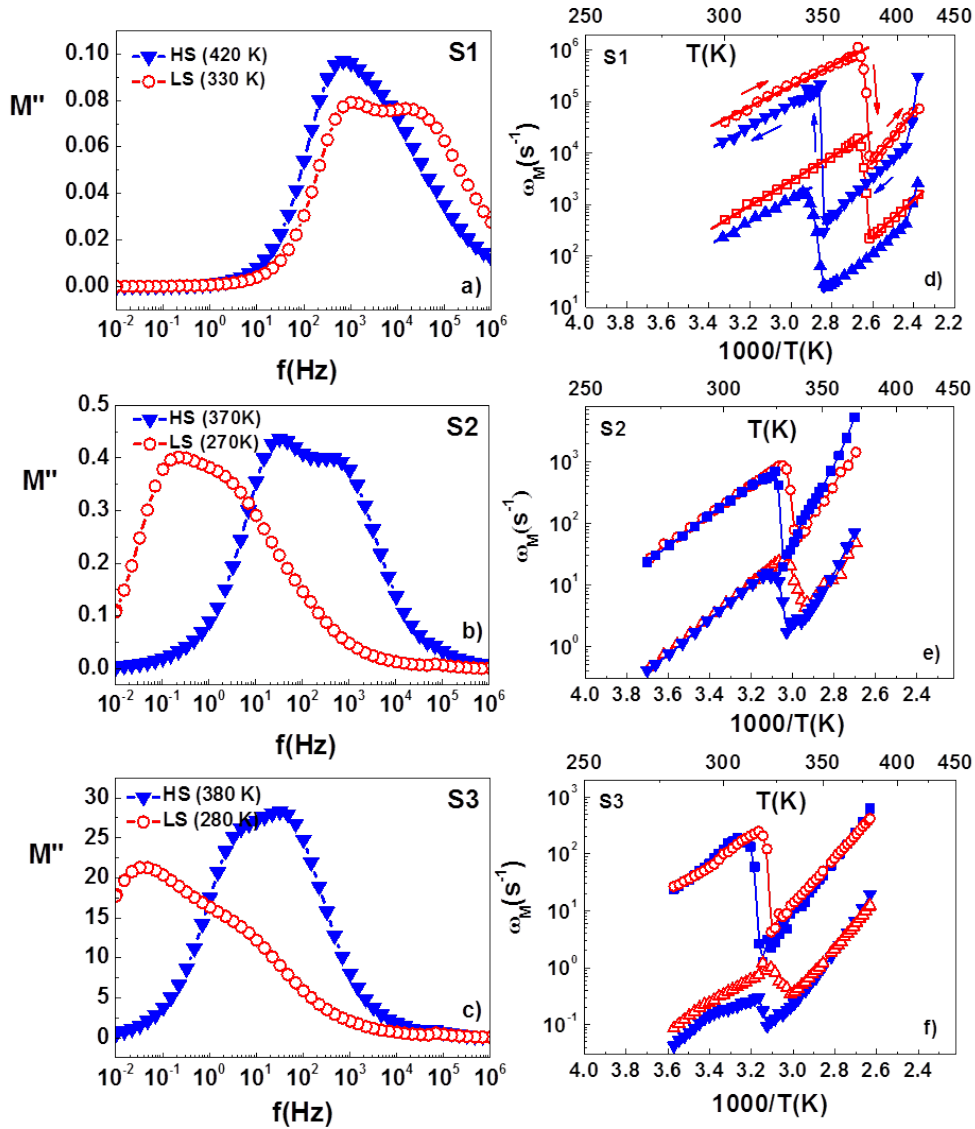
Figure 2.23: Frequency dependence of the loss modulus in the LS and HS states for samples **S1** (a), **S2** (b) and **S3** (c). Temperature dependence of the two deconvoluted relaxation peak frequencies for samples **S1** (d), **S2** (e) and **S3** (f) respectively.

Satisfactory fits were obtained for all the activation parameters (E_h, ω_{0h}) and (E_M, ω_{0M}) only for sample **S1**, which are synthesized in Table 2.3.

For this compound, the activation energies extracted from electric modulus analysis agree with the values of DC conductivity and hopping frequency activation energies. In other words similar energy barriers are involved both in the relaxation and conducting processes and it can therefore be assumed that these different representations of charge transport are equivalent. This conclusion is also supported by the very similar values obtained for the frequency pre-exponential factors. When comparing the spin-state dependence of activation parameters there is an obvious decrease of the activation energy when going from the HS to the LS state, while the spin-state dependence of the pre-exponential factors is less obvious. On the other hand, the activation energies (in a given spin state) are very similar in the pure and Zn diluted samples (see Figure 2.21). The dramatic decrease of σ_{DC}, ω_M and ω_C with the dilution cannot be thus related to a change of the activation barriers.

Table 2.3: Activation parameters for sample **S1** in the HS and LS states obtained from the Arrhenius dependence of the DC conductivity, the hopping frequency ω_c and the loss peak frequency ω_M in the heating ($\uparrow$) and cooling ($\downarrow$) modes.

Spin state	E_σ [eV]	σ_0 [$S \cdot cm^{-1}$]	E_h [eV]	ω_{0h} [s^{-1}]	E_{M1} [eV]	ω_{0M1} [s^{-1}]	E_{M2} [eV]	ω_{0M2} [s^{-1}]
HS	0.61 $\uparrow$ 0.61 $\downarrow$	10^{-2} 10^{-2}	0.59 $\uparrow$ 0.58 $\downarrow$	$2 \cdot 10^{10}$ 10^{10}	0.67 $\uparrow$ 0.64 $\downarrow$	$2 \cdot 10^{11}$ $3 \cdot 10^{11}$	0.59 $\uparrow$ 0.58 $\downarrow$	$2 \cdot 10^{10}$ 10^{10}
LS	0.51 $\uparrow$ 0.48 $\downarrow$	$6 \cdot 10^{-2}$ 10^{-2}	0.56 $\uparrow$ 0.53 $\downarrow$	$3 \cdot 10^{11}$ 10^{11}	0.47 $\uparrow$ 0.45 $\downarrow$	$4 \cdot 10^{10}$ $7 \cdot 10^9$	0.57 $\uparrow$ 0.53 $\downarrow$	$5 \cdot 10^{11}$ 10^{11}

One can suggest therefore that these changes are related either to a decrease of the charge carrier density (number of iron centers) and/or to a change of the hopping distance and the associated active phonon modes.

2.4 Conclusions

In this chapter, a thorough analysis of the charge transport properties has been made in order to better understand the dynamic behavior of charge carriers, in the SCO complex $[Fe(Htrz)_2(trz)](BF_4)$ synthesized in different forms (nano- and micro-crystalline powder) and diluted with zinc ions ($[Fe_{1-x}Zn_x(Htrz)_2(trz)](BF_4)$).

In the first part of this chapter, an unprecedented behavior of the complex permittivity upon the spin transition in the compound $[Fe(Htrz)_2(trz)](BF_4)$ was reported. It has been shown that the dielectric relaxation frequency is strongly dependent on the spin state of the complex, denoting different relaxation mechanisms, which could be related to the structural changes (lattice deformation) between the two spin states. The AC and DC conductivity, as well as the dielectric constant and the dielectric relaxation frequency exhibit a spin state dependence, with an important drop when going from the LS to the HS state. All these measured quantities represent a different facet of the charge carrier dynamics, conferring unique properties to this material and making it interesting for threshold switching and memory devices as well as thermally variable capacitors due to their hysteresis in the conductivity as well as the dielectric constant.

The substitution of the "active" Fe centers by "inactive" Zn ions lead to some important findings concerning the charge transport properties of this spin crossover compound. The metal substitution was found homogeneous and the obtained compounds appeared closely isostructural. The iron ions kept their spin transition properties in the diluted samples, but as expected a loss of cooperativity and a shift of the spin transition towards lower temperatures was observed with increasing the iron dilution by zinc. It has been demonstrated that spin crossover phenomena can be also detected through the temperature dependence of AC conductivity and dielectric loss and show that virtually all material dependent electrical parameters, such as electrical conductivity, electric modulus, cut-off frequency, relaxation peak frequency, etc. display a spin-state dependence. In particular, it has been shown that the spin transition from the LS to the HS state led to a systematic decrease of the electrical conductivity and carrier hopping frequencies, which were related to the higher values of the activation energy in the HS state. The Zn substitution of active iron centers do

not change the activation barriers, but leads to an important decrease of the charge carrier hopping frequencies, which is reflected by the drop of the electrical conductivity by ca. 6 orders of magnitude (for x = 0.43). Taking into account the close structural and morphological similarity of the pure and Zn-diluted samples these results indicate that the ferrous ions with open $3d^6$ electronic shell directly participate to the charge transport process, in contrast to the Zn(II) ions, which have a closed $3d^{10}$ shell.

Chapter 3

Elaboration and characterization of an electronic device in horizontal configuration containing $[Fe(Htrz)_2(trz)](BF_4)$ particles

Based on the results of Chapter 2 as well as some previous results in the team [31] we built a microelectronic device using the $[Fe(Htrz)_2(trz)](BF_4)$ complex. Rod-shaped micrometric particles where organized by dielectrophoresis between interdigitated electrodes and their static electrical properties were investigated. A special attention has been devoted to the study of the robustness of SCO properties both at the material and device levels. In order to exploit the switching phenomenon of these materials in memory devices or electronic switches, one needs to control the spin state of the material using fast changing signals. In particular the use of an electric field or light irradiation to drive the transition would be an important breakthrough. To this end, in the second part of this chapter, the light and electric-field induced modulation of charge transport phenomena across the bistability region is presented.

3.1 Device elaboration

3.1.1 Stability studies on the SCO compound

Before inserting the material in an electronic device one must first perform several tests on the selected complex. The robustness of the spin transition must be determined for the SCO material, i.e. if it can withstand multiple thermal cycling. Another important aspect is to observe if different experimental conditions like the use of vacuum, the presence of different solvents or the thickness of the sample will influence in some matter the transition. From these experiments one can determine the presence of the spin transition and the changes, if any, due to repeated thermal cycling, or other external conditions.

To our knowledge this type of tests has never been performed on any SCO material. Usually, the SCO is thermally induced and the relative proportion of the HS and LS molecules is recorded over a few heating-cooling cycles. The number of thermal cycles reported in the literature is usually less than 3-4 and the highest number we found was a few dozen [18]. It is well-known in the SCO field that, depending on the compound, the spin transition behavior may change or even disappear due to various phenomena (i.e.

loss or uptake of solvent molecules, irreversible structural changes or mechanical fatigue). It has been shown for example that the same compound can exist in two distinct phases, with distinct SCO properties, depending on the degree of the sample hydration [126]. A small shift of the spin transition temperature is often observed after the first thermal cycle, also known as the "run in" phenomenon, which is explained in most cases by the loss of solvents [62, 121]. The synthesis in different solvents can also lead to very different SCO properties. A nice example is given in refs [42, 127].

The spin crossover is accompanied by a significant change of the molecular volume and the associated elastic stress and strain often result in the mechanical fatigue of the material, which in turn can influence the SCO behavior. For example, a spectacular self-grinding of crystals of $Fe(L)_2[Ag-(CN)_2]_2$ (with L = 4,4-bipy) into microcrystalline powder was observed and in parallel the thermal hysteresis loop of the SCO disappeared [128]. Similar self-grinding was reported for the compound $[Fe_2(DAPP)(abpt)](ClO_4)_2$ (DAPP = Bis(3-aminopropyl)(2-pyridylmethyl)amine, abpt = 4-Amino-3,5-bis(pyridin-2-yl)-1,2,4-triazole) but the SCO properties did not change considerably [129]. On the contrary, an excellent mechanical and SCO stability has been reported for $[Fe(bapbpy)(NCS)_2]$ (bapbpy contains two fused N,N-bis(2-pyridyl)amines) crystals [130, 131] after 10 consecutive thermal cycles revealed by optical reflectivity and magnetic susceptibility measurements, respectively. Probably the most detailed stability study was reported by Kahn et al. [18] on the $[Fe(NH_2trz)_3](NO_3)_{1.7}(BF_4)_{0.3}$ SCO complex. They showed that after several dozen thermal cycles the compound did not suffer any alteration of the spin transition temperatures.

An indirect method from which we can point out the robustness of spin transition is to look at experiments which were performed on devices or materials under periodic excitation. For example Marino et al. [132] used a pump-probe optical method to investigate the dynamics of the spin transition of $[Fe(PM-AzA)_2(NCS)_2]$ single crystal. To monitor the dynamics, two delayed laser pulses are sent to the sample, one to induce the SCO and the second to detect it. Owing to the ultra-fast dynamics, a considerable number of acquisitions (hundreds or thousands) had to be averaged to obtain a good signal to noise ratio. From this experiment we can infer that the sample can withstand a considerable number of transitions (in this case photoswitches). Another indirect proof of the stability of the spin crossover is given in the paper of Gural'sky et al. [85] where a bilayer actuator device, built using an SCO/polymer composite, was actuated by a periodic applied current over several hundreds of cycles. Multiple switches were performed also on an electrical device based on $[Fe(trz)_3](BF_4)_2$ (trz = triazole) nanoparticles [35]. A cellulose composite of the compound $[Fe(Htrz)_2(trz)](BF_4)$ was also investigated for its reversible thermos-chromic properties and the color change was detected even after 1000 thermal cycles [133].

The robustness of the SCO phenomenon was studied by performing multiple variable temperature optical reflectivity measurements. This consists in detecting the color change of the complex by varying the sample temperature. The experimental setup is illustrated in Figure 3.1 and consists in a liquid nitrogen cryostat (Linkam HFS600E-PB4), a stable light source (in this case a 100 W halogen lamp) and a stereo-microscope with a 1.3 MP CMOS Motic camera.
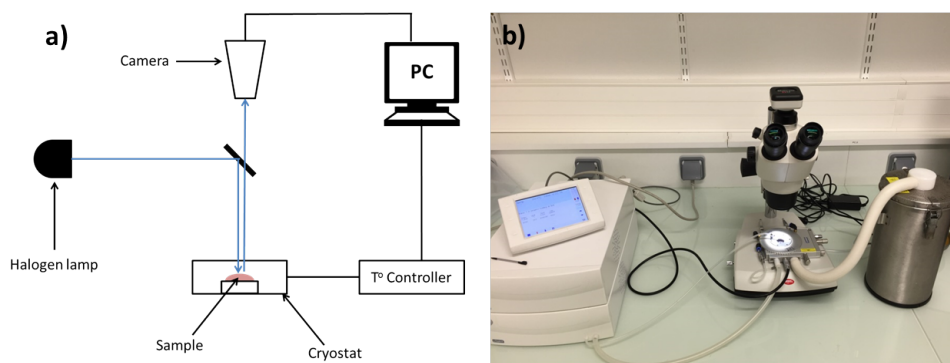
Figure 3.1: (a) Schematic representation of the variable temperature reflectivity setup. (b) Photo of the experimental setup.

Figure 3.2a illustrates the reversible color change of the complex. The sample changes its color from pink in the LS state (at low temperature) into white in the HS state (at high temperature). A 540 nm filter has been used in order to increase the contrast between the two spin states. Figure 3.2b shows the hysteresis cycle for the first and the last three registered thermal cycles. The temperature of the sample was varied between 290 K and 430 K in air atmosphere with 5 K/min and an image was acquired each degree. A region of the image containing the sample was selected and an integration of the intensity of each pixel was performed in order to get the reflectance value. The transmission electron microscope (TEM) image (see Figure 3.2c) shows the size of the particles which is around 1 - 1.5 μm. The thermal behavior of this sample presents the well-known shape, with a wide hysteresis above room temperature. In heating mode, the reflectance of the considered sample (at 540 nm) is weak until 390 K where it starts to increase due to the spin transition, until it saturates. In cooling mode the reflectance of the sample remains constant until 350 K where it drops back to the initial value.
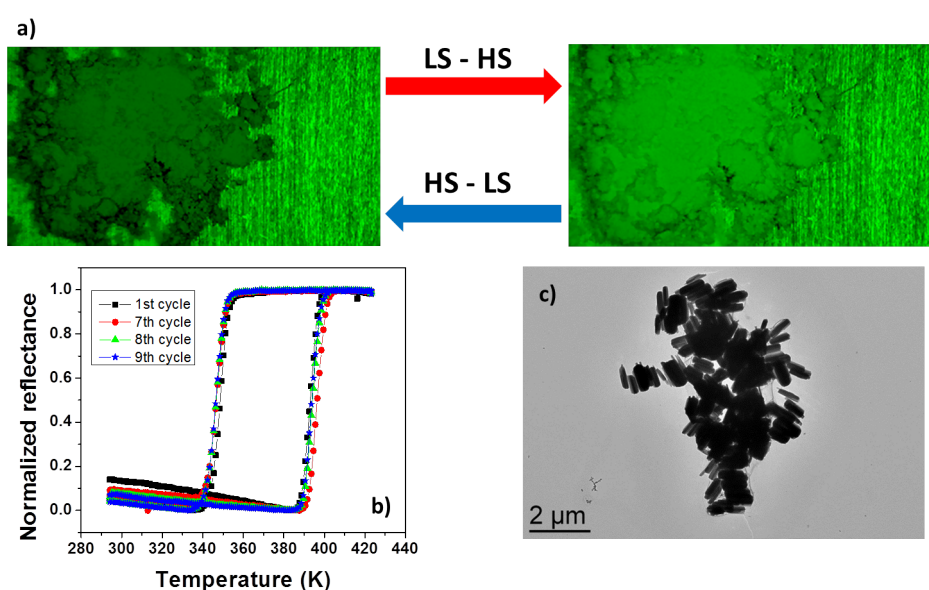
Figure 3.2: a) Color change of $[Fe(Htrz)_2(trz)](BF_4)$ due to spin crossover phenomena recorded using a 540 nm filter. b) Thermal dependence of the optical reflectivity recorded during multiple cycles in air. c) TEM micrograph of the sample.

In order to confirm the thermal and time stability of the compound, a series of 3000 consecutive thermal cycles were performed on the sample after it has been stored, in air and at ambient temperature for three years. The results are rather surprising (Figure 3.3), as one can see a shift of the HS to LS transition temperature, while the LS to HS transition remains practically unchanged. Even though the transition temperature shifts, the sample still presents a hysteretic behavior even after 3000 thermal cycles, which can be exploited for applications.
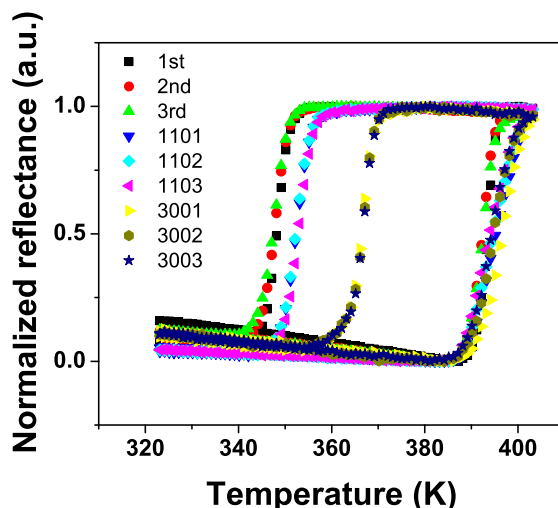
Figure 3.3: Thermal hysteresis of $[Fe(Htrz)_2(trz)](BF_4)$ corresponding to the spin transition before and after 1100 and 3000 consecutive cycling.
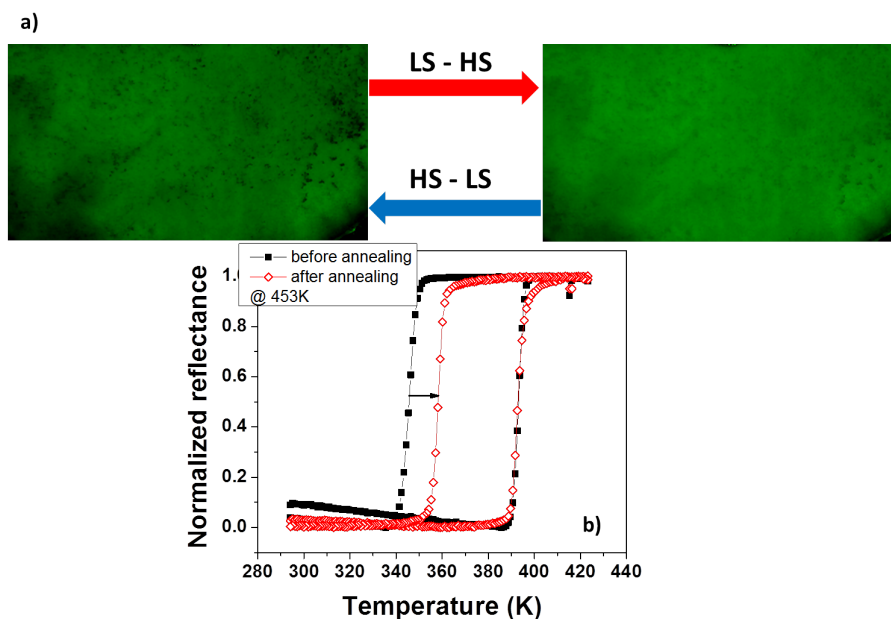
Figure 3.4: a) Optical images of the $[Fe(Htrz)_2(trz)](BF_4)$ sample after anealing in nitrogen atmosphere (dark spot represent degraded sample). b) Consecutive thermal hysteresis loops registered before and after annealing.

Another stability experiment was performed on a much thinner layer of the compound. The particles have been dispersed in ethanol and the solution was drop casted on a glass slide. The thermal hysteresis cycle has been recorded before and after subjecting it to thermal annealing for 3 hours to 453 K under a constant flow of dry nitrogen. A shift of the HS to LS transition to higher temperatures has been observed. This shift can be attributed to a partial degradation of the sample (see the dark spots in optical images from Figure 3.4.

The annealing temperature has been increased to see if the sample suffers further and the sample has been kept at 473 K for 3 hours in nitrogen atmosphere, and the resulting effect was a loss of SCO properties, i.e. the sample did not present any color change, and the dark regions are more pronounced. Figure 3.5 illustrates the registered heating and cooling branch after this thermal treatment. The color of the sample remains the same in the whole temperature range, with many dark regions, indicating a chemical degradation of the sample. The degradation of the compound due to thermal treatment has been confirmed by Fourier Transform Infrared (FTIR) spectroscopy (see Figure 3.6), where one can see a modification of the peaks between 3200 and 2400 cm^{-1}, 1700 and 1300 cm^{-1} as well as 1000 and 700 cm^{-1}.
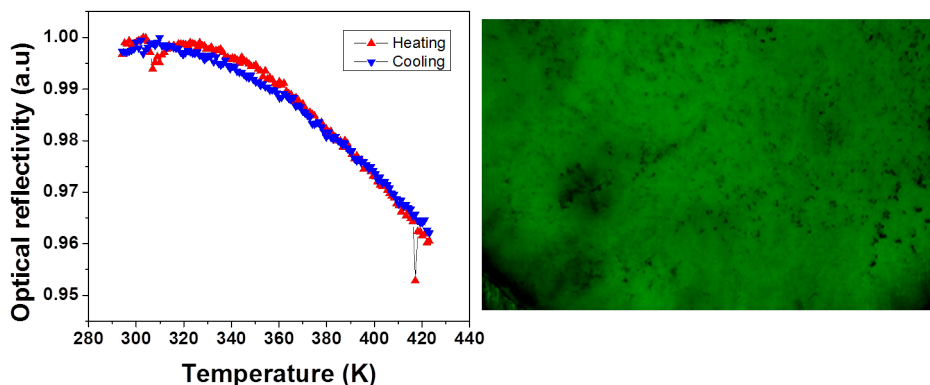
Figure 3.5: The thermal dependency of reflectivity and image of the $[Fe(Htrz)_2(trz)](BF_4)$ sample after 3 hours anealing at 473 K in nitrogen atmosphere.
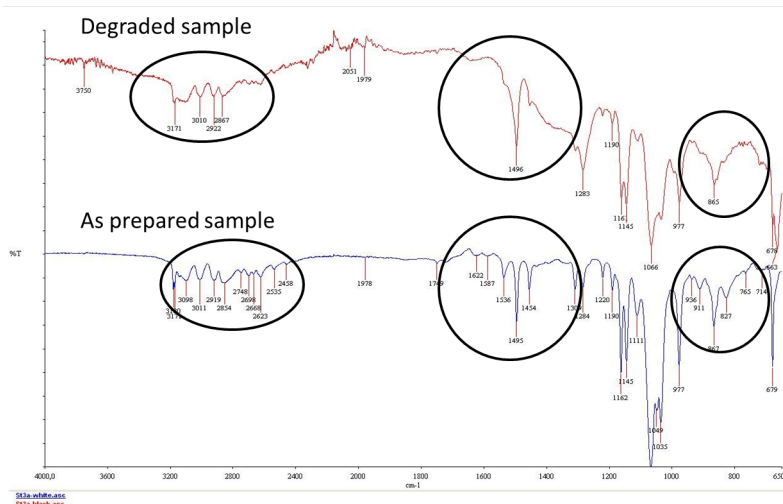
Figure 3.6: FTIR spectra of thermally anealed (473 K) and as prepared sample.

The thermal variation of the reflectivity of the sample deposited on a glass slide using ethanol and water was compared in order to see if the different solvents influence the spin transition properties. The thermal hysteresis loops were registered in the same time to better compare the curves. This comparison is presented in the Figure 3.7 where no influence of the solvents on the SCO properties can be observed.
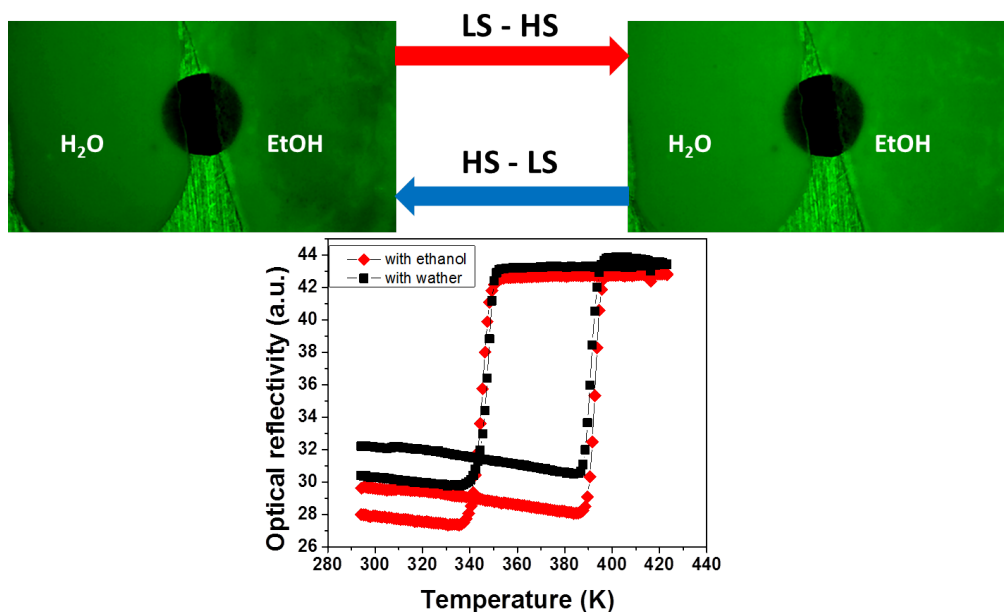
Figure 3.7: Optical images and thermal hysteresis for the sample dispearesd in water and ethanol.

Interestingly enough, by subjecting the thin deposited sample to a secondary vacuum of $7.5 \cdot 10^{-9}$ bar the sample does not suffer the same degradation after high temperature treatment (3h at 453 K and 473 K) as shown by the thermal cycles registered before and after thermal treatment (Figure 3.8a).
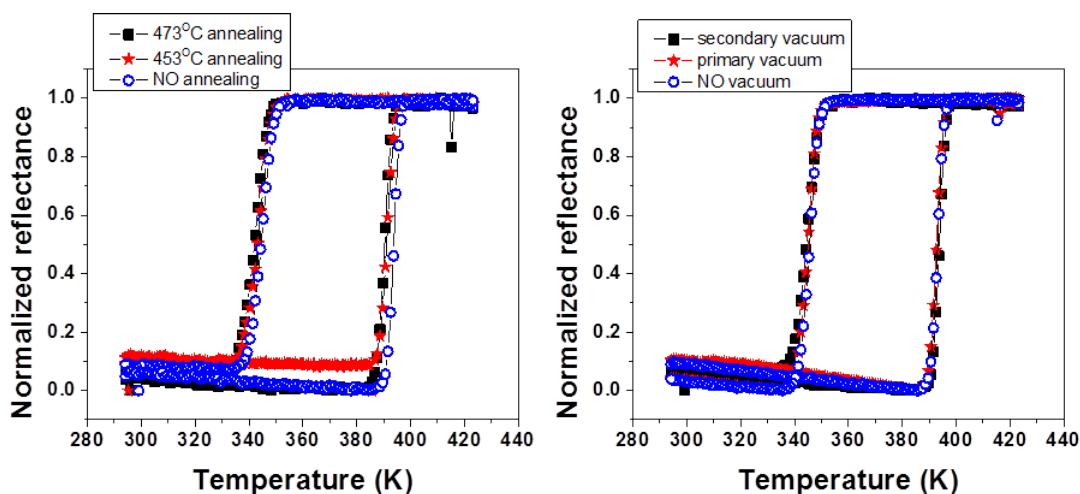
Figure 3.8: (a) Effect of thermal annealing at 453 K and 473 K on the SCO behavior of the sample treated previously in secondary vacuum. (b) Thermal hysteresis loops of $[Fe(Htrz)_2(trz)](BF_4)$ registered after primary and secondary vacuum treatment.

Moreover, placing the sample in vacuum did not change the transition temperatures (Figure 3.8b). This phenomenon might by explained by the fact that by keeping the sample in vacuum all traces of remaining solvents are removed and the sample becomes more stable.

From this stability study on the sample one can draw some important conclusions. The first observation is that these optical measurements reveal a very reproducible SCO behavior, i.e. the spin transition temperatures remain in the same temperature region after numerous cycles. In order to obtain this reproducibility, the sample must not be subjected to temperatures higher than 420 K. Moreover, by dispersing the particles in ethanol or water, the SCO properties are not influenced. Finally, subjecting the sample to secondary vacuum ($7.5 \cdot 10^{-9}$ bar), did not influence the transition temperatures, but it made the sample more resilient to high temperatures (473 K).

3.1.2   Dielectrophoresis technique

As recently reported by Rotaru et. al, the possibility of successfully organizing high aspect ratio rods of $[Fe(Htrz)_2(trz)](BF_4)$ between interdigitated electrodes, with a high degree of orientation [36] represents a promising perspective towards the the understanding of the electrical behavior of these materials. To this aim they used dielectrophoresis, which consists of organizing SCO particles dispersed in an ethanol solution between interdigitated electrodes using an electric field. Electronic devices have been constructed using different electrode morphologies (different electrode gaps) and different particle sizes, but the best result was obtained using high aspect ratio particles, with the length comparable to the electrode gap size (between 1.06 and 1.6 the size of the electrode gap). Indeed the highest orientational order parameter (S = 0.86) was obtained for the sample with 3.1 ± 0.7 μm on interdigitated electrodes with 4 μm gap. By performing dielectrophoresis on smaller aspect ratio particles (250 nm long and 100 nm wide) on electrodes with 4 μm gap and 100 nm gap they observed an important decrease of the order parameter (S = 0.09 and S = 0.16 respectively). This decrease in the order parameter is due to a negligible or negative torque.

In this thesis we elaborated similar devices. Interdigitated gold microelectrodes were fabricated by conventional photolithography and liftoff techniques. Due to the fact that in our experiments the particle size was changed with respect to [36], the efficiency of dielectrophoresis was re-evaluated. The particles were dispersed in ethanol, obtaining a solution with a concentration of 2 g/L. The solution was dropcasted on the electrode and the electric field was applied through two gold tipped tungsten micro-probes from a signal generator. After 10 s the excess solution was removed and the electric field was interrupted. The same process was repeated for each electrode pair. Figure 3.10 shows the results of the dielectrophoresis test carried out at different frequencies for an applied voltage of 7.5 V. In the first case, where the frequency is 10 Hz (a), one can see that the particles are repelled by the overlapping region of the electrodes and attracted on the surface of the electrodes. By increasing the frequency to 1 kHz (b), a change in the dielectrophoresis process was observed.
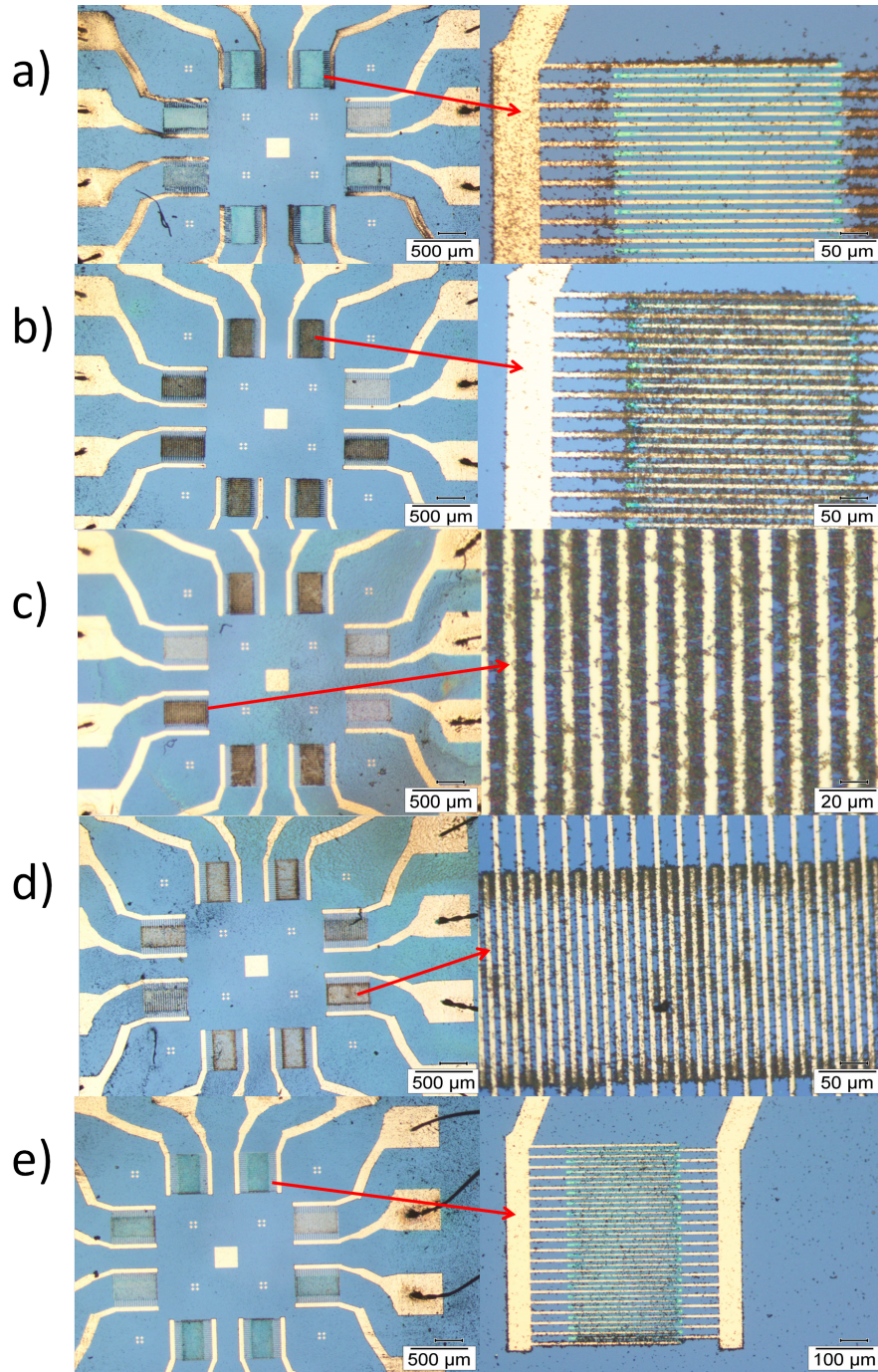
Figure 3.9: Optical images of SCO particles organized by dielectrophoresis, performed at 7.5 V and (a) 10 Hz, (b) 1 kHz, (c) 10 kHz, (d) 100 kHz and (e) 1 MHz.

The particles are both deposited on the gold electrodes and also between them. At 10 kHz (c), the particles are primarily organized in between the electrodes and clearly form bridges between adjacent electrodes. Similar observations have been made for 100 kHz, where the particles still tend to align between electrodes, but mainly towards the tip of the electrodes. Finally at 1 MHz (e) the particles were deposited between the last two overlapping electrodes.

At low frequencies, this system exhibits a positive dielectrophoresis, where the particles are attracted to the gold electrodes. Then by increasing the frequency, the particles are subjected to a stronger negative dielectrophoresis, where the particles are preferentially

organized towards the end of the electrodes where the electrical field intensity is higher
[134–137]. Even though the size of the particles has been diminished to 0.25 of the size
of electrode gap, an homogeneous deposition at 10 kHz (7.5 V applied bias) has been
obtained, which was the frequency used for elaborating all the experimental devices.

The voltage analysis (see figure below) reveals that regardless of the voltage used (1
V, 3 V, 5 V and 7.5 V) the particles will be organized between the electrodes. A voltage of
1 V, 3 V, 5 V and 7.5 V was applied on different electrodes and no clear dependence on the
applied voltage has been observed on this system. On the other hand a clear difference is
seen between the electrodes that were connected to a voltage and those who were not. On
the electrodes with no voltage applied, one can see no sign of dielectrophoresis.
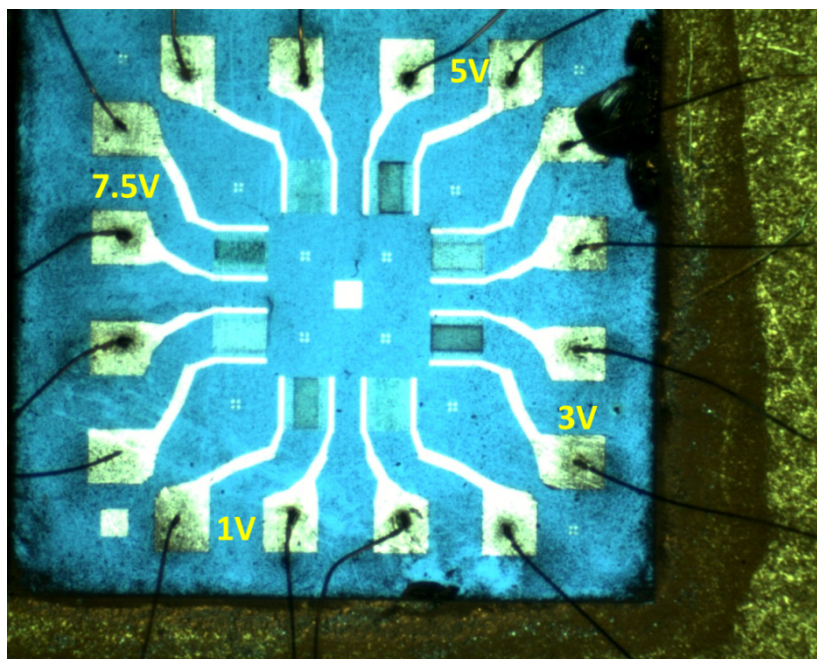
Figure 3.10: Dielectrophoresis at different voltages (1 V, 3 V, 5 V and 7.5 V at 10 kHz)
performed on 4 out of 8 electrode pairs. The remaining electrode pairs are not connected
to any voltage supply.

3.2 Device characterization

3.2.1 Spin crossover effect on the electrical device

The resulting devices were used to measure the electrical properties and to determine if the device will present the intrinsic properties of this material. The micro-electronic devices were measured in a cryogenic cell equipped with gold tipped tungsten electric probes (Linkam HFS600E-PB4) and a sub-femtoamp remote source-meter (Keithley 6430) was used to apply the bias and to measure the current in the device. The temperature of the sample and the current through the device were measured simultaneously using a Labview program. It is well known that a loss of material properties can be observed when the particle or molecule is connected to an electrode [4]. Therefore, multiple thermal cycles were performed between 290 K and 410 K on the device and registered the current through the particles due to an applied bias of 20 V. The result is presented in the figure below.
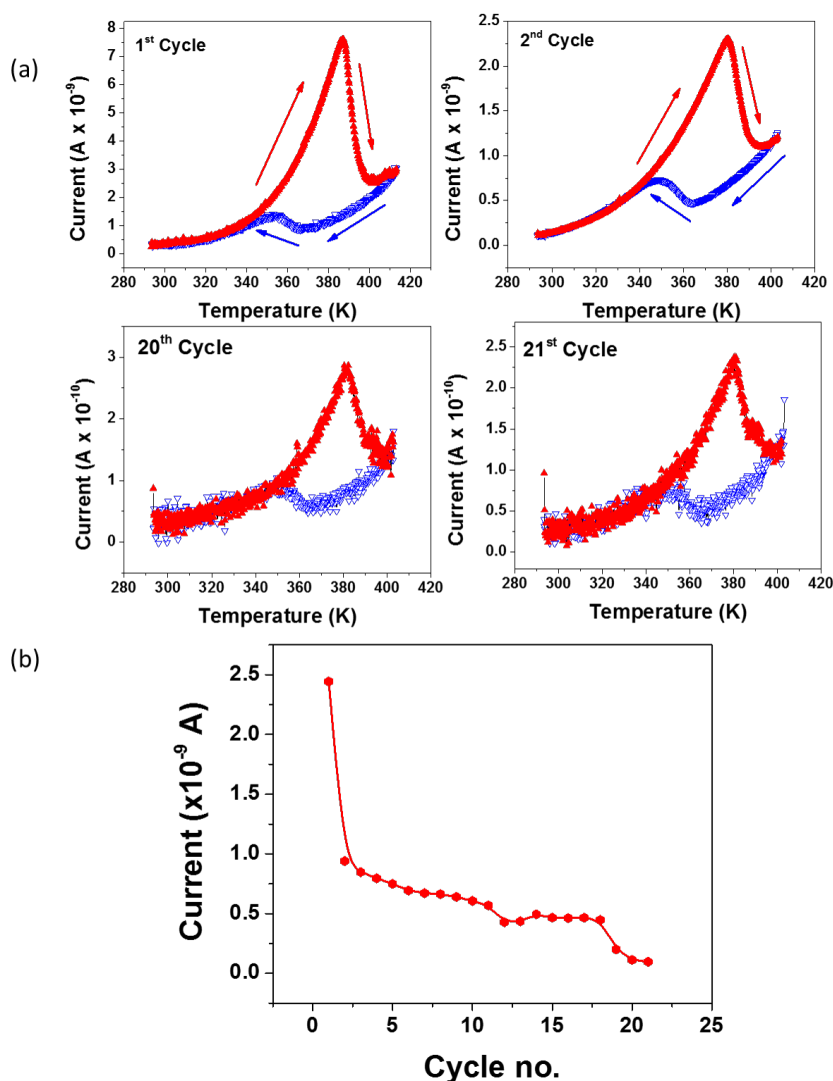
Figure 3.11: (a) Selected current vs. temperature characteristic of the electronic device over consecutive thermal cycles. (b) Variation of the mean current intensity recorded in heating mode during 21 consecutive thermal cycles.

The I-T curve of the obtained micro-electronic device is presented in Figure 3.11a. The shape of the curve is similar to what it has been reported on a similar complex (C1 from ref [31]) and presents a strong thermally activated behavior with increasing temperature. The current increases exponentially from 0.3 nA to 7.6 nA at 387 K, where it drops abruptly at 2.5 nA at 402 K, which is a clear indication of the LS to HS transition. In the cooling mode, the current presents a slightly less thermal activation, and around 367 K the current starts increasing from 0.8 nA to 1.3 nA at 352 K, which is consistent with the HS to LS transition.

In order to test the stability of the elaborated electronic device, we have completed a large number of thermal cycles, in both heating and cooling modes between 290 K and 410 K. Figure 3.11 shows the device characteristics up to 21 cycles. On one hand, the spin transition temperatures remain stable after the thermal cycling, which denotes that the particles in our electronic device still present the spin transition properties. On the other hand, the current intensity decreases progressively with each thermal cycle. This denotes that our device suffers a modification during each thermal cycle. Figure 3.11b shows the variation of the mean electrical current value on the heating branch. One can clearly see that there is a significant decrease in current values from 2.45 nA to 0.93 nA between the first and second thermal cycles, followed by a more progressive decrease down to 0.09 nA for the 21st cycle. There are many possible causes of this current decrease in the electrical conductivity and individual effects are hard to point out. The main cause may be the loss of particle/particle and particle/electrode contacts due to the thermal cycling or a degradation of the compound due to the current passing through the particles. It should be noted finally that these tests were carried out using a fixed applied bias (20 V) and temperature rate (5 K/min) and it is possible that by changing these parameters some improvement can be also obtained.

3.2.2   Light induced modulation of charge transport

In this section the effect of light irradiation on the electrical conductance of micro-rods of the spin crossover $[Fe(Htrz)_2(trz)](BF_4)$ coordination network, organized between interdigitated gold electrodes is reported. Experiments were carried out by irradiating the sample with different wavelengths (between 295 and 655 nm) either in air or under a nitrogen atmosphere.

The spin transition properties of the powder sample used for device preparation have been verified using variable temperature (5 K/min heating and cooling rates) diffuse reflectivity measurements around 540 nm, since the LS state has significantly higher absorbance in this spectral region. As shown in Figure 3.12a the LS to HS and the HS to LS transitions occur around 383 K and 340 K, respectively in good agreement with our previous measurements (see Figure 2.5 and 3.2b). Also the current - temperature characteristic was recorded and the shape of the hysteresis is in good agreement with optical measurement and also with the previously measured curves. The electrical conductivity is strongly thermally activated and the LS state is significantly more conductive (Figure 3.12b). The spin transition temperatures (339 K and 381 K) inferred from the electrical measurement are in good agreement with the optical data.

The experimental setup used to study the light irradiation effect on the devices is presented in Figure 3.13. It consists of a 100 W Xe lamp, an IR filter, in order to prevent the heating of the sample, and an optical fiber. At the end of the optical fiber various optical filters with different wavelengths and a mechanical shutter were mounted. The sample was

irradiated through the fused silica window of the cryostat and the current was recorded
before, during and after the light irradiation at a fixed temperature and a fixed bias.
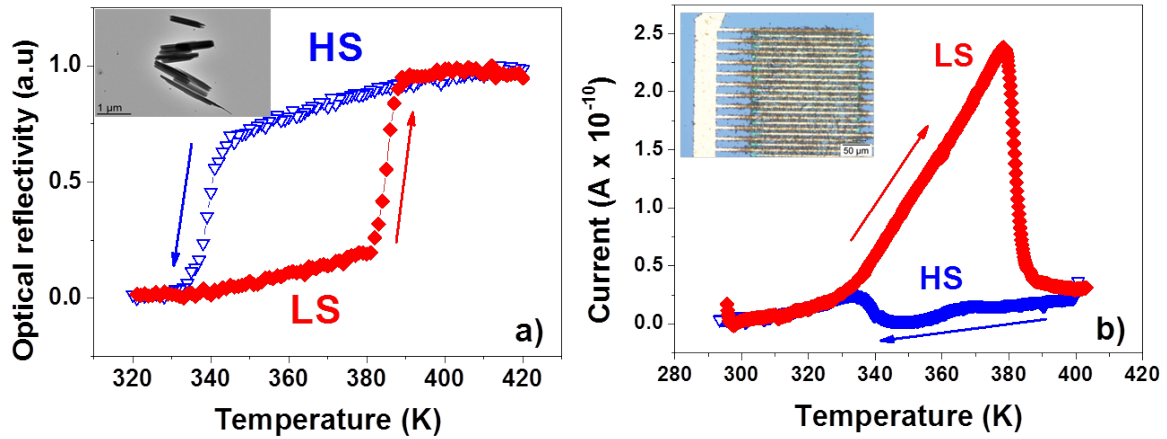
Figure 3.12: (a) Temperature dependence of the optical reflectivity (λ = 540 nm) of the
powder sample $[Fe(Htrz)_2(trz)](BF_4)$ in the heating and cooling modes. The inset shows
a TEM image of the particles. (b) Temperature dependence of the current intensity (at U
= 20 V) in the device in the heating and cooling modes. The inset shows the photo of the
interdigitated electrode device with the particles.
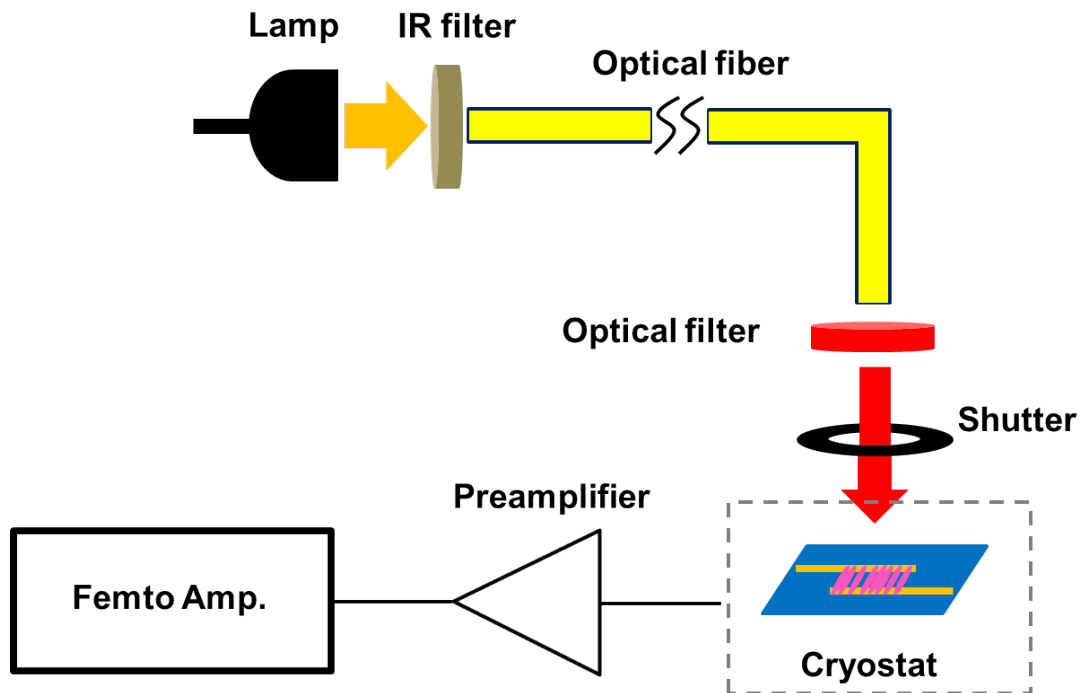
Figure 3.13: Schematic representation of the experimental setup used for the variable tem-
perature photocurrent measurements.

Typical current-voltage characteristics of the device are reported in Figure 3.14. The I-V curves have been recorded in the LS state at 368 K both in the dark and under light exposure. In both cases an Ohmic response was observed, however a lower current intensity (higher resistance) was measured under light irradiation. This contrasts the results obtained with other synthesis batches reported in [36] where a nonlinear I-V curves where found
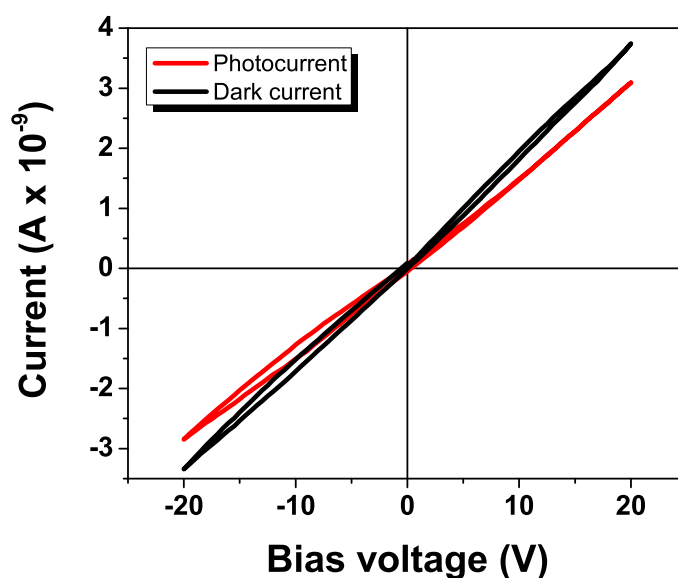
Figure 3.14: I-V characteristics of the device in dark and under light irradiation (full spectrum) recorded in air at 368 K in the LS state.

The light effect was studied inside the hysteresis loop at various temperatures, where the device was exposed to different wavelengths for a period of time. Figure 3.15 shows the typical response of the device at 368 K both in the heating (LS state) and cooling (HS state) modes. (These experiments have been repeated on several different electrode arrays and for several times on the same electrode array. Similar results were obtained in each case.)

It has been also verified that such current drift does not occur when the sample is kept in dark. Figure 3.16 shows the response of this device, in time with and without light.The experiment started in dark, with no light shining on the sample and one can see in both cases that the current does not present any drift. Also, the voltage bias has been interrupted in order to see if the current drift registered in the dark is an effect of the applied bias, but one can notice that the current presents the same evolution, therefore is an effect independent of the applied bias.
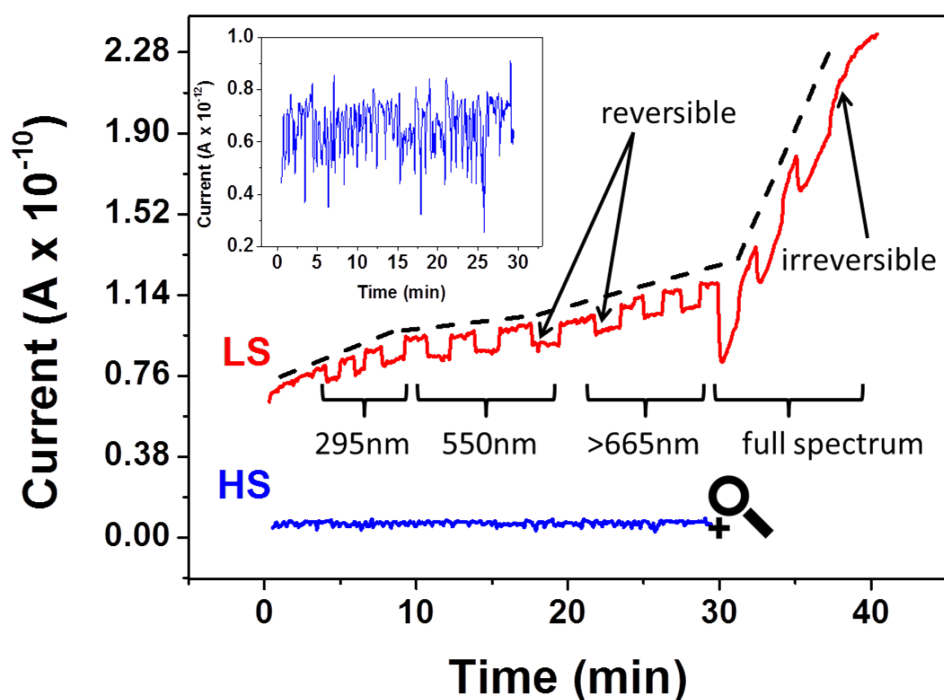
Figure 3.15: Current flowing in the device under light irradiation (20 V bias voltage). Light was successively turned on and off at different wavelengths - indicated in the figure. All data was recorded at 368 K in air both in the HS and LS states. The inset shows a zoom of the current in the HS state. In the LS state both reversible and irreversible photoconductivity phenomena are observed. The dashed line is an "eye guide" of the irreversible behavior.
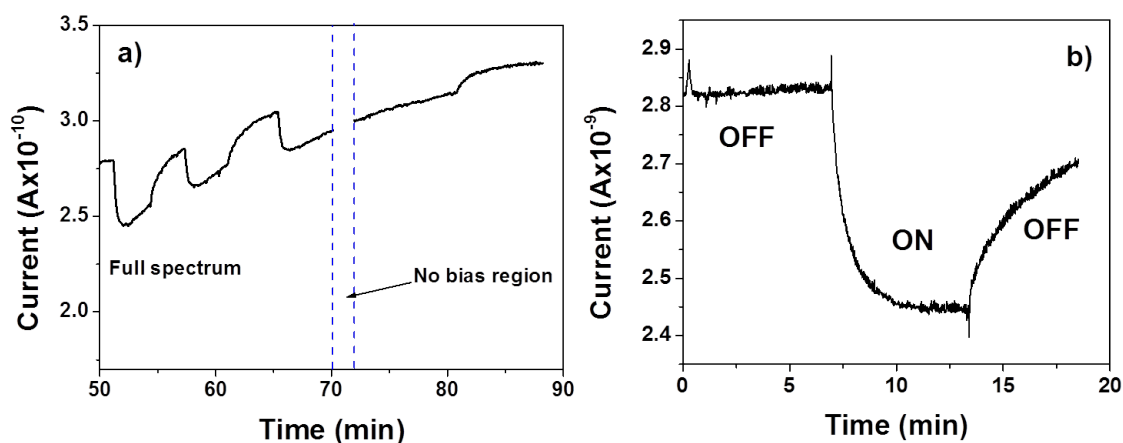
Figure 3.16: a) Photocurrent variation recorded in air at 368 K during light irradiation with full spectrum. Between 70 and 72 minutes the voltage bias was cut off. The current drift tendency was not changed by bias removal. b) Current intensity measured in dark (OFF) light (ON) dark (OFF) sequence at 368 K in LS state. The current drift is not present in the first OFF region. In the ON region the sample was irradiated with light and the current intensity dropped. When the light was switched OFF the current does not recover in the same manner, instead it presents an increasing current drift.

These experiments were repeated in the same conditions (temperature, light exposure and applied bias) in the HS state as well, however no effect of light has been observed (see Figure 3.15). However, the current intensity in the HS state (7 pA) is very low when compared to that in the LS state (≈ 100 pA). Taking into account the measurement noise (≈ 1 pA) we cannot detect reliably small ($< 40\%$) current intensity variations in the HS state.This conclusion has been reached by taking the current intensity distribution in dark in the HS state and determining the standard deviation. The detection limit of the current has been defined as three times the standard deviation. In other words even if there is a light-induced effect in the HS state it might be masked by the noise. The data of the current intensity values, the fit using LogNormal distribution and the fit values are presented below.
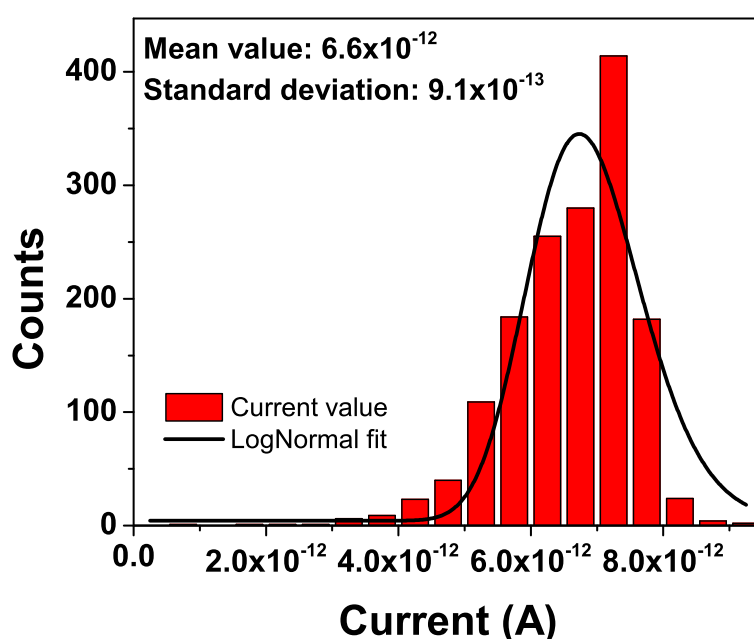
Figure 3.17: Current intensity distribution in the HS state and lognormal fit. The detection limit of the photocurrent is defined as three times the standard deviation of the dark current, i.e. 2.7 pA, which is *ca.* 40 % of the current intensity (6.6 pA).

The current drop was also investigated in the LS state under light exposure at other temperatures. Under full spectrum irradiation we obtained 0 %, 4.4 %, 7.5 % and 4.0 % current decrease at 293, 343, 363 and 383 K respectively (in the LS state). As shown in Figure 3.12b the current in the device is the highest around 368 K, hence this temperature dependence of the photoeffect indicates its possible correlation with the current intensity. Since the carrier density does not vary much with temperature in this system this result suggests that the photoeffect is correlated with the mobility of the charge carriers. Figure 3.15 shows also the influence of the wavelength of the light on the photoeffect (see also Table 3.1 and Figure 3.18).

These wavelengths were selected since this SCO compound has a strong charge transfer absorption band in the LS state around 280 nm and a ligand-field absorption band around 550 nm, while it has a weak absorption in the near IR (700 - 800 nm) in the HS state. Nevertheless, no clear correlation between the current response and the absorption spectra of the complex has been observed: Apparently in the LS state photoeffects can be generated

through the entire UV-visible-NIR spectral range.

Table 3.1: Light-induced current intensity variation for three consecutive light exposures of different wavelengths and under full spectrum irradiation, recorded in air at 368 K in the LS state.

Wavelength	295 nm	550 nm	665 nm	Full spectrum
1st **light exposure**	12%	15%	14%	55%
2nd **light exposure**	13%	15%	16%	24%
3rd **light exposure**	13%	15%	15%	24%
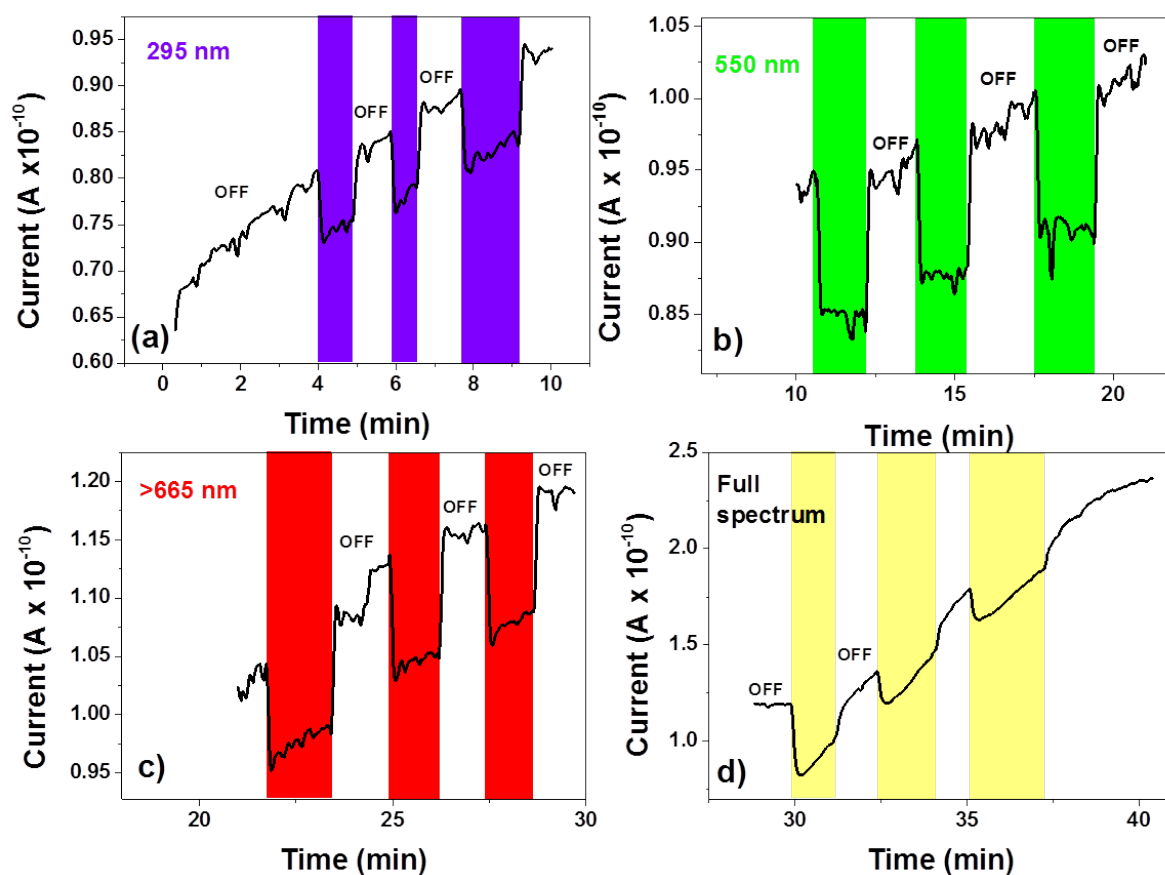
Figure 3.18: Photocurrent variation recorded in air at 368 K during light irradiation at different wavelengths: a) 295 nm b) 550 nm, c) > 665nm and d) full spectrum.

A similar behaviour has been observed in dry nitrogen atmosphere as in air, i.e. a reversible decrease of the current during the light irradiation and a continuous irreversible increase of the current (Figure 3.19). However, the decrease in the current magnitude under light was always higher in air atmosphere. As shown in Figure 3.19 the decrease of the current when the device is first exposed to light is significant (28%) even in nitrogen, but the next on/off switches lead only to a change of about 7%. These observations indicate that the reversible photoeffect phenomenon might be favored by the adsorption/desorption

of oxygen and/or humidity on the surface of the particles. Somewhat similar findings have been reported in the literature for other materials [138–140] and explained by oxygen-related surface charge traps. Such surface redox reactions may thus also play a role in the case of this device.
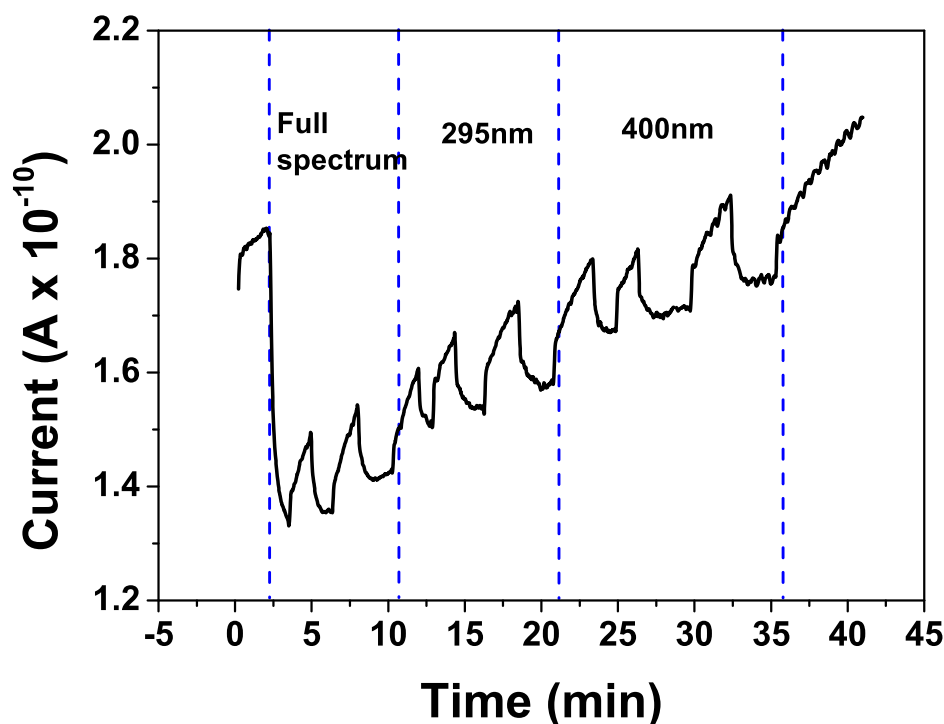
Figure 3.19: Current flowing in the device under light irradiation in nitrogen atmosphere (20 V bias voltage). Light was successively turned on and off at different wavelengths as indicated in the figure.

It is worth mentioning that photo-current phenomena in the same SCO compound have been reported by Etrillard et al. [32] (See also Section 1.2.2). They investigated particles (ca. 500 nm length and 100 nm width) synthesized using surfactants and reported in contrast to these results - a room temperature photo-conductance process with a significant increase in the electrical current during the light irradiation. However, no temperature (i.e. spin-state) dependence of the conductance has been reported.

3.2.3 Unidirectional spin state switching of the electronic device

We have also investigated the possibility of electric field induced switching of spin states within hysteresis region. To this aim, new devices were made using the previously discussed method. Again we started the investigation with the control of the starting powder sample.

The thermal behavior of the optical reflectance of the powder is shown in Figure 3.20, presenting the onset of switching from the LS to HS state at 107 ^{o}C and the reverse switching from the HS to LS state around 71 ^{o}C. This wide, abrupt and reproducible thermal hysteresis loop observed above room temperature is very similar to the ones shown before on other synthesis batches.
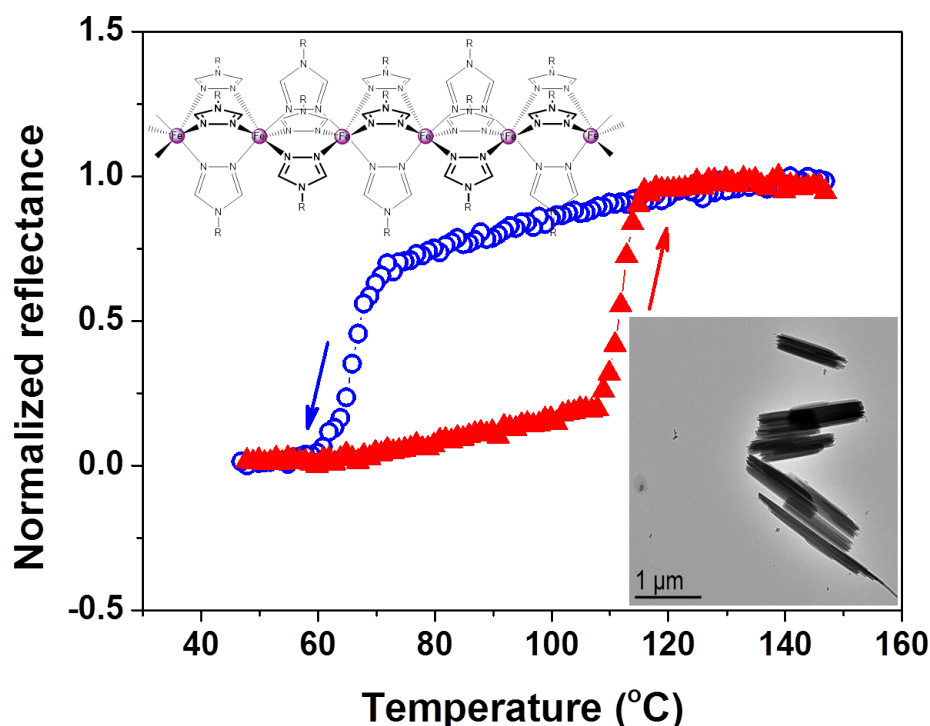
Figure 3.20: Temperature dependence of the normalized optical reflectance recorded at 550 nm in the heating and cooling modes for $[Fe(Htrz)_2(trz)](BF_4)$ microparticles. The insets show the TEM image of the particles (bottom) and the schematic representation of the chemical structure (top).

Figure 3.21a shows the temperature dependence of the current flowing in the device under a 40 kV/cm electric field. The overall current vs temperature (I-T) characteristics of the device were found basically the same as the previous ones. Upon heating the device from 30 to 130 ^{o}C (red symbols) a strong thermal activation of the current was observed up to 111 ^{o}C, where a sharp current decrease from 0.45 nA to 1.8 pA, characteristic of the LS to HS transition, was registered. When cooling the device (blue symbols), the latter remains in the HS state until 71 ^{o}C where the current increases slightly from 2.3 pA to 35 pA closing the hysteresis loop (characteristic to the HS to LS transition). The thermal cycle was recorded several times to ensure the reliability of the device. While the current intensity showed some evolution the transition temperatures were found well

reproducible in all registered curves, before, between and after the switches were performed (see Figure 3.22). The cycle measured between electrical switches was recorded with a 10 kV/cm electric field, which is sufficient to reveal the SCO phenomena. This aspect will be exploited later. It may be worth to note also that the optical reflectivity signal from the device cannot be used to detect the SCO (for its very weak change), hence only electrical means were used to this aim.
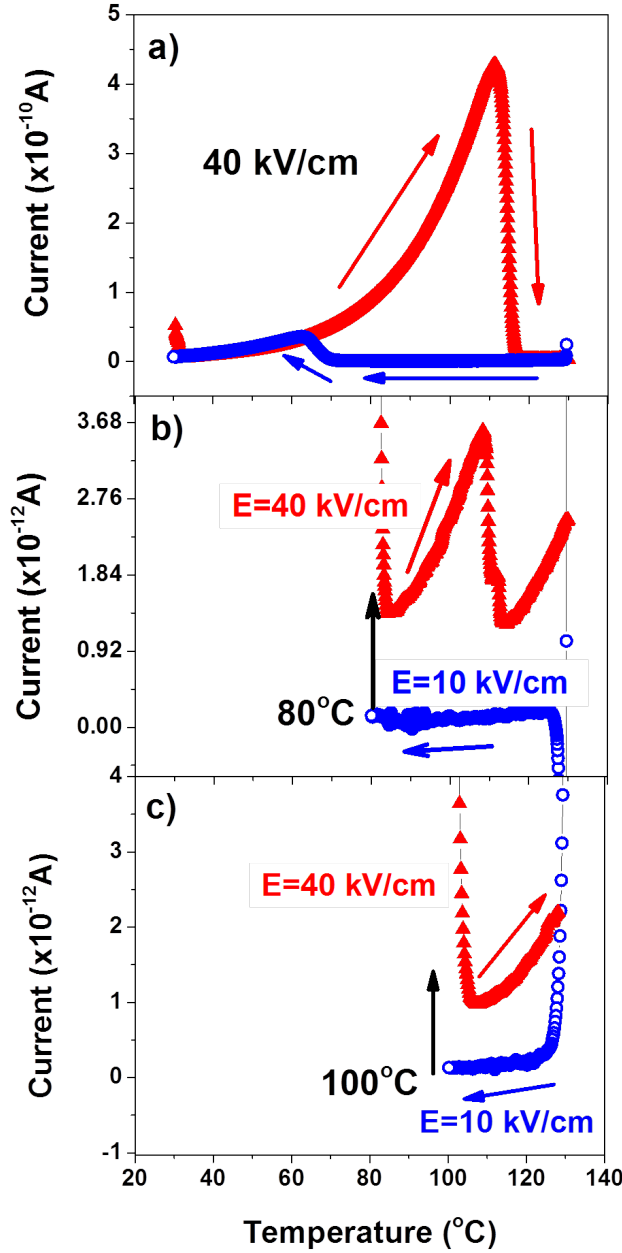
Figure 3.21: Current vs temperature characteristics of the interdigitated electrode device connected with particles of $[Fe(Htrz)_2(trz)](BF_4)$. Heating and cooling rates are 5 $^oC/min$. a) Full heating-cooling cycle between 30 and 130 ^oC under 40 kV/cm electric field. b-c) Incomplete thermal cycles: cooling from 130 to 80 ^oC (b) or to 100 ^oC (c) under 10 kV/cm bias followed by heating back to 130 ^oC under an electric field of 40 kV/cm.
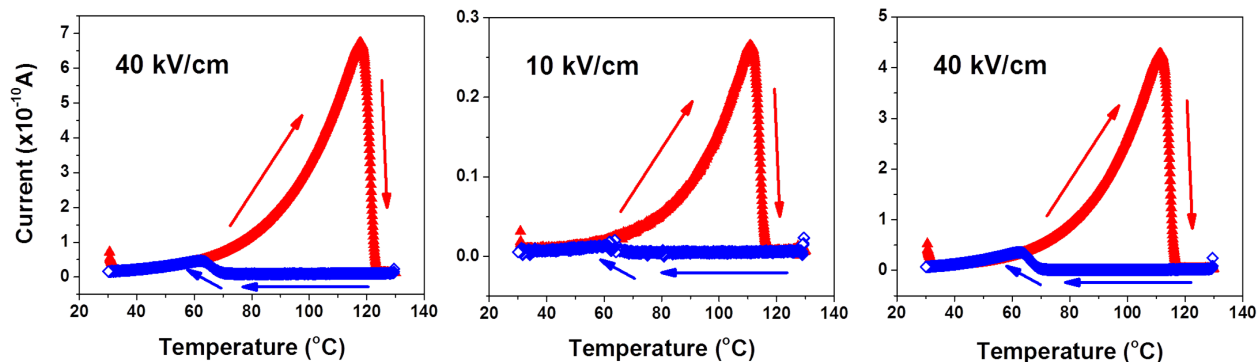
Figure 3.22: I - T cycles of the device before, between and after the electrical switches.

In order to explore the possibility of spin-state switching by an applied electrical field the thermal cycling has been stopped at different temperatures within the hysteresis loop and applied isothermally a voltage bias. In the heating mode no significant effect can be observed, i.e. the LS to HS transition could not be induced by the electric field. This fact will be treated further in the article. On the contrary, a clear response to the applied electric field was systematically observed in the cooling mode near the low temperature transition. Figure 3.21b shows a typical result. First the device was heated to 130 $^o C$ (without any applied bias) to ensure that the material is fully transformed to the HS state. Then the temperature was decreased to 80 $^o C$ while recording the current with a 10 kV/cm electric field (blue symbols in Figure 3.21b). An electric field of 10 kV/cm was applied to record the current of the device during cooling in order to be sure that the sample does not start to change its spin-state before the desired temperature. Indeed, inside the hysteresis loop, even just a few $^o C$ above the onset of the HS to LS transition, the system remains in the HS state "infinitely" (see Figure 3.23).
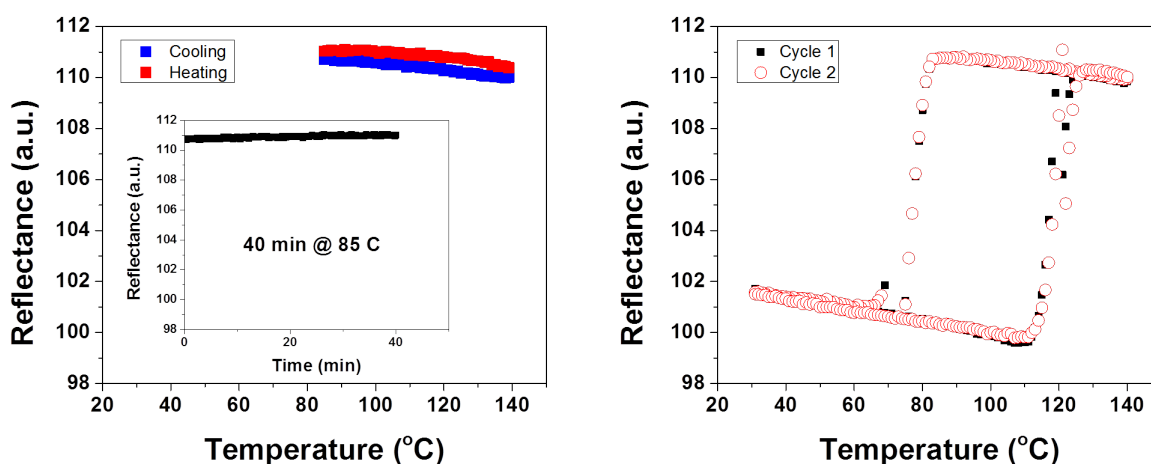
Figure 3.23: Reflectance variation in the cooling and heating modes between 140 $^o C$ and 85 $^o C$ in the HS state in the absence of any applied electrical field. The inset represents the variation of the optical reflectance as a function of time in isothermal conditions. No sign of the HS to LS spin transition can be inferred from these data. Two consecutive hysteresis loops are presented in the second panel (transition temperature are slightly shifted due to the fact that these measurements were performed on another synthesis batch).

When the temperature was stabilized an electric field step (from 10 to 40 kV/cm) was applied and the device was heated while measuring the current under a 40 kV/cm electric field. By increasing the temperature a decrease in the current around 110 ^oC was recorded, which is consistent with the LS to HS transition (red symbols in Figure 3.21b). This fact confirms a successful transformation of a part of the compound from the HS to LS state using the electric field at 80 ^oC. This effect cannot be attributed to any thermal phenomena induced by the application of the bias voltage since the low temperature (LS) state is clearly stabilized, therefore a clear correlation can be made with the application of the electric field. It has been also confirmed that the measured effect is not due to a minor cycle (see Figure 3.23). This experiment has been performed at different temperatures inside the bistability region (74, 76 and 80 ^oC) and with different values of the applied electric field (10, 20 and 40 kV/cm) and the same effect has been observed (see Figures 3.24 and 3.25).
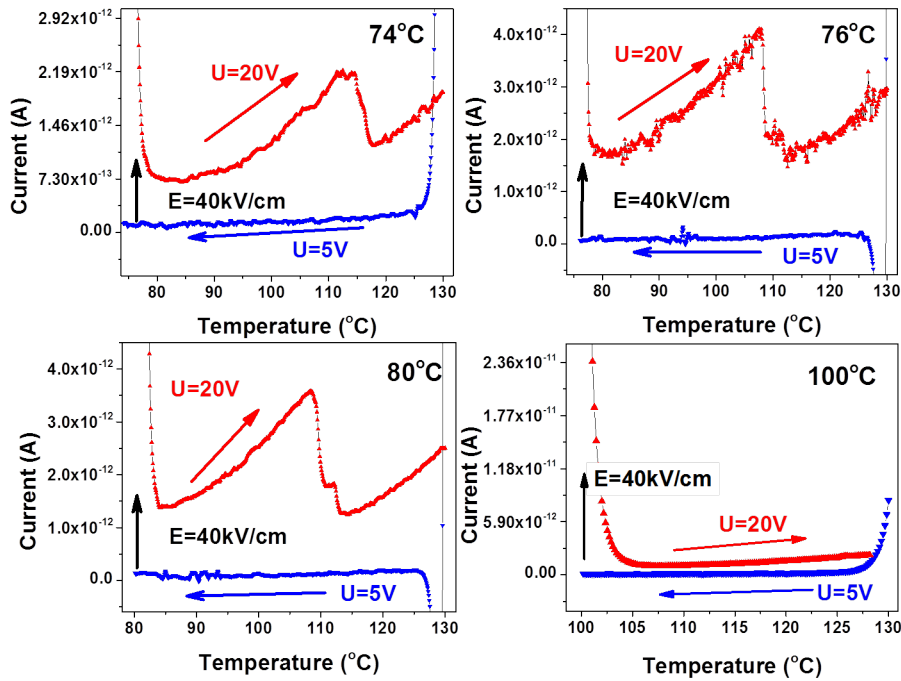
Figure 3.24: Electric-field (40 kV/cm) induced HS-LS switches at different temperatures.
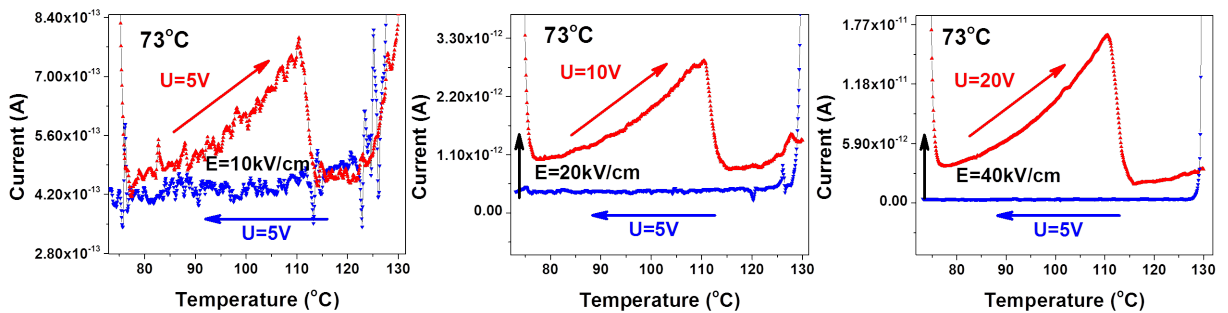
Figure 3.25: Electric-field induced HS-LS transition performed at 73 ^oC with different electric field strengths.

On the other hand, when the same experiment was performed at 100 ^oC inside the

hysteresis loop (cooling mode) the switch could no longer be obtained and the device remained in the fully HS state (Figure 3.21c). It may be worth to note here that at 100 ^oC the HS state is the stable phase in contrast to the 74-80 ^oC range wherein it is only blocked in a metastable phase by the nucleation barriers. It is worth stressing that in all these experiments the maximum current intensity obtained after the switch is several orders of magnitude lower (5% at best) than that observed for the "reference" thermal cycle (i.e. for the full transition). Unfortunately, if the applied field exceeds 40 kV/cm the electrodes are damaged and a further increase of the field to test for a higher spin conversion efficiency has not been possible. The relationship between the current intensity and the HS/LS fractions is certainly not linear, nevertheless it is a clear indication that the electric field-induced spin-state switching observed in these experiments is very incomplete. It is possible, however, that this result would be different if the scale of this device would be a few nanometers. Indeed, very small nanoparticles of **1** have been reported to preserve their hysteresis properties and even exhibit an electric field-induced switching phenomenon [35].

It is important to note that these experiments have been performed on several devices and consistent results have been obtained. Figure 3.26 shows an electric switch experiment carried out on a different device at 82 ^oC. (See figure S5 in the SI for the device characteristics.) In this experiment, following the cool down to 82 ^oC under 5 V bias, the device was kept at this temperature for about 4 hours under 40 kV/cm electric field. The measured current continued to increase with time, which indicates that the instantaneous field-induced switching effect is followed by a slow, continuous process of HS to LS switching. To prove that the transition indeed occurred, the temperature was increased from 82 to 130 ^oC and the current in the device was measured under a 40 kV/cm electric field. One can clearly observed the characteristic decrease in current caused by the LS to HS spin transition around 120 ^oC.
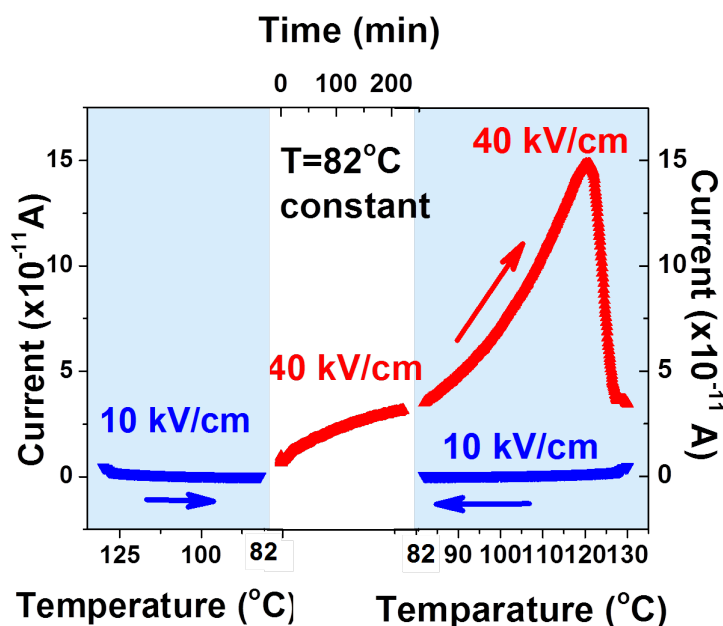
Figure 3.26: Electric field switch experiment performed at 82 ^oC. The left panel shows the current recorded when cooling the device from 130 to 82 ^oC under 10 kV/cm. The middle panel depicts the temporal evolution of the current at fixed temperature (82 ^oC) and bias (40 kV/cm) followed by a complete thermal cycle (right panel) between 82 and 130 ^oC.

In order to reproduce at least qualitatively the effects of an electric field on the quasi-static thermodynamical and kinetic properties of SCO materials, a simple theoretical approach based on statistical physics considerations was developed in a very similar way as in references [141] and [40]. The interaction energy between the macroscopic field $\vec{E}$ and the electric dipolar moment $\vec{p}$ of SCO complexes is added to both the static and dynamical versions of the mean field Ising-like model (see equations 3.1 and 3.2 for the static case).

$$H = -J \sum_{<i,j>} \sigma_i \sigma_j + \left[\frac{\Delta}{2} - k_B T ln \left(\frac{g_{HS}}{g_{LS}} \right) \right] \sum_{i=1}^{N} + H_{elec} \qquad (3.1)$$

$$\langle H_{elec} \rangle (\{\sigma\}) = -\frac{p_{HS}^2 - p_{LS}^2}{6k_B T} E^2 \sum_{i=1}^{N} \sigma_i \qquad (3.2)$$

where k_B is the Boltzmann constant, Δ (2450 K) stands for the ligand field, J (525 K) is a phenomenological parameter describing cooperativity, g_{HS}/g_{LS} (750) is the effective degeneracy ratio of the two states H_{elec} is the mean value of the static electric field and σ is a fictitious spin with eigenvalues +1 or -1 for the HS and LS states, respectively. The electric field - dipole interaction modifies the ligand field of SCO molecules due to the spin-state dependence of the dipolar momentum. This leads to a shift of the transition temperature whose analytical expression can be obtained using the Langevin approach in the high temperature limit (equation 3.3) [40].

$$T_{eq}(E) = T_{eq}(E = 0) - \frac{p_{HS}^2 - p_{LS}^2}{6k_B T} E^2 \qquad (3.3)$$

The electric dipolar moment of the two spin states $p_\alpha = 3\epsilon_0 \left(\epsilon_\alpha^r - 1 \right) k_B T / N_A$ ($\alpha =$ HS, LS, ϵ_0 represents the vacuum permittivity and N_A is the number of molecules), can be roughly estimated from typical values of the relative permittivities $\epsilon_{HS}^r = 1$ and $\epsilon_{LS}^r = 5$ of the two spin states [142]. As shown in Figure 3.27a, with these parameters the application of an electric field of $E = 40$ kV/cm leads to an increase of the transition temperature by ca. $\Delta T = 10.7$ K. In other words the field stabilizes the LS phase in agreement with the experimental results. This explains why the switch is unidirectional. This very simple model, however, cannot provide a quantitative analysis, mainly due to the kinetic aspects associated with the nucleation-growth phenomena in these particles. This facet of the spin transition under an electric field is clearly highlighted by the dynamical Ising-like model. Figure 3.27b shows that starting from a HS phase, the application of the electric field within the hysteresis loop leads only to a slight decrease of the HS fraction (8.5%, from 0.9 to 0.825) corresponding to a partial conversion of the material into the LS state. This result is a direct consequence of the important energy barriers between the two states within the hysteresis region.
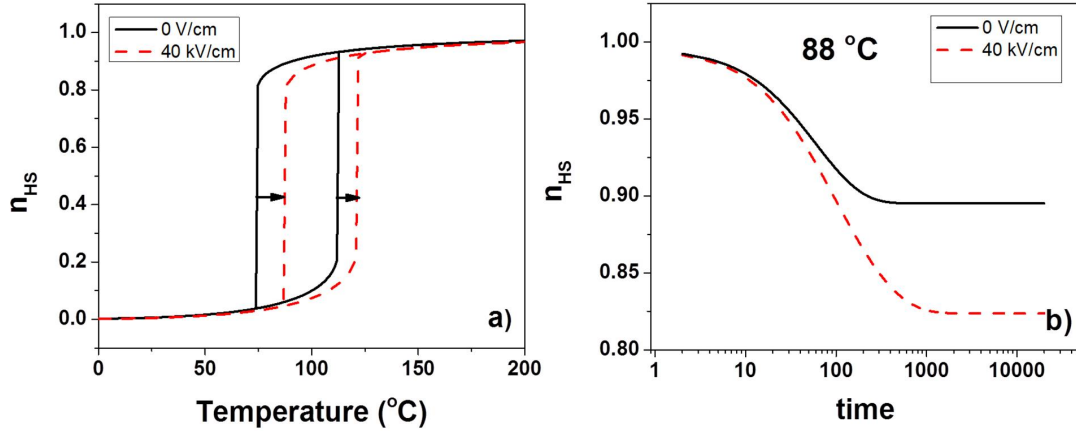
Figure 3.27: (a) Simulated temperature dependence of the HS fraction in the absence and presence of an electric field. The field-induced shift of the spin transition is indicated by the arrow. (b) Logarithmic representation of the simulated temporal evolution of the HS fraction in the presence and absence of an applied electric field (40 kV/cm) at 88 ^oC (cooling branch). At 88 ^oC the stable phase is n_{HS} = 0.9 at 0 kV/cm due to a thermal relaxation.

3.3 Conclusions

In this chapter we described the fabrication process and characterization of SCO based microelectronic devices obtained by performing dielectrophoresis on micrometric particles of the $[Fe(Htrz)_2(trz)](BF_4)$ complex. We first determined the optimum parameters for organizing the particles between the interdigitated electrodes, which allowed us to obtain a dense and fairly uniform coverage of the interelectrode gaps by the particles. In agreement with previous results, in each device we observed a thermal hysteresis of the current intensity under applied bias, which we could clearly correlate with the spin transition. In agreement with the measurements on the bulk samples (see Chapter 2) the current flowing in the device is significantly higher in the low spin state of the complex. Then we performed an analysis of the stability of the spin transition for both the starting material and the device. It was shown that the particles keep their spin transition properties even after 3000 thermal switching cycles in ambient air, but the cooling branch of the hysteresis associated with the SCO shifts slowly to higher temperature. At the device level the spin transition appears also robust, but the current intensity decreases continuously upon thermal cycling, which we tentatively attributed to a deterioration of the particle/particle and/or particle/electrode contacts. Further studies will be necessary to overcome this problem and obtain more robust devices. A possible approach would be the encapsulation of the device.

We have also investigated the effect of light irradiation on these devices. By fixing the temperature inside the hysteresis loop in the low spin state, a reversible decrease in the current intensity as well as a slow irreversible increase of the current was observed under light irradiation. In the high spin state no effect could be detected in otherwise identical conditions (bias, temperature, light irradiation). These photoeffects seem to be related to the mobility of the charge carriers, which increases with increasing temperature and which is significantly higher in the low spin state of the material when compared to the high spin state. The observed light-induced phenomena are also related to some extent to the sample environment as the effects are more pronounced in the presence of oxygen and humidity.

Moreover no correlation could be made with the absorption spectrum of the spin crossover compound. These two latter observations point to a possible adsorbate mediated redox mechanism behind the photoeffects. While the underlying mechanism needs further investigations, it is clear that this possibility of turning on and off the photoeffect by switching the spin state of the system (within the hysteresis loop) is a new and promising property of spin crossover devices, which broadens the scope of their future applications.

In the last part of this chapter, the electric field induced switching of the spin state of the $[Fe(Htrz)_2(trz)](BF_4)$ complex at the macroscopic scale is demonstrated. The unidirectional switching from the metastable HS to the stable LS state has been achieved by applying an electric field step inside the hysteresis loop. The field effects were discussed in the frame of the well-known static and dynamic Ising-like models. This approach allowed to reproduce qualitatively the main features of the experimental observations: stabilization of the LS state, slow and incomplete switching within the hysteresis due to the kinetic barriers.

Chapter 4

Elaboration and characterization of nanoelectronic devices in vertical configuration

This chapter describes an alternative approach for charge transport measurements in the tunneling regime based on robust, well-reproducible large-area vertical devices with thin SCO spacer layers. This approach allowed us to probe the spin-state switching in the SCO layer by optical means while detecting the associated resistance changes both in the tunneling (thin junction) and injection-limited (thick junction) regimes. The high current intensity in the devices provided also possibility for mechanistic studies by means of temperature- and frequency-dependent dielectric spectroscopy.

Obviously, the main bottleneck to this approach is the need for high quality, ultrathin, pinhole-free SCO films over large electrode areas, which resist also to the deposition of the upper metallic electrode. To this aim the [$Fe(bpz)_2(phen)$] SCO complex **1** has been chosen (bpz = dihydrobis(pyrazolyl)borate and phen = 1,10-phenantroline), which is one of the scarce SCO compounds that can be deposited by thermal evaporation [59, 93, 143]. The bulk powder of **1** displays a rather abrupt spin transition, with a very narrow hysteresis, while the vacuum-deposited films exhibit a gradual spin crossover. Both the powder and film samples are known to exhibit also light-induced excited spin-state trapping (LIESST) phenomenon below ca. 50 K. Interestingly, the spin crossover properties of the films are virtually independent of the film thickness from (at least) 1 μm down to the sub-monolayer (i.e. isolated molecule) level, which makes this material ideal for nanoelectronic devices. The fabricated devices have been studied in variable temperature DC and AC regimes as well as isothermally at 5 K, while attempting to observe the LIESST effect in electrical properties.

4.1   Sample and device characterization

Before investigating the devices, a thorough sample characterization was done starting from the powdered sample, the deposited thin film as well as the material stacked between the deposited electrodes.

The synthesis of the powdered sample was carried out under argon atmosphere $Fe(BF_4)_2 \cdot 6H_2O$ (0.9079 g, 2.7 mmol) was added to a potassium bis(1-pyrazolyl)borohydrate (1.0000 g, 5.4 mmol) in methanol (25 ml) with ascorbic acid (10 mg) and stirred for 1 h. The resulting KBF_4 salt was filtered and washed with methanol (5 ml). 1,10-phenanthroline (0.5355

g, 2.7 mmol) was added in small portion under agitation to the filtrate forming a dark violet precipitate. The violet microcrystalline powder was filtered after 1 h, washed twice using methanol (10 cm^3) and dried under vacuum overnight. I.R: ν(C=C) 1624, 1591, 1513; ν (C=N) 1159. Elemental analysis: calculated for $C_{24}H_{24}N_{10}B_2Fe$: C, 54.39; H, 4.56; N, 26.43 gives C, 53.82; H, 4.30; N, 26.18.

Variable-temperature magnetic susceptibility data was obtained at cooling and heating rates of 4 K/min under a field of 0.1 T using a Quantum Design MPMS superconducting quantum interference device magnetometer. The experimental data was corrected for the diamagnetic contribution using Pascal's constants. Optical reflectivity images were acquired with a MOTIC SMZ-168 stereomicroscope equipped with MOTICAM 1000 color CMOS camera. A 2 K/min rate was used for both cooling and heating. Figure 4.1 shows the temperature dependence of the magnetic susceptibility and the optical reflectance of the [$Fe(bpz)_2(phen)$] complex in powder form. Both measurements reveal a clear and abrupt transition centered around 165 K, without any obvious hysteresis loop.
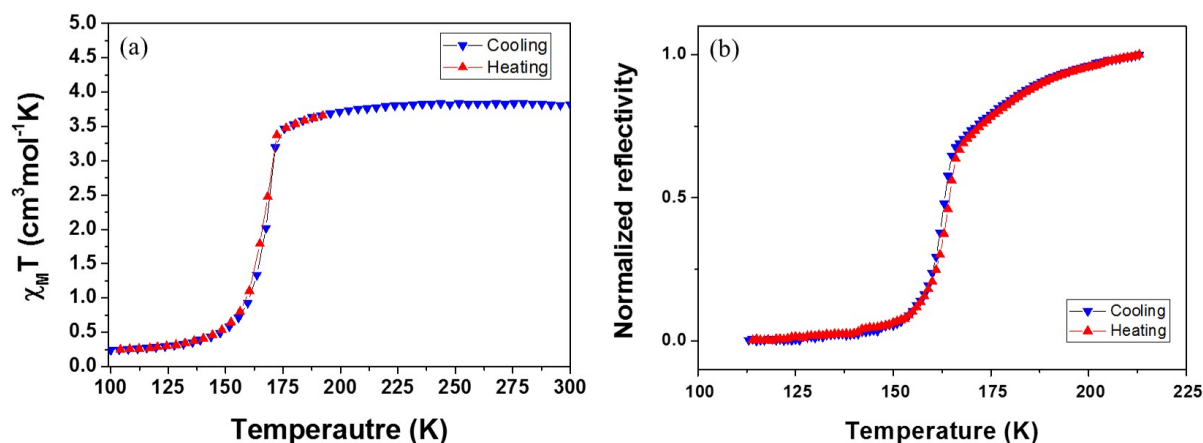
Figure 4.1: Variable-temperature (a) magnetic susceptibility and (b) optical reflectivity of [$Fe(bpz)_2(phen)$] powder.

The spin transition of the [$Fe(bpz)_2(phen)$] complex in powder form has been detected by measurements of the dielectric constant by using a variable temperature Novocontrol BDS 4000 broad-band dielectric spectrometer. The powder sample was sandwiched between two electrodes with a thickness of ca. 100 μm and an effective diameter of 10 mm. The temperature was varied between 110 K and 220 K, and the temperature variation of the real part of the dielectric permittivity ϵ' in quasi-static mode at 0.1 Hz and in dynamic mode at 1 MHz shows the abrupt spin transition at 167 K, where a typical [24] increase of ca. 1% is registered when the system transits from LS to HS (Figure 4.2).
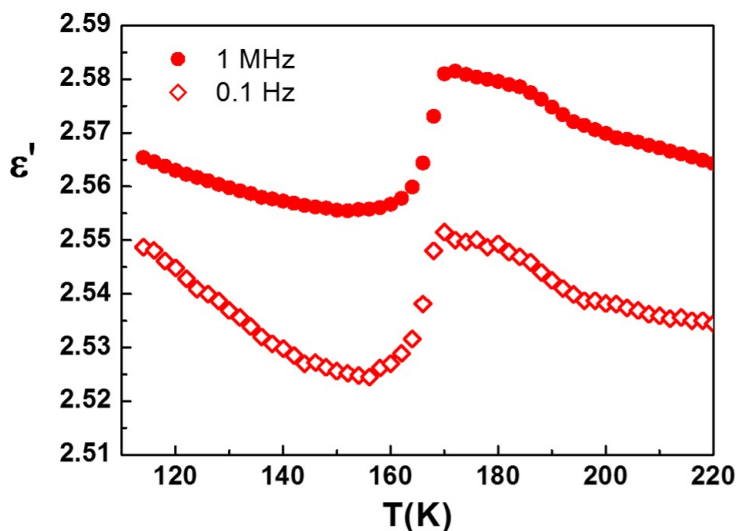
Figure 4.2: Variable-temperature dielectric permittivity (real part) of the [*Fe*(*bpz*)$_2$(*phen*)] powder at two different frequencies of the applied field.

Thermogravimetric analysis (Figure 4.3) shows a stable behavior of the complex in the temperature range of 25 ^oC and 200 ^oC with no indication of solvent loss or sample degradation. Starting from 210 ^oC the sample presents an abrupt weight loss, indicating that the onset of sublimation.
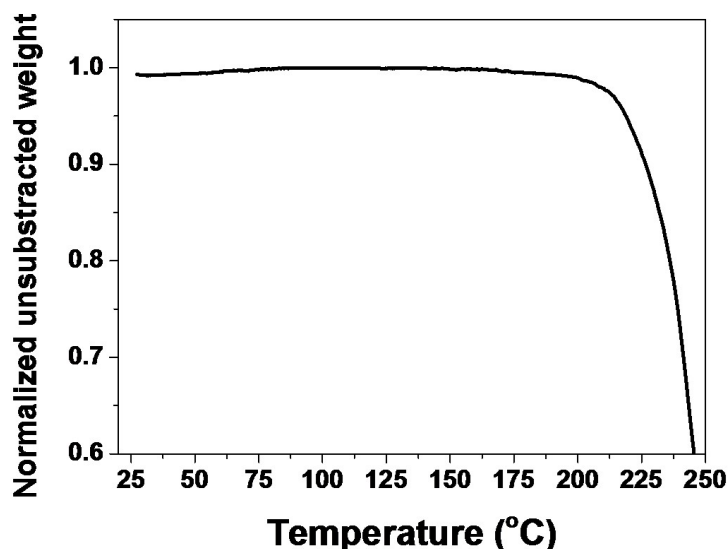
Figure 4.3: Thermogravimetric analysis on [*Fe*(*bpz*)$_2$(*phen*)] powder.

The volume change caused by the spin transition in a single crystal has been also studied using variable temperature single-crystal X-ray diffraction. By plotting the cell parameters as a function of temperature (see Figure 4.4), two distinct regions can be clearly observed. The first region between 80 K and 150 K has an average unit cell volume of 590 $Å^3$, while the second region situated between 170 K and 290 K has an average unit volume of 650 $Å^3$. The resulting change in volume is about 8.5 % and corresponds to the volume change upon SCO. This value is typical for Fe(II) SCO complexes. Incidentally it

is interesting to note also the lack of any significant thermal expansion in this compound
which is a rather scarce behavior.
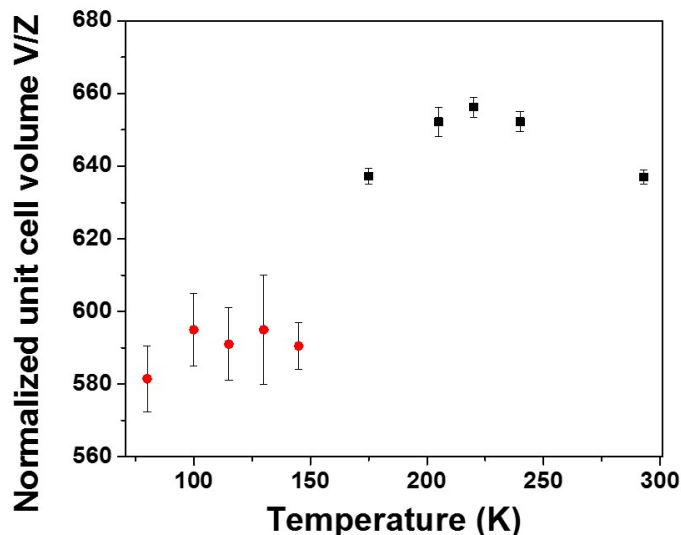
Figure 4.4: Cell volume as a function of temperature for a single crystal of
$[Fe(bpz)_2(phen)]$.

In order to obtain thin films similar as described in ref [93, 143], the SCO complex
was placed in a crucible and heated by Joule effect up to 110 ^oC allowing the sublimation
of the complex on the chosen substrate under ultra-high vacuum (10^{-7} Torr) conditions.
AFM topography measurements have been performed at room temperature in air using a
Dimension Icon instrument (Bruker) on a 10 nm test deposition on an area of 20x20 μm^2
and no imperfections were observed in several regions that were investigated. Also the
obtained a topography presented a roughness for the sampled area of 0.173 nm, which
indicates that the complex forms an remarkably smooth thin film.
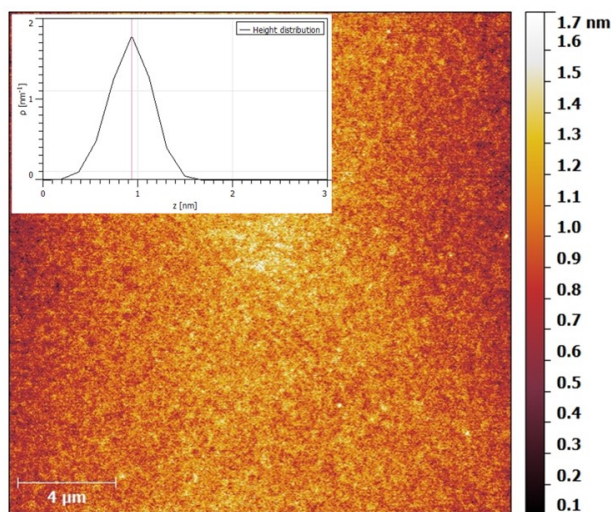
Figure 4.5: AFM topography of an area of 20x20 μm^2 of the deposited thin film of
$[Fe(bpz)_2(phen)]$. The inset represents the height distribution of the measured area.

UV-visible absorption measurements on the films were carried out using a Cary-50 (Varian) spectrometrer. Different thicknesses of the thin films of the complex sublimated on glass substrates were placed in a vertical cryogenic cell (Linkam). Absorption spectra were recorded between 93 K and 293 K in the 200 - 800 nm spectral range. Figure 4.6 presents the UV-Vis spectra for a 110 nm (top panel) and a 60 nm (bottom panel) thin film. The 110 nm film presents three distinct peaks at 503 nm, 550 nm and 604 nm respectively, which are characteristic to the material [143]. The 60 nm thin film presents the same characteristic peaks, however the 550 nm peak is less pronounced. The temperature dependence of the absorbance of the thin films is also plotted at a fixed wavelength, and it reveals the well-known very gradual spin crossover between approx. 100 - 200 K for both the 110 nm and 60 nm films. As mentioned before, the difference between the SCO behavior of the film and the powder could be due to the different structure of the two samples, i.e. this being an amorphous thin film and not a crystalline powder. However, the most important aspect is that the sample still presents the SCO phenomenon and did not degrade during sublimation.
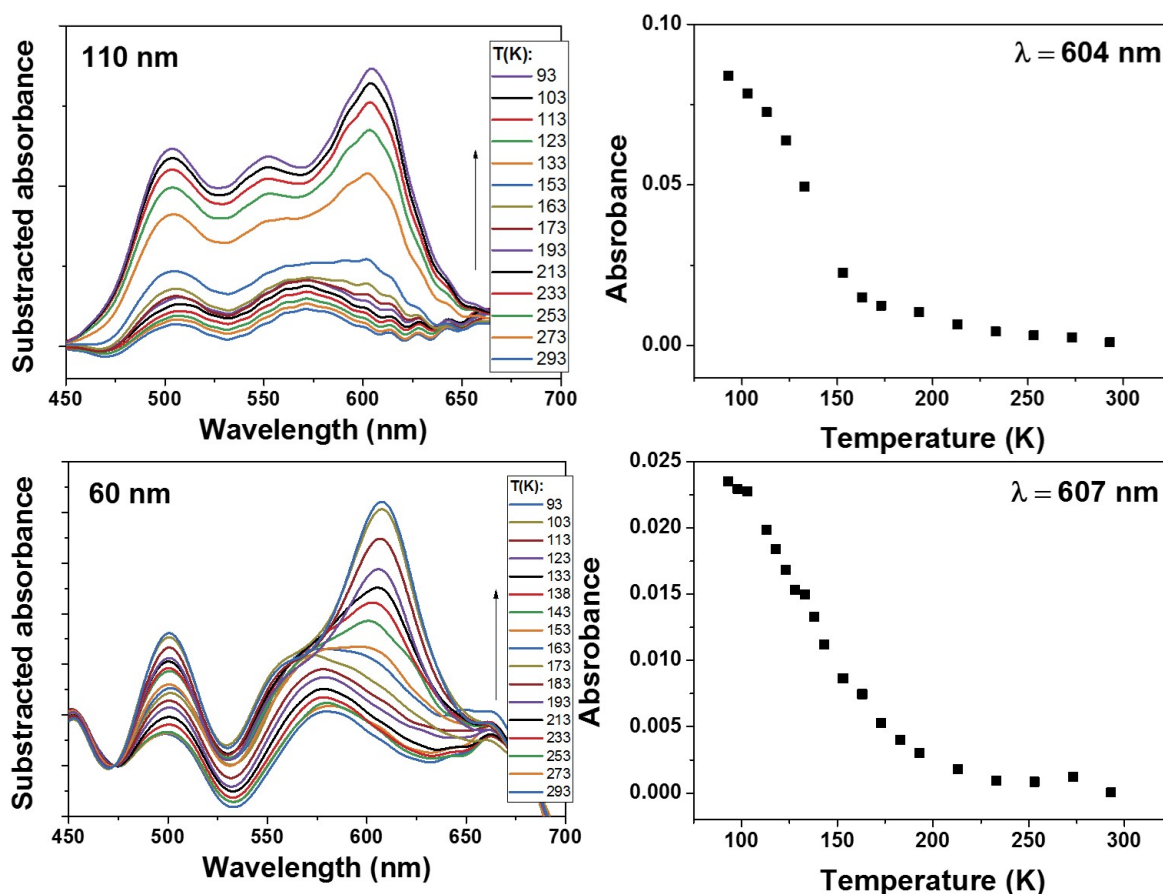
Figure 4.6: Top panel presents the UV-Vis spectra of the 110 nm thin film recorded at different temperatures and the corresponding temperature dependence of the absorbance at λ = 604 nm. Bottom panel presents the UV-Vis spectra of the 60 nm thin film recorded at different temperatures and the corresponding temperature dependence of the absorbance at λ = 607 nm.

The complex exhibits thus spin crossover after being sublimated on a glass substrate, but the question is weather this SCO is maintained also when a metallic electrode is evaporated on top of it. Since the spin transition in **1** is accompanied by a significant change in

volume (ca. 8.5 %) the mechanical stress imposed by the 'sandwich' geometry may change or even preclude the SCO in the device. To verify the occurrence of SCO in these circumstances we acquired optical reflectivity spectra of a glass/ITO/SCO(100 nm)/Al stack as a function of temperature between 300 K and 5 K. This method probes the change in the complex refractive index ($n^* = n+ik$) associated with the spin transition [144]. As shown in Figure 4.7b the reflectance ($\lambda = 640$ nm) of the multilayer decreases significantly between ca. 200 and 100 K and increases again to the initial level below 50 K.
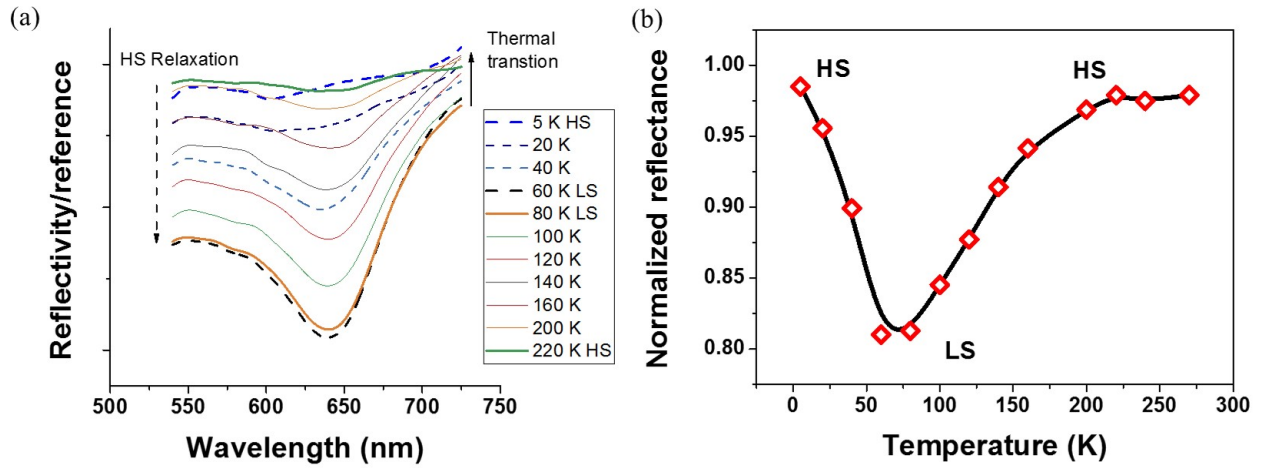
Figure 4.7: (a) Variable temperature reflectivity spectra for a glass/SCO/Al stack. (b) Temperature dependence of the optical reflectivity (λ =640 nm).
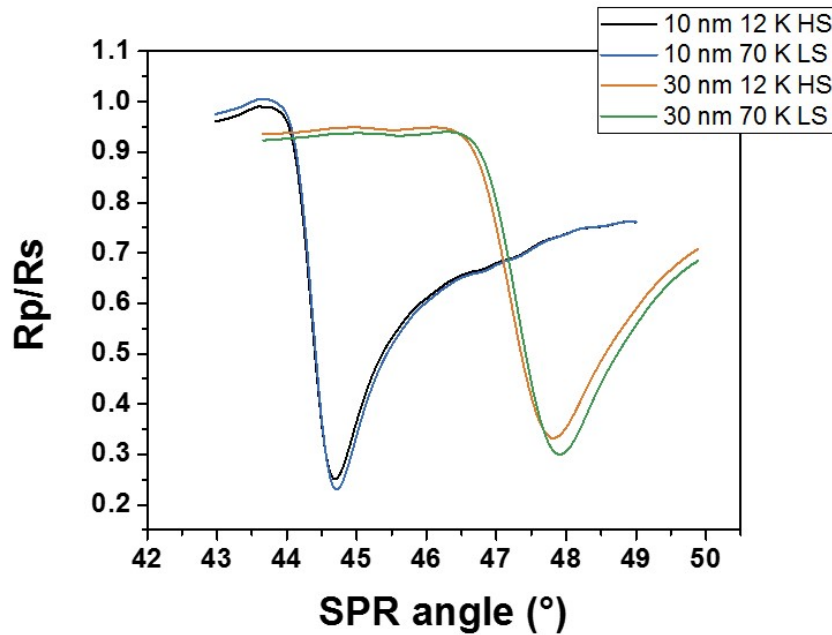
Figure 4.8: SPR spectra recorded for the 10 nm and 30 nm junction in the LS and HS state.

These changes of the reflectivity signal correspond closely to the well-known thermal spin transition and the LIESST effect of the film of **1** [59, 91, 143, 145], providing thus unambiguous evidence that the SCO properties are preserved in the sandwich structure.

The photo-induced $LS \leftrightarrow HS$ SCO phenomenon was also detected in very thin (10 nm and 30 nm) films through the refractive index changes, but due to the smaller thickness the measurement was carried out by depositing the films on a surface plasmon resonance sensor [146]. The SPR spectra was registered for the two thickness at 12 K (HS state) and 70 K (LS state) (see Figure 4.8), and for the 10 nm film an angle variation of 0.020^o was measured, while for the 30 nm film, an angle variation of 0.098^o was detected. The higher SPR angles in the LS states are consistent with the higher density of the material in this spin state (see Figure 4.4).

4.2 Fabrication and characterization of nanoelectronic devices

Nanoelectronic devices (10 nm, 30 nm and 100 nm) were by grown by thermal evaporation at 110 ^oC in a high vacuum chamber (10^{-7} Torr) at a rate of 0.05 nm/s on 180 nm thick ITO (indium-tin-oxide) electrodes. These latter were purchased from Praezisions Glas & Optik GmbH and patterned by wet etching using a conventional photolithography mask. Alternatively, for a 100 nm junction the surface of the ITO electrode surface was planarized by spin-coating a PEDOT:PSS (poly(3,4-ethylenedioxythiophene) polystyrene sulfonate) hole transport layer on top of it. The upper 100 nm thick Al electrode was finally thermally evaporated through a shadow mask on the substrate. To avoid perforation of the SCO layer the Al film was deposited at a rate of 0.1 nm/s and the substrate was cooled by water. The schematic representation of the device made with **1** is shown in Figure 4.9a. Thin films of 4.9 were first grown by thermal evaporation on pre-patterned ITO bottom electrodes on glass substrates. The choice of the substrate and the electrode was motivated by their optical transparency, which allows for both triggering and probing the spin-state changes in the devices by visible light irradiation. In the next step the upper Al electrodes were carefully deposited by thermal evaporation through a shadow mask into a crossbar configuration (Figure 4.9b). The effective junction area of each device is $\approx$ 3 mm^2. Junctions of **1** were fabricated in a single run with three different thicknesses (10, 30 and 100 nm). The film thickness was monitored in-situ during the deposition by a quartz crystal balance and confirmed also ex-situ by acquiring atomic force microscopy (AFM) data and scanning probe microscopy (SEM) images of the device tranches milled by focused ion beam (FIB) etching (Figure 4.10).
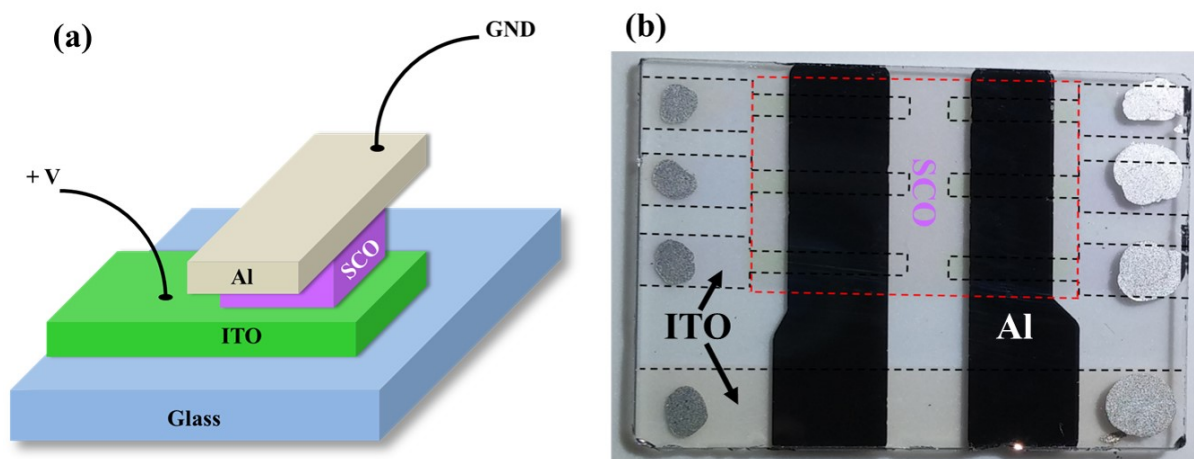
Figure 4.9: Device structure. a) Schematic representation of the ITO/SCO/Al junction. b) Photograph of a device with six crossbar junctions. The regions with ITO and SCO films are indicated by dashed lines. Silver paste contacts on the ITO are also visible.
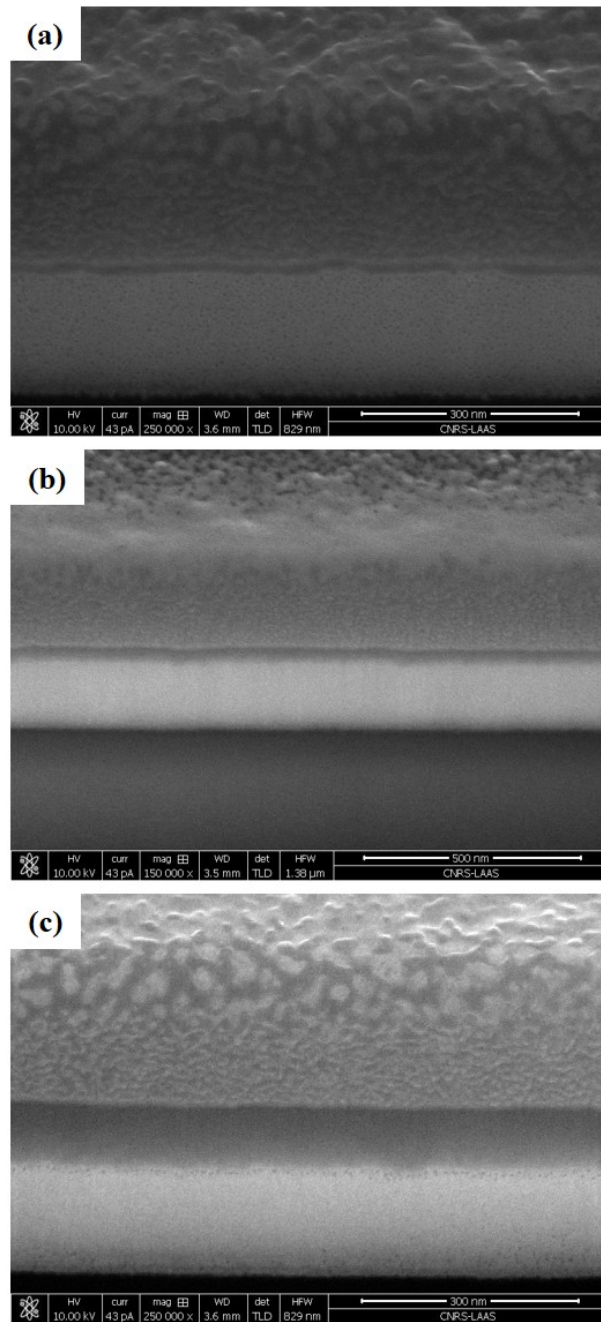
Figure 4.10: SEM images of the FIB milled cross-section of the junctions with different
SCO film thickness: (a) 10 nm, (b) 30 nm and (c) 100 nm).

Electrical characterization of the nanoelectronic devices were performed in a Oxford cryogenic cell adapted for electrical measurements. The wires where connected to the devices using silver paste pads. A sub-femtoamp remote source-meter (Keithley 6430) was used to apply the bias and to measure the current in the device.

I-V characteristics of the different devices were strongly non-linear and exhibited either temperature independent tunneling or insulating-like thermal behavior, which rules out the contribution of short circuit channels. These observations together with the highly reproducible device characteristics (for devices with the same geometry) confirm the high quality of the SCO films in the devices.

Variable temperature current-voltage curves registered for devices with 10 nm SCO layer (Figure 4.11a) are clearly characteristic of tunnel junctions. In particular, the thermal variation of the I-V curves is negligible in a broad temperature range (5 K - 293 K), which is a generic feature of tunneling conduction. By plotting the I-V data as a Fowler-Nordheim (F-N) plot as $ln(I/V^2)$ vs. $1/V$ (see Figure 4.11) further insight into the charge transport process can be extracted. If the F-N plot presents a minimum at a certain voltage, the device suffers a transition between a low- and high-bias regime, characterized by the transition voltage V_{trans} which is related to the energy offset between the Fermi level of the electrode and the nearest molecular orbital. Indeed, as illustrated in Figure 4.12a-c, the F-N plots presents a minimum, which corresponds to a transition voltage of V_{trans}=2.5 V at 5 K and 100 K and V_{trans}=1.6 V at room temperature. Also the I-V curves obey Simmons' relationship $I = I_0(V + \gamma V^3)$ [147] (Figure 4.13a-c) and the differential conductance dI/dV curves exhibit parabolic shape typical of tunneling junctions as illustrated in Figure 4.13d-f.

A closer examination of the temperature dependence of the conductivity of the junction reveals a slight increase (ca. 10 %) in the thermal spin crossover range between ca. 200 and 100 K (Figure 4.11b). It is, however, difficult to conclude solely from these data on a link between the two phenomena. In order to separate thermal effects and the influence of SCO on the device characteristics we used light irradiation to alter the spin-state of the junction. We cooled the device to 5 K in dark and we irradiated the sample using a halogen lamp. Immediately the current flowing in te device dropped by nearly 9 % (Figure 4.11c). Following this first irradiation, the current intensity remained at the same level during several ON-OFF irradiation cycles. This finding can be correlated with the LIESST effect: light irradiation leads to the population of the HS state, which is metastable at 5 K with a long lifetime of several days. To further substantiate the relationship between the current intensity and the spin state of the device this latter was heated to 100 K in the dark. Upon heating the metastable HS state relaxes to the LS ground state and as a consequence the current reached the same level as before light irradiation. This 'dark cooling - photo-switching - dark heating' cycle was repeated several times with the same result. The device was also irradiated by light at 100 K where no LIEEST effect occurs, and in this case no significant effect on the conductivity was observed (Figure 4.11d). All these results point to the conclusion that switching the spin-state of the junction from the LS to the HS state leads to a well reproducible decrease of ca. 9 % of the tunneling current.
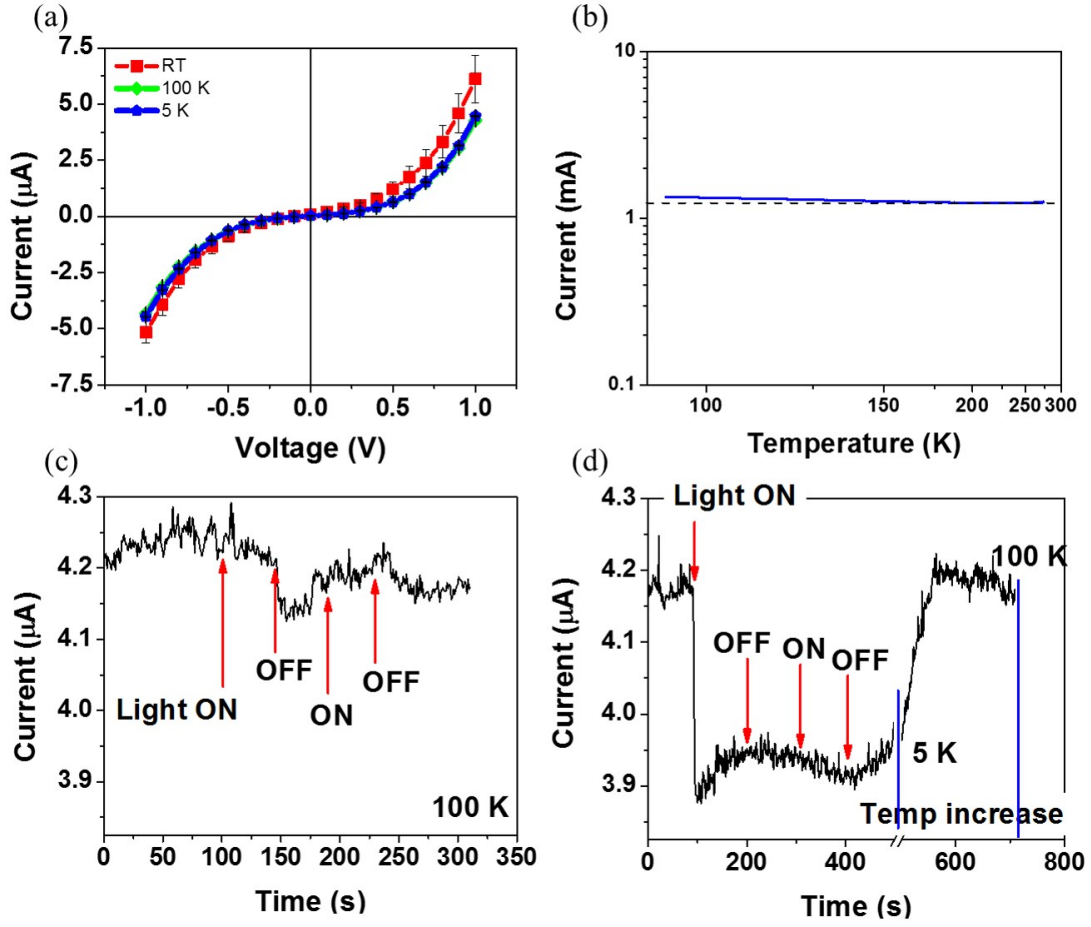
Figure 4.11: Electrical characteristics of a 10 nm junction. (a) I-V curves registered at room temperature, 100 K and 5 K. (b) Temperature dependence of the conductivity of the junction. (c) Visible light irradiation effect on the current flowing in the junction at 5 K followed by heating from 5 K to 100 K in the dark. (d) Visible light irradiation effect on the current flowing in the junction at 100 K.
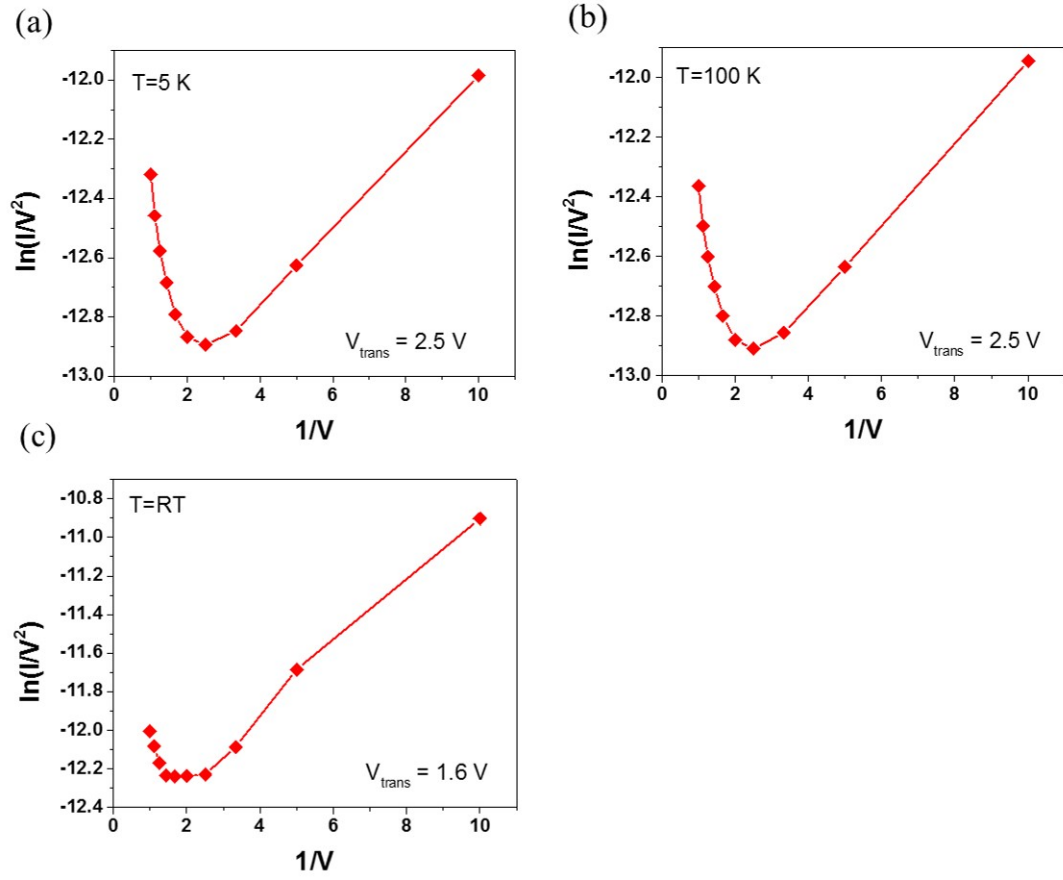
Figure 4.12: I-V data of the 10 nm device acquired at (a) room temperature, (b) 100 K and (c) 5 K plotted as $ln(I/V^2)$ vs. $1/V$ F-N plot. dI/dV vs. V curve.
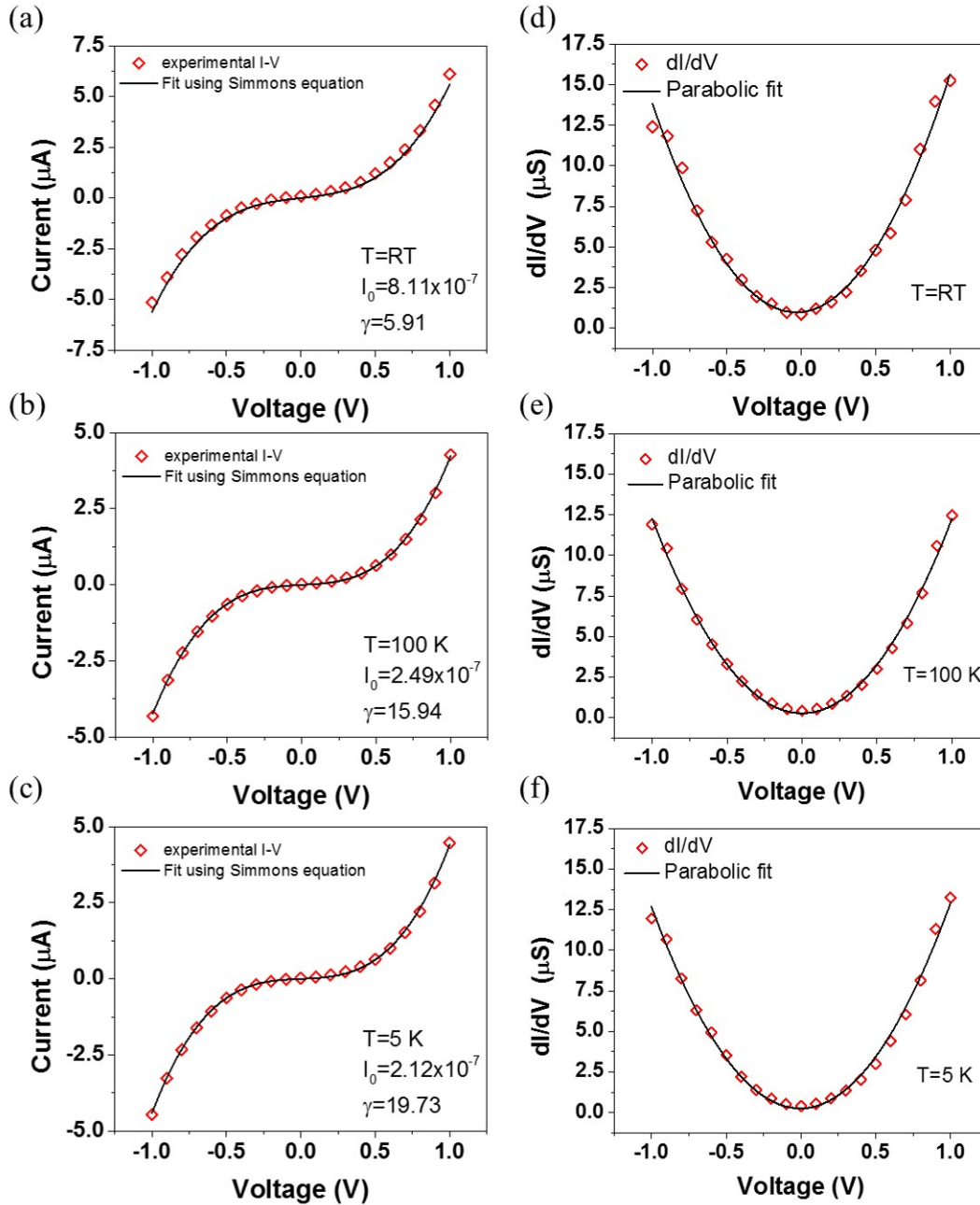
Figure 4.13: I-V data of the 10 nm device acquired at (a) room temperature, (b) 100 K and (c) 5 K. The straight lines correspond to fits of the data with Simmons' intermediate-voltage range tunneling equation (the barrier height is slightly lower than the applied voltage): $I = I_0(V + \gamma V^3)$. The fitted parameters are shown in the figures. dI/dV vs. V curve and parabolic fit for the device at (d) room temperature, (e) 100 K and (f) 5 K.

Figure 4.14a shows the current-voltage characteristics of the 30 nm device registered at room temperature and 5 K. The high temperature I-V characteristic changed considerably from the 10 nm device, presenting a rectifying behavior, with current flowing only under positive voltage, i.e. when the Al electrode is the cathode. The rectification ratio is rather high exceeding 420. The existence of an onset voltage is indicative of strong interface barriers, while the asymmetry of the I-V curves stems merely from the asymmetry of the device constructed with different electrode materials. The I-V curves have been fitted with

the diode equation [148, 149]:

$$I = I_0 \left[exp\left(\frac{eV}{nk_BT} \right) - 1 \right] \qquad (4.1)$$

where I_0 is the reverse bias current, k_B the Boltzmann constant, e the charge of electron and n the 'non-ideality' factor. While the fits are satisfactory down to ca. 100 K, the fitted values of n are rather high ($n = 12$ at 293 K) when compared to the commonly observed ones ($n = 1$-2). This deviation from the ideal behavior might be an indication of bulk conduction barriers, all the more that for thicker (100 nm) barriers n further increases ($n = 31$ at 293 K).
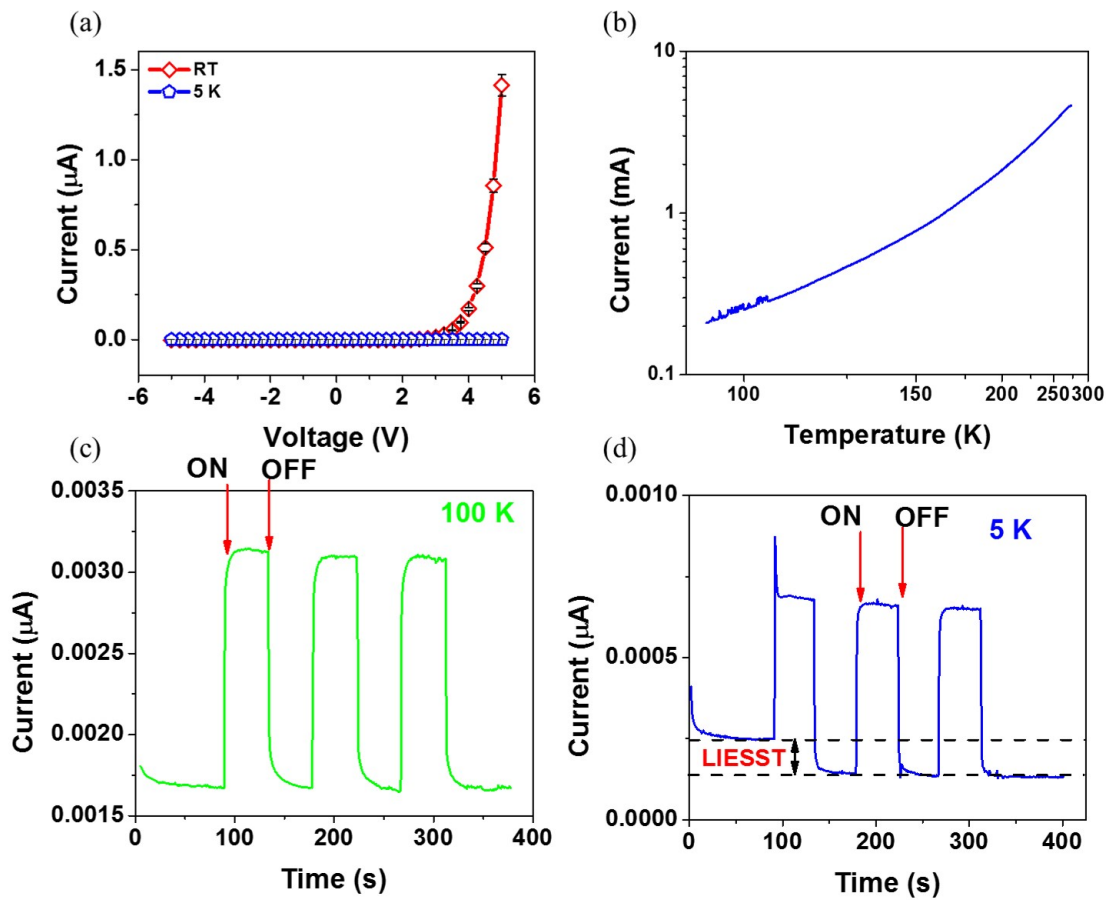
Figure 4.14: Electrical characteristics of a 30 nm junction. (a) I-V curves registered at room temperature and 5 K. b) Temperature dependence of the conductivity of the junction. (c-d) Visible light irradiation effect on the current flowing in the junction at 5 K (c) and 100 K (d).

The resistance of the junction is strongly temperature dependent and increases ca. one order of magnitude between 293 K and 100 K (Figure 4.14b). Below ca. 100 K the rectification ratio starts to decrease and at 5 K the I-V curve becomes nearly symmetric - similar to the 10 nm junction (see Figure 4.15 for the detailed representation of the I-V curves and the F-N $ln(I/V^2)$ vs. $1/V$ representation at 5 K). In other words at low temperatures the 30 nm junction exhibits tunneling behavior. The Arrhenius plot of the conductivity of the device exhibit a change of slope near 200 K. It is tempting to link this phenomenon with the occurrence of thermal SCO below 200 K, but this correlation may be

only fortuitous. In this case also a more obvious correlation was obtained through photo-induced spin-state switching experiments. When shining white light on the device at 5 K we observed a prompt increase of the current intensity from 250 pA to 870 pA, followed immediately by a decrease back to 700 pA (Figure 4.14c). When the light was turned off the current level dropped back to 150 pA. In the subsequent ON/OFF cycles, only a reversible switching between 150 and 700 pA has been observed. The complete sequence (dark cooling and light ON/OFF cycles) was well reproduced several times. In analogy with the 10 nm junction the 'irreversible' current drop was attributed to the LIESST effect. This hypothesis is well supported by the experiments at 100 K, wherein only the reversible photocurrent phenomenon was observed even for the first irradiation (Figure 4.14d). One might notice that the LIESST effect on this junction is more important: when going from the LS to the HS state the tunneling current drops by ca. 48 %.
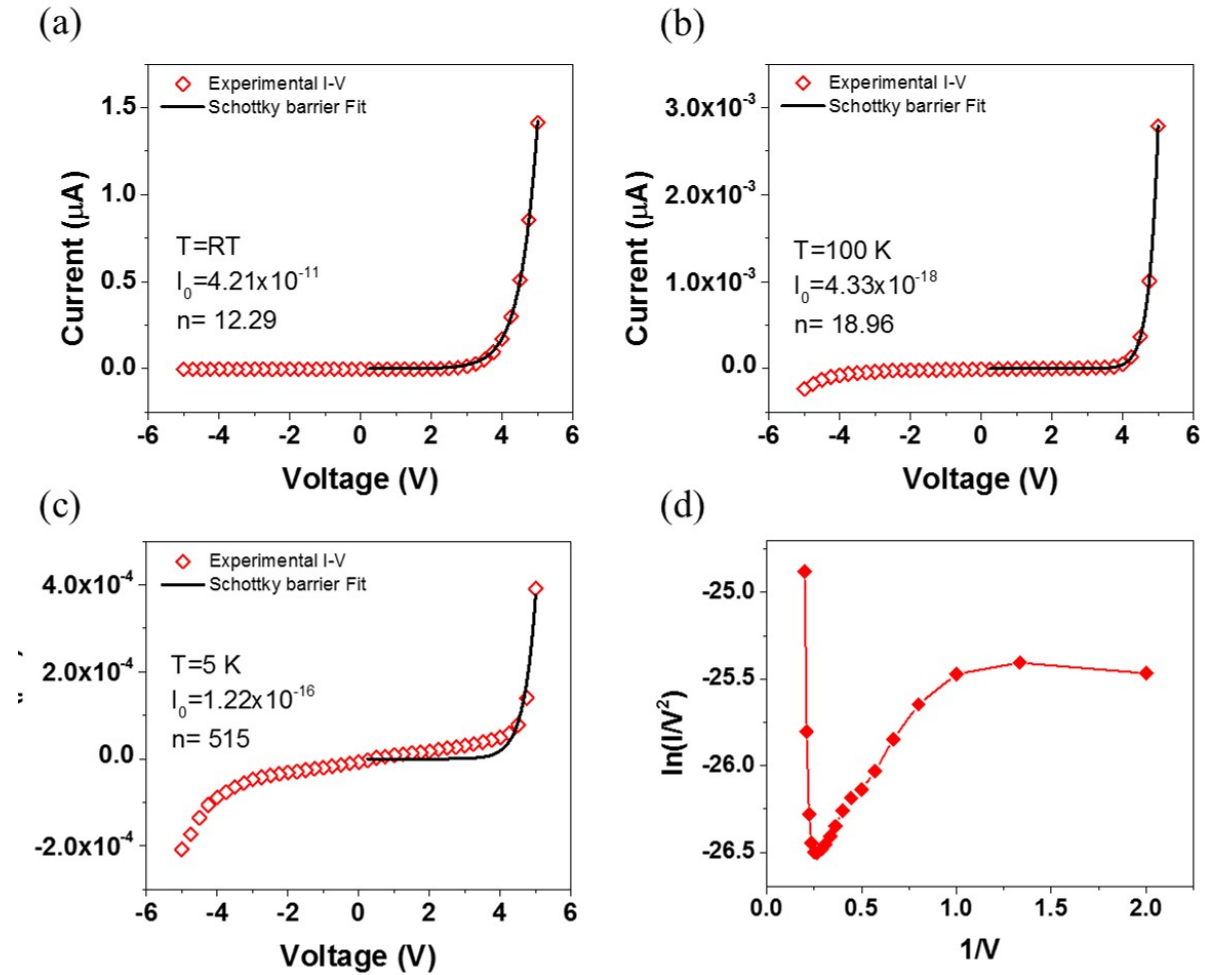
Figure 4.15: I-V data of the 30 nm device acquired at (a) room temperature, (b) 100 K and (c) 5 K. The straight lines correspond to fits of the data with the diode equation. (d) I-V curve plotted as $ln(I/V^2)$ vs. $1/V$ for F-N tunneling. The fitted parameters are shown in the figures.

The Al/1/ITO and Al/1/PEDOT-PSS/ITO junctions with 100 nm films of 1 was also tested and, overall a very similar, diode-type, characteristics as for the 30 nm junctions, i.e. a rectification behavior and strong thermal activation was observed (see Figures 4.16 and 4.17). However, in these devices we could not put in evidence any sign of the spin-

state switching on the conductance of the junction neither in the thermal SCO nor in the LIESST regimes. Furthermore the decrease of the rectification ratio to ca. 35 suggests that in these relatively thick junctions the current flow is also limited by the bulk conductivity besides the injection process. It may be worth to note also that 100 nm junctions do not show LIESST effect, but they exhibit the reversible photoconductivity phenomenon observed also in the 30 nm junctions. We thus tentatively assign this effect to photo-activated charge injection through the electrode interface barrier(s). It has to be noted that due to experimental reasons, the data for the 100 nm device could not be repeated several times, therefore these result have to be treated with caution until further experiments will be made.
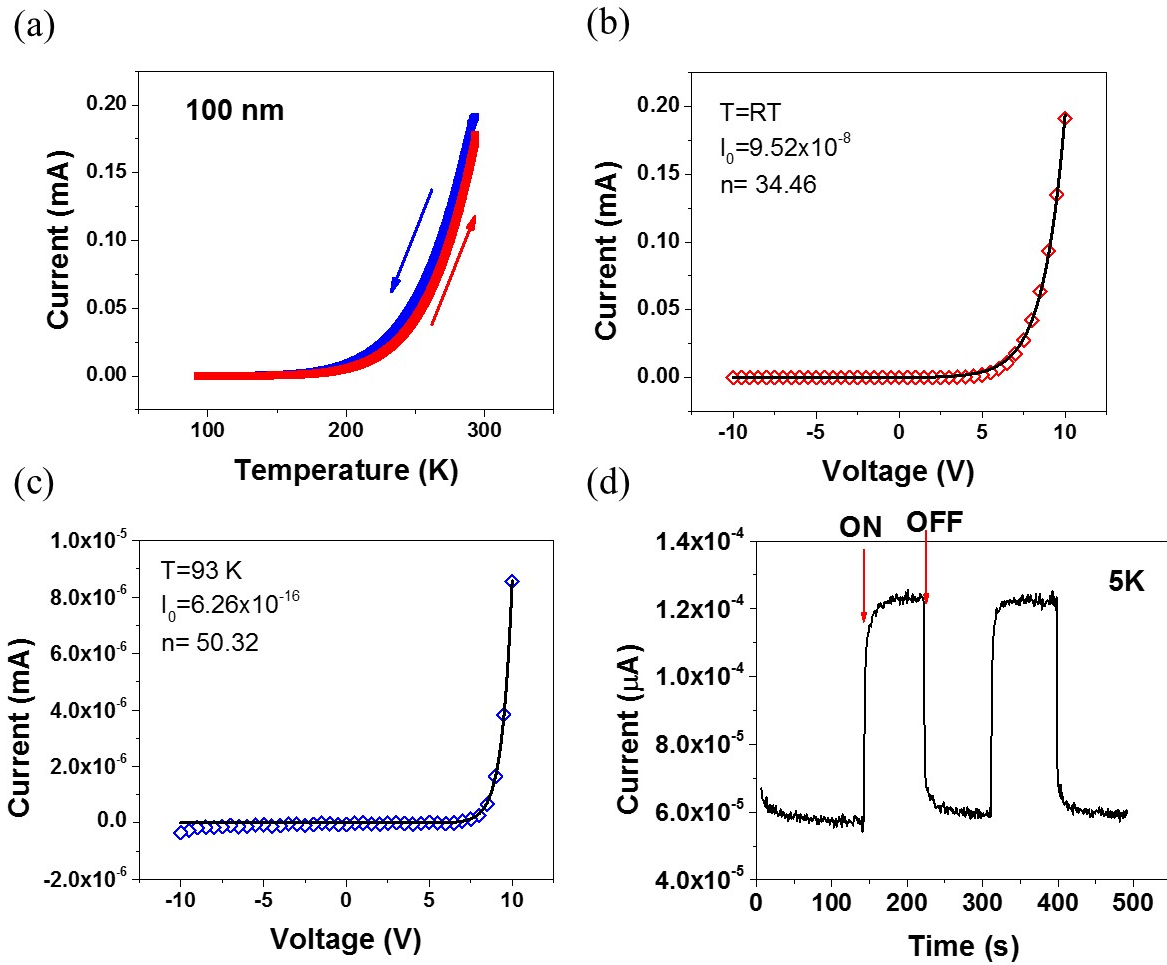
Figure 4.16: Electrical characteristics of the 100 nm ITO/1/Al junction. (a) I-T curve acquired on heating and cooling for an applied bias of 10 V. (b-c) I-V curves acquired at room temperature and 93 K. The straight lines correspond to fits of the data with the diode equation. The fitted parameters are shown in the figures. (d) Light irradiation effect on the current intensity at 5 K for two ON/OFF cycles.
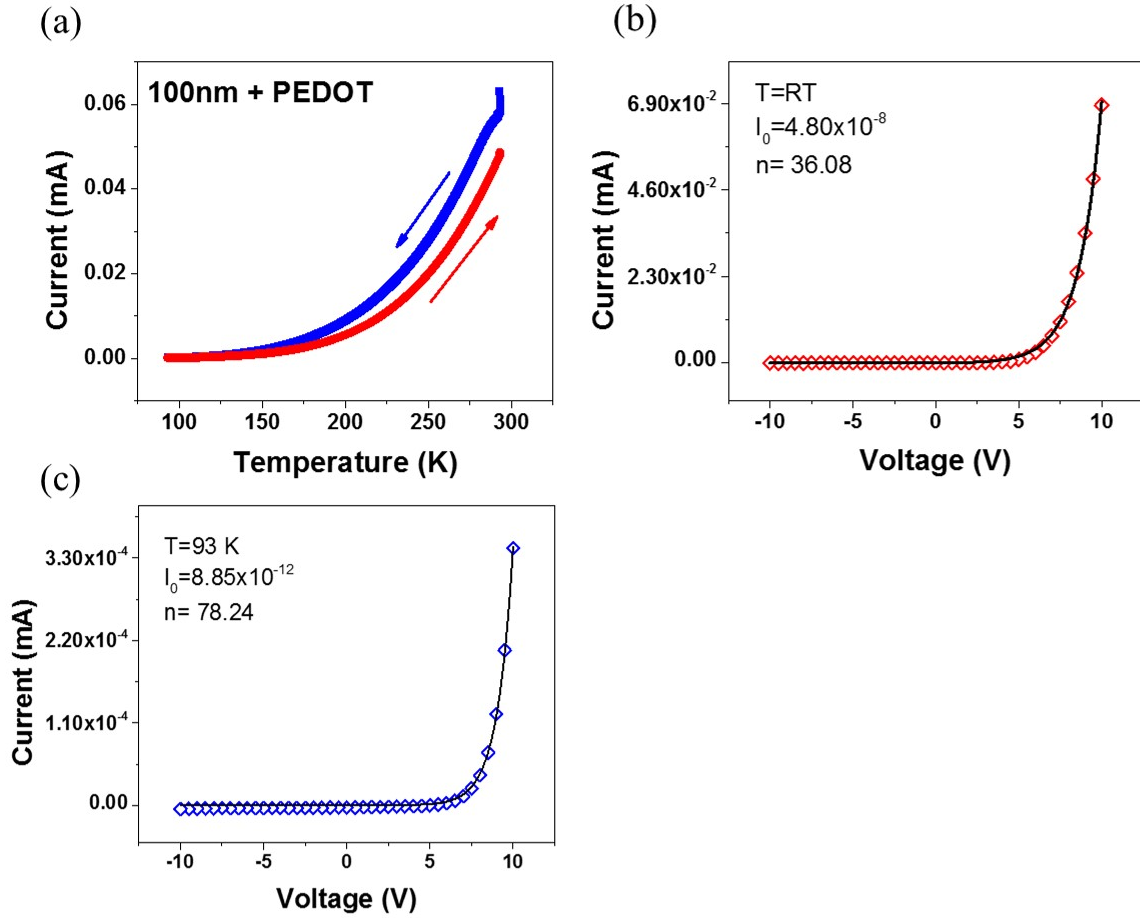
Figure 4.17: Electrical characteristics of the 100 nm ITO/PEDOT:PSS/1/Al junction. (a) I-T curve acquired on heating and cooling for an applied bias of 10 V. (b-c) I-V curves acquired at room temperature and 93 K. The straight lines correspond to fits of the data with the diode equation. The fitted parameters are shown in the figures.

To further investigate the charge transport process in the devices we have also measured their dielectric spectra, i.e. the frequency dependent complex permittivity, in a broad temperature range. Figure 4.18 shows the frequency dependence of the real part of the complex conductivity (σ') together with the dielectric loss modulus (M'') acquired at selected temperatures for the 10 nm, 30 nm and 100 nm junctions. The complex conductivity and the complex dielectric functions are related to each other by $\sigma' = i\omega\epsilon_0\epsilon^*$, where ϵ_0 is the permittivity of the free space and ω is the circular frequency, while the dielectric modulus is defined by $M^* = 1/\epsilon^*(\omega)$. One can observe very similar characteristics between the different junctions. Moreover, the master curves for σ' and M'' (see Figure 4.19) shows a good overlap of the curves, indicating the same conduction mechanism and relaxation process at all temperatures.
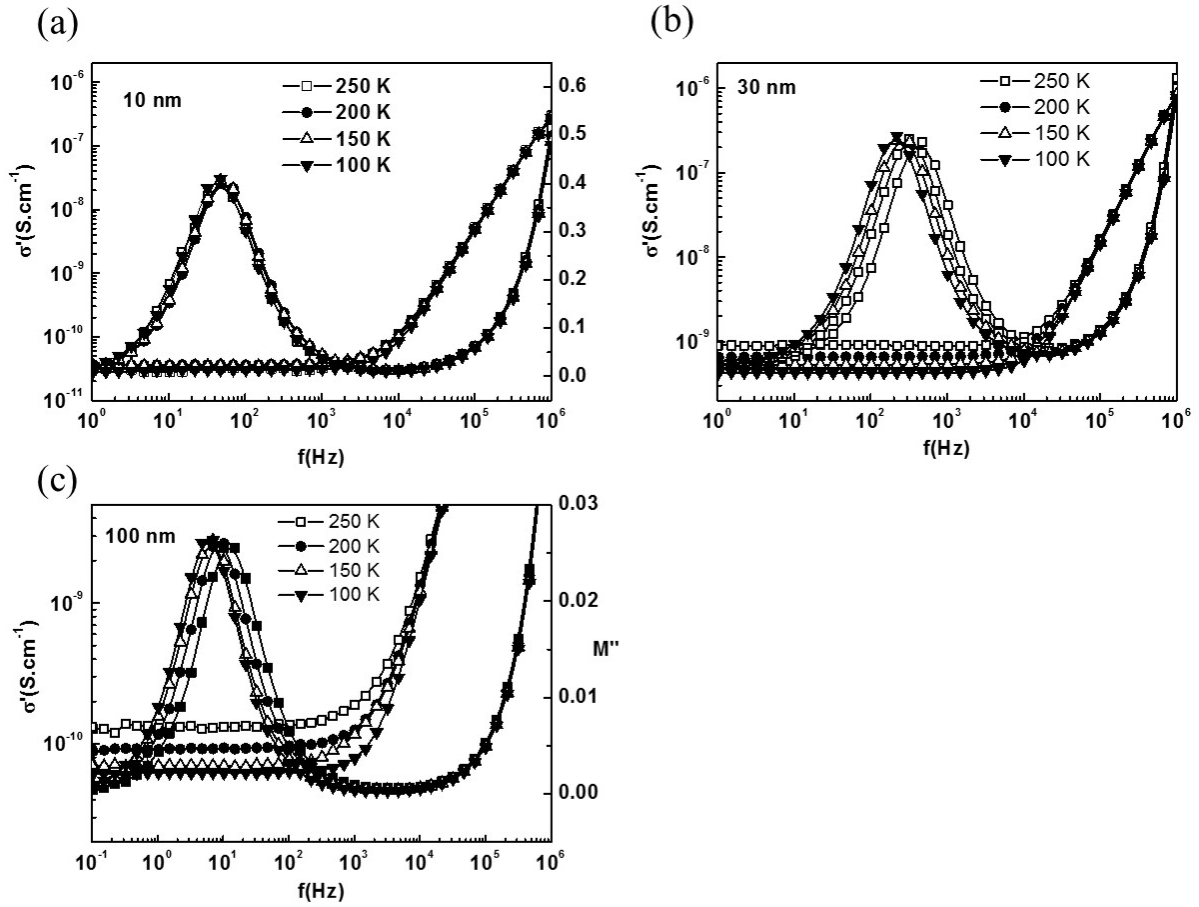
Figure 4.18: Variable temperature dielectric spectra showing the frequency dependence of the real part of the AC conductivity and that of the loss modulus at selected temperatures for (a) 10 nm, (b) 30 nm and (c) 100 nm junction.
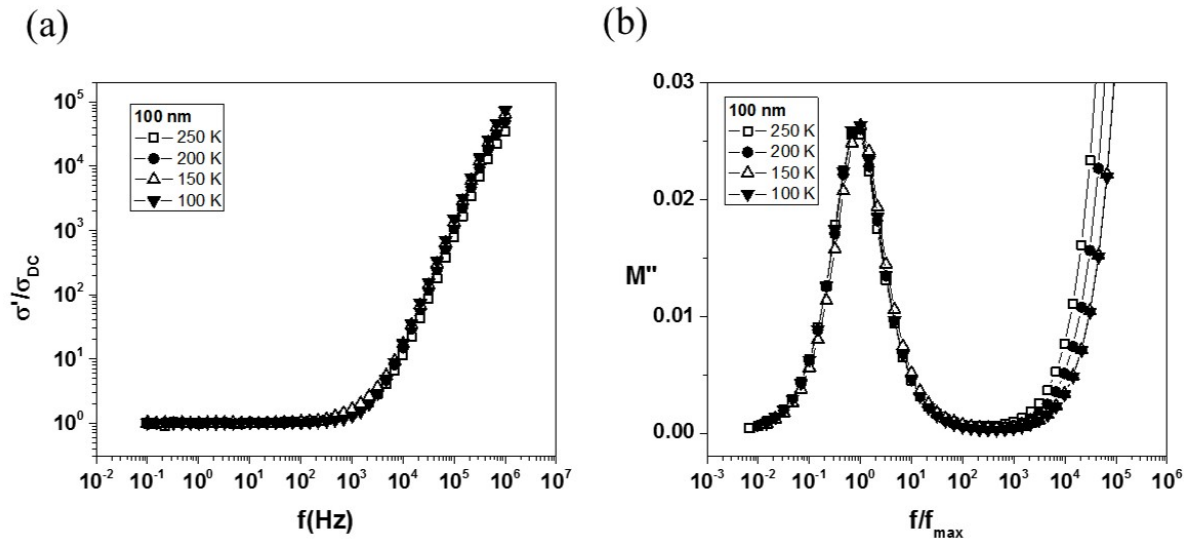
Figure 4.19: Variable temperature dielectric spectra showing the master curves of (a) the real part of the AC conductivity and (b) the loss modulus at selected temperatures for the 100 nm junction.

At low frequencies the conductivity is constant, while at high frequencies it exhibits power law behavior. A dielectric relaxation, characterized by a Debye loss peak, is also observed. This universal behavior of dielectrics [108] can be understood here as a combination of the junction resistance and the electrode interface capacitance, which is charged by the (weak) DC conduction. It is worth to stress the nearly ideal Debye behavior of the junctions, which is rarely observed experimentally. This means that the whole junction behaves as a single dipole. The sole, but of course crucial difference between the dielectric spectra of the junctions is observed in their temperature dependence. In the case of the 30 nm and 100 nm junctions both the conductivity and the relaxation frequency exhibit thermal activation, while for the 10 nm junction both quantities are temperature independent. To better illustrate this difference Figure 4.20 shows the Arrhenius plots for each device. It is clear that for the 10 nm device that no thermal activation of the charge carriers occur. The 30 nm and 100 nm devices clearly present two activated regions, the low temperature region which is characterized by a small activation energy, and a high temperature region that is characterized by a higher activation energy. This result can be tentatively interpreted as a spin state dependence of the conductivity, due to the fact that the change in activation energy is situated around the transition temperature of the SCO material.
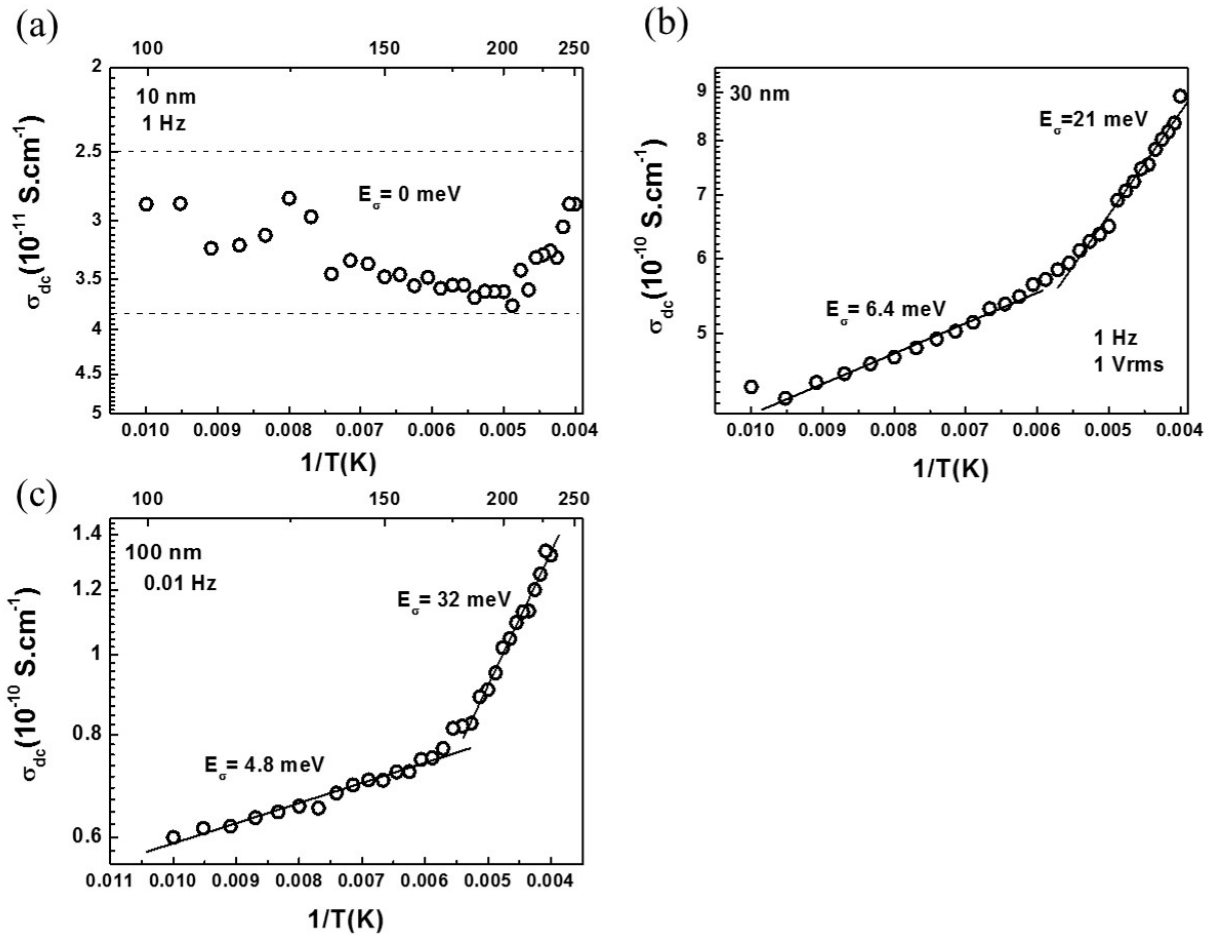
Figure 4.20: Arrhenius plots foof σ_{DC} for the (a) 10 nm, (b) 30 nm and (c) 100 nm devices.

Based on these data the charge transport in the different devices can ascribed to a similar hopping conductivity process. Taking into account the thickness of the tunneling junctions (10 - 30 nm) tunneling must refer here to a multistep tunneling by activationless

hopping between localized states. The hopping rate increases with increasing phonon (i.e. attempt) frequency and decreases with increasing distance between the localized states [150]. Since the LS to HS switching is well-known to result in a significant increase of the metal-ligand distances and thus a decrease of the associated vibrational frequencies we understand that this switching process must lead to a lower tunneling current, which is indeed observed in these experiments (It should be noted however that other parameters may also influence the tunneling current. In particular the variation of ϵ (see Figure 4.2) may play an important role). In the case of the rectifying junctions (30 - 100 nm) the conduction can be described as a thermally-activated charge injection into the molecular orbitals of **1** at one electrode interface, followed by thermally activated hopping through the junction to the other interface, where the charge extraction occurs. Indeed, the charge transport mechanism changes considerably from one device to another.

By considering the work functions of Al and ITO as well as the molecular orbital (MO) energy levels of **1** (see Figure 4.21), calculated by density functional theory (DFT) [93], it appears that most probably the barriers for hole vs. electron injection are low vs. high and thus the low current associated with negative polarity occurs due to the higher work function of ITO vs. Al. However, this picture would also imply a significant impact of the spin state switching on the injection barrier(s), which was not observed in these experiments. A first hypothesis would concern the uncertainty of DFT calculations in terms of the absolute positions of MO orbitals. Nevertheless even if the shift of the LUMO energy level upon the spin state switching is overestimated by the DFT there must obviously exist some shift. It can be supposed that this effect may be hidden in these experiments by the strong intrinsic thermal and photo-sensitivity of the current in these junctions.
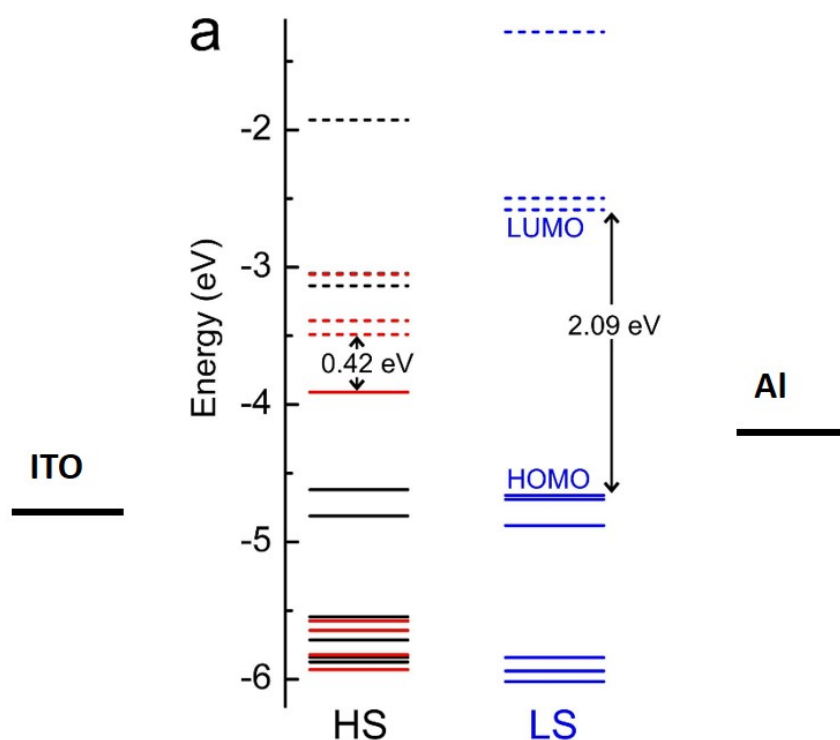
Figure 4.21: Molecular orbital energy scheme of **1** (adsorbed on Au(111) surface) in the HS and LS states calculated by DFT. The work functions of the electrodes are also indicated.

4.3 Conclusions

In summary, vertical optoelectronic devices were fabricated with thin films of the [*Fe*(*bpz*)$_2$(*phen*)] spin crossover complex sandwiched between large area electrodes. The devices with 10 nm junctions display tunneling conductivity, while the 100 nm junctions exhibit diode characteristics in a broad temperature range. The 30 nm devices show intermediate behavior: tunneling at low T and rectification at high T. Experimental evidence that the spin-state switching of the junctions in the tunneling regime leads to a substantial and reversible increase/decrease of the tunneling current (up to 50 %) in the LS/HS states and we correlated this effect with the change of carrier hopping frequencies and distances upon the SCO is also provided. In the injection regime no effect of the SCO on the device characteristics could be observed, however this might be simply masked by the intrinsic properties of these junctions. Overall these results provide very promising perspectives for using spin crossover compounds in electronic devices. In addition, since the magnetic properties of the junction change also upon the SCO (diamagnetic vs. paramagnetic) even more appealing prospects appear for spintronic applications. Taking into account the current state of the art of the SCO field it is clear that there is no fundamental obstacle to prepare nanometric junctions with SCO compounds exhibiting room temperature switching properties. On the other hand, the technical challenge is substantial as it will be necessary to develop methods for the deposition of pinhole free films of these compounds between large area magnetic electrodes in a robust, reproducible way.

Chapter 5

General conclusions

The research presented in this thesis was motivated by the increasing interest of researchers in the development and study of spin crossover material based applications. These materials possess intriguing characteristics, the most important being molecular switching and hysteresis at nanometer level. These properties along with fast switching, sensitivity to different external stimuli and material design flexibility make these compounds suitable for various applications such as sensors, displays, memory or switching devices. During the last decade several prototypes and proofs of concept for various devices containing SCO materials have been proposed. However, reports of devices controlled by electrical signals are scarce. This might be a consequence of the rather limited understanding of the electrical properties of these materials, even though there are several remarkable studies on this topic. Starting from this state of the art, this thesis aimed for analyzing some interesting electrical properties of a few selected SCO materials from an experimental point of view.

In a first time we have investigated the benchmark spin crossover complex $[Fe(Htrz)_2 (trz)](BF_4)$ in the bulk powder form using broadband dielectric spectroscopy. We confirmed the rather low value (ca. 10^{-9} S/cm at 293 K) of its DC conductivity and showed that the previously reported drop of the DC conductance upon switching the complex from the LS to the HS state is also observable in the AC conductance within a broad frequency range (1 Hz - 1 MHz). The electric modulus formalism has been used to characterize the charge transport mechanism. In particular this approach revealed the co-existence of two distinct dielectric relaxation peaks at the same temperature corresponding to the two different spin states. The higher dielectric relaxation frequencies in the LS state suggest that the increase of the conductivity in this spin state occurs due to a higher charge carrier (polaron) hopping rate. We believe this will be the general trend for most SCO compounds since the hopping frequencies are strongly related to the mass density and the phonon frequencies of the material, which change in a similar manner in different SCO complexes. The electrical properties of the solid solutions $[Fe_{1-x}Zn_x(Htrz)_2(trz)](BF_4)$ (x = 0, 0.26 and 0.43) were then investigated in the next step in order to determine the influence of the substitution of the "active" iron center by the "inactive" zinc ion. The physico-chemical analysis revealed that the obtained powder samples were closely isostructural and the Zn dilution was homogeneous throughout the particles (of similar morphology), which are the necessary conditions for a pertinent comparison of their charge transport properties. Broadband dielectric spectroscopy revealed a considerable decrease in the electrical conductivity by ca. 6 orders of magnitude for the highest dilution as well as a shift of the spin transition towards lower temperatures and a shrinking of the hysteresis width. While the two latter

phenomena were quite predictable, the drop of the conductivity is a remarkable new result as it proves that the iron ions participate directly in the charge transport process.

Using the $[Fe(Htrz)_2(trz)](BF_4)$ sample, microelectronic devices have been also fabricated by dielectrophoresis. The resulting devices were tested by electrical means, revealing a clear and reproducible spin state dependency of the measured current. While the spin transition in the starting powder could withstand 3000 thermal spin-state switching cycles (with a slow shrinking of the hysteresis width), at the device level a significant drop of the current intensity was observed after each cycle. This has been tentatively attributed to a degradation of the electrical contacts between the particles and the gold electrodes. These devices were then used to investigate the influence of different external stimuli, such as temperature, applied bias, light irradiation and environmental effects (presence of humidity and oxygen). Significant photoeffects on the current intensity were observed in the LS state of the device. This phenomenon could be correlated with the mobility of the charge carriers, which is significantly higher in the low spin state of the material when compared to the high spin state. The observed light-induced phenomena are also related to some extent to the sample environment as the effects were more pronounced in the presence of oxygen and humidity, suggesting a surface-mediated photochemical process at its origin. The most promising result on these devices was the successful switch from the HS to LS state by means of an applied electric field. This is the first report of spin state switching using an electric field to induce the spin transition at the macroscopic scale. Nevertheless the spin conversion obtained by applying and external electric field on this scale remains rather low (5 % at best). The switch has been performed inside the hysteresis loop near the cooling branch of the hysteresis, which discards the possibility that the observed effects are thermally induced. The effect of the electric field has been reproduced qualitatively using a modified Ising-like model wherein the dielectric permittivity difference between the HS and LS complexes was considered as the main ingredient for the field effect.

Nanoelectronic devices were also fabricated using the $[Fe(bpz)_2(phen)]$ SCO complex, which was deposited by thermal evaporation between vertical electrodes. This way we could fabricate well reproducible devices with pinhole-free, large area SCO junctions of ca 10, 30 and 100 nm thickness. The thermal and light induced spin state switching in the devices was confirmed by optical means and correlated with the electrical characteristics. The charge transport mechanism in these devices was thickness dependent: temperature-independent tunneling for the 10 nm device and thermally activated, injection-limited conductance for the 100 nm device. The 30 nm device exhibited intermediate characteristics: diode-like rectification at high temperatures and tunneling behavior at low temperatures. The photo-induced spin-state switching effect on the device current has been clearly observed in the tunneling regime for the 10 nm and 30 nm devices, with the LS junction being more conducting (up to 50 % higher than the HS junction). We suggested the lower tunneling current in the HS state may be related to the reduced hopping rate of charge carriers. In the case of the rectifying junctions (30 - 100 nm) no obvious effect of the SCO on the electrical characteristics could be evidenced despite compelling theoretical predictions. It is possible, however, that the SCO effect on the current intensity was masked by the intrinsic sensitivity of these devices to temperature changes as well as to light irradiation.

Overall the results obtained in this thesis highlight that molecular spin crossover materials can be incorporated in various micro and nanoelectronic devices in a rather straightforward manner allowing for a reversible modulation of device electrical characteristics by means of spin-state switching of the metal complexes. From a fundamental point of view, further studies, including experimental as well as theoretical approaches, will be necessary

to obtain more insights into the relationship between the molecular structure and electrical properties of these compounds. Density functional theory (DFT) calculations may be particularly useful to this aim. Concerning the potential applications, the vertical junction devices we developed appear very promising. In particular, magneto-transport studies of these devices represent an exciting perspective due to the concomitant change of their electrical and magnetic characteristics. For further progress in this direction, it would be necessary to fabricate thin junctions exhibiting SCO around room temperature. A thorough investigation of the molecular orbitals involved in the charge transport process will be also indispensable using both theoretical (DFT) and experimental (voltammetry, photoelectron spectroscopy) methods.

List of publications

[1] **Lefter, C.**; Gural'skiy, I.y.A.; Peng, H.; Molnár, G.; Salmon, L.; Rotaru, A.; Bousseksou, A.; Demont, P. "Dielectric and charge transport properties of the spin crossover complex [Fe(Htrz)2(trz)](BF4)". physica status solidi (RRL) Rapid Research Letters 2014, 8, 191-193.

[2] **Lefter, C.**; Tricard, S.; Peng, H.; Molnár, G.; Salmon, L.; Demont, P.; Rotaru, A.; Bousseksou, A. "Metal substitution effects on the charge transport and spin crossover properties of [Fe1xZnx(Htrz)2(trz)](BF4) (trz = triazole)". The Journal of Physical Chemistry C 2015, 119, 8522-8529.

[3] **Lefter, C.**; Tan, R.; Dugay, J.; Tricard, S.; Molnár, G.; Salmon, L.; Carrey, J.; Rotaru, A.; Bousseksou, A. "Light induced modulation of charge transport phenomena across the bistability region in [Fe(Htrz)2(trz)](BF4) spin crossover micro-rods". Physical Chemistry Chemical Physics 2015, 17, 5151-5154.

[4] **Lefter, C.**; Tan, R.; Tricard, S.; Dugay, J.; Molnár, G.; Salmon, L.; Carrey, J.; Rotaru, A.; Bousseksou, A. "On the stability of spin crossover materials: From bulk samples to electronic devices". Polyhedron 2015, 102, 434-440.

[5] **Lefter, C.**; Tan, R.; Dugay, J.; Tricard, S.; Molnár, G.; Salmon, L.; Carrey, J.; Nicolazzi, W.; Rotaru, A.; Bousseksou, A. "Unidirectional electric field-induced spin-state switching in spin crossover based microelectronic devices". Chemical Physics Letters 2015, accepted, Editor's Choice article.

[6] **Lefter, C.**; Davesne, V.; Salmon, L.; Molnár, G.; Demont, P.; Rotaru, A.; Bousseksou, A. "Charge transport and electrical properties of spin crossover materials: towards nanoelectronic and spintronic devices". Magnetochemistry, Special Issue "Spin Crossover (SCO) Research" - Review, submitted.

Bibliography

[1] H. Rohrer, *Japanese Journal of Applied Physics*, 1993, **32**, 1335.

[2] P. S. Peercy, *Nature*, 2000, **406**, 1023–1026.

[3] R. W. Keyes, *Proceedings of the IEEE*, 2001, **89**, 227–239.

[4] S. J. v. d. Molen and P. Liljeroth, *Journal Of Physics: Condensed Matter*, 2010, **22**, 133001.

[5] M. Tsutsui and M. Taniguchi, *Sensors*, 2012, **12**, 7259–7298.

[6] S. Sanvito, *Chemical Society Reviews*, 2011, **40**, 3336–3355.

[7] O. Sato, *Proceedings of the Japan Academy Series B-Physical and Biological Sciences*, 2012, **88**, 213–225.

[8] P. A. de Silva, N. H. Q. Gunaratne and C. P. McCoy, *Nature*, 1993, **364**, 42–44.

[9] F. M. Raymo, *Advanced Materials*, 2002, **14**, 401–414.

[10] C. P. Collier, E. W. Wong, M. Belohradsky, F. M. Raymo, J. F. Stoddart, P. J. Kuekes, R. S. Williams and J. R. Heath, *Science*, 1999, **285**, 391–394.

[11] L. Bogani and W. Wernsdorfer, *Nat Mater*, 2008, **7**, 179–186.

[12] P. Gutlich and H. A. Goodwin, *Topics in Current Chemistry. Spin Crossover in Transition Metal Compounds I.*, Springer-Verlag, Berlin, 2004.

[13] A. Bousseksou, G. Molnar, L. Salmon and W. Nicolazzi, *Chemical Society Reviews*, 2011, **40**, 3313–3335.

[14] P. Gutlich, A. Hauser and H. Spiering, *Angewandte Chemie-International Edition in English*, 1994, **33**, 2024–2054.

[15] H. Spiering, K. Boukheddaden, J. Linares and F. Varret, *Physical Review B*, 2004, **70**, 184106–184116.

[16] J. K. McCusker, K. N. Walda, R. C. Dunn, J. D. Simon, D. Magde and D. N. Hendrickson, *Journal of the American Chemical Society*, 1992, **114**, 6919–6920.

[17] J. F. Letard, P. Guionneau and L. Goux-Capes, in *Towards spin crossover applications*, 2004, vol. 235, pp. 221–249.

[18] O. Kahn and C. J. Martinez, *Science*, 1998, **279**, 44–48.

[19] J. Linares, E. Codjovi and Y. Garcia, *Sensors*, 2012, **12**, 4479–4492.

[20] C. Bartual-Murgui, A. Akou, C. Thibault, G. Molnar, C. Vieu, L. Salmon and A. Bousseksou, *Journal of Materials Chemistry C*, 2015, **3**, 1277–1285.

[21] L. Salmon, G. Molnar, D. Zitouni, C. Quintero, C. Bergaud, J. C. Micheau and A. Bousseksou, *Journal of Materials Chemistry*, 2010, **20**, 5499–5503.

[22] M. Matsuda, K. Kiyoshima, R. Uchida, N. Kinoshita and H. Tajima, *Thin Solid Films*, 2013, **531**, 451–453.

[23] H. J. Shepherd, I. A. Gural'skiy, C. M. Quintero, S. Tricard, L. Salmon, G. Molnar and A. Bousseksou, *Nat Commun*, 2013, **4**, 26071–26079.

[24] A. Bousseksou, G. Molnar, P. Demont and J. Menegotto, *Journal of Materials Chemistry*, 2003, **13**, 2069–2071.

[25] S. Bonhommeau, T. Guillon, L. M. L. Daku, P. Demont, J. S. Costa, J. F. Letard, G. Molnar and A. Bousseksou, *Angewandte Chemie-International Edition*, 2006, **45**, 1625–1629.

[26] C. Faulmann, S. Dorbes, S. Lampert, K. Jacob, B. G. de Bonneval, G. Molnar, A. Bousseksou, J. A. Real and L. Valade, *Inorganica Chimica Acta*, 2007, **360**, 3870–3878.

[27] K. Takahashi, H. B. Cui, Y. Okano, H. Kobayashi, Y. Einaga and O. Sato, *Inorganic Chemistry*, 2006, **45**, 5739–5741.

[28] M. Nihei, N. Takahashi, H. Nishikawa and H. Oshio, *Dalton Transactions*, 2011, **40**, 2154–2156.

[29] L. Salmon, G. Molnar, S. Cobo, P. Oulie, M. Etienne, T. Mahfoud, P. Demont, A. Eguchi, H. Watanabe, K. Tanakae and A. Bousseksou, *New Journal of Chemistry*, 2009, **33**, 1283–1289.

[30] T. Mahfoud, G. Molnar, S. Cobo, L. Salmon, C. Thibault, C. Vieu, P. Demont and A. Bousseksou, *Applied Physics Letters*, 2011, **99**, 053307–053310.

[31] A. Rotaru, I. A. Gural'skiy, G. Molnar, L. Salmon, P. Demont and A. Bousseksou, *Chemical Communications*, 2012, **48**, 4163–4165.

[32] C. Etrillard, V. Faramarzi, J.-F. Dayen, J.-F. Letard and B. Doudin, *Chemical Communications*, 2011, **47**, 9663–9665.

[33] M. S. Alam, M. Stocker, K. Gieb, P. Muller, M. Haryono, K. Student and A. Grohmann, *Angewandte Chemie-International Edition*, 2010, **49**, 1159–1163.

[34] V. Meded, A. Bagrets, K. Fink, R. Chandrasekar, M. Ruben, F. Evers, A. Bernand-Mantel, J. S. Seldenthuis, A. Beukman and H. S. J. van der Zant, *Physical Review B*, 2011, **83**, 245415.

[35] F. Prins, M. Monrabal-Capilla, E. A. Osorio, E. Coronado and H. S. J. van der Zant, *Advanced Materials*, 2011, **23**, 1545–1549.

[36] A. Rotaru, J. Dugay, R. P. Tan, I. A. Gural'skiy, L. Salmon, P. Demont, J. Carrey, G. Molnar, M. Respaud and A. Bousseksou, *Advanced Materials*, 2013, **25**, 1745–1749.

[37] L. Cambi and A. Gagnasso, *Atti. Accad. Naz. Lincei*, 1931, **13**, 809.

[38] J. W.A. Baker and H. Bobonich, *Inorganic Chemistry*, 1964, **3**, 1184.

[39] P. Guetlich, A. B. Gaspar and Y. Garcia, *Beilstein Journal of Organic Chemistry*, 2013, **9**, 342–391.

[40] T. Mahfoud, G. Molnar, S. Bonhommeau, S. Cobo, L. Salmon, P. Demont, H. Tokoro, S. I. Ohkoshi, K. Boukheddaden and A. Bousseksou, *Journal of the American Chemical Society*, 2009, **131**, 15049–15054.

[41] S. M. Neville, B. A. Leita, G. J. Halder, C. J. Kepert, B. Moubaraki, J. F. Letard and K. S. Murray, *Chemistry-a European Journal*, 2008, **14**, 10123–10133.

[42] W. Bauer, W. Scherer, S. Altmannshofer and B. Weber, *European Journal of Inorganic Chemistry*, 2011, **18**, 2803–2818.

[43] V. A. Money, C. Carbonera, J. Elhaik, M. A. Halcrow, J. A. K. Howard and J. F. Letard, *Chemistry-a European Journal*, 2007, **13**, 5503–5514.

[44] P. Gutlich, A. B. Gaspar, V. Ksenofontov and Y. Garcia, *Journal of Physics-Condensed Matter*, 2004, **16**, S1087–S1108.

[45] F. Varret, A. Bleuzen, K. Boukheddaden, A. Bousseksou, E. Codjovi, C. Enachescu, A. Goujon, J. Linares, N. Menendez and M. Verdaguer, *Pure and Applied Chemistry*, 2002, **74**, 2159–2168.

[46] C. Slichter and H. Drickamer, *J. Chem. Phys.*, 1972, **56**, 2142–2160.

[47] Y. Qi, E. W. Mller, H. Spiering and P. Gtlich, *Chemical Physics Letters*, 1983, **101**, 503–505.

[48] A. Bousseksou, N. Negre, M. Goiran, L. Salmon, J. P. Tuchagues, M. L. Boillot, K. Boukheddaden and F. Varret, *European Physical Journal B*, 2000, **13**, 451–456.

[49] A. Bousseksou, K. Boukheddaden, M. Goiran, C. Consejo, M. L. Boillot and J. P. Tuchagues, *Physical Review B*, 2002, **65**, 172412.

[50] J. J. McGravey and I. Lawthers, *Journal of the Chemical Society, Chemical Communications*, 1982, 906–907.

[51] S. Decurtins, P. Gutlich, C. P. Kohler, H. Spiering and A. Hauser, *Chemical Physics Letters*, 1984, **105**, 1–4.

[52] A. Hauser, *Chemical Physics Letters*, 1986, **124**, 543–548.

[53] A. Hauser, *Journal of Chemical Physics*, 1991, **94**, 2741–2748.

[54] S. Bonhommeau, G. Molnar, A. Galet, A. Zwick, J. A. Real, J. J. McGarvey and A. Bousseksou, *Angewandte Chemie-International Edition*, 2005, **44**, 4069–4073.

[55] S. Cobo, D. Ostrovskii, S. Bonhommeau, L. Vendier, G. Molnar, L. Salmon, K. Tanaka and A. Bousseksou, *Journal of the American Chemical Society*, 2008, **130**, 9019–9024.

[56] F. Varret, H. Constant-Machado, J. L. Dormann, A. Goujon, J. Jeftic, M. Nogues, A. Bousseksou, S. Klokishner, A. Dolbecq and M. Verdaguer, *Hyperfine Interactions*, 1998, **113**, 37–46.

[57] W. Morscheidt, J. Jeftic, E. Codjovi, J. Linares, A. Bousseksou, H. Constant-Machado and F. Varret, *Measurement Science and Technology*, 1998, **9**, 1311–1315.

[58] M. A. Halcrow, *Spin-Crossover Materials: Properties and Applications*, John Wiley and Sons, February 2013, pp. 1–564.

[59] H. Naggert, J. Rudnik, L. Kipgen, M. Bernien, F. Nickel, L. M. Arruda, W. Kuch, C. Nather and F. Tuczek, *Journal of Materials Chemistry C*, 2015, **3**, 7870–7877.

[60] A. B. Gaspar, V. Ksenofontov, M. Seredyuk and P. Gutlich, *Coordination Chemistry Reviews*, 2005, **249**, 2661–2676.

[61] Y. Garcia, G. Bravic, C. Gieck, D. Chasseau, W. Tremel and P. Gutlich, *Inorganic Chemistry*, 2005, **44**, 9723–9730.

[62] J. R. Galan-Mascaros, E. Coronado, A. Forment-Aliaga, M. Monrabal-Capilla, E. Pinilla-Cienfuegos and M. Ceolin, *Inorganic Chemistry*, 2010, **49**, 5706–5714.

[63] M. M. Dirtu, A. D. Naik, J. Marchand-Brynaert and Y. Garcia, *International Conference on the Applications of the Mossbauer Effect*, 2010, **217**, 4.

[64] G. Molnar, V. Niel, J. A. Real, L. Dubrovinsky, A. Bousseksou and J. J. McGarvey, *Journal of Physical Chemistry B*, 2003, **107**, 3149–3155.

[65] N. O. Moussa, D. Ostrovskii, V. M. Garcia, G. Molnar, K. Tanaka, A. B. Gaspar, J. A. Real and A. Bousseksou, *Chemical Physics Letters*, 2009, **477**, 156–159.

[66] C. Bartual-Murgui, A. Akou, L. Salmon, G. Molnar, C. Thibault, J. A. Real and A. Bousseksou, *Small*, 2011, **7**, 3385–91.

[67] A. Bousseksou, G. Molnar and G. Matouzenko, *European Journal of Inorganic Chemistry*, 2004, 4353–4369.

[68] J. A. Wolny, R. Diller and V. Schuenemann, *European Journal of Inorganic Chemistry*, 2012, 2635–2648.

[69] P. Guetlich, *Zeitschrift Fur Anorganische Und Allgemeine Chemie*, 2012, **638**, 15–43.

[70] E. Konig, G. Ritter and S. K. Kulshreshtha, *Chemical Reviews*, 1985, **85**, 219–234.

[71] S. Alvarez, *Journal of the American Chemical Society*, 2003, **125**, 6795–6802.

[72] T. Guillon, S. Bonhommeau, J. S. Costa, A. Zwick, J.-F. Letard, P. Demont, G. Molnar and A. Bousseksou, *Physica Status Solidi a-Applications and Materials Science*, 2006, **203**, 2974–2980.

[73] M. Nakano, N. Fujita, G. E. Matsubayashi and W. Mori, *Molecular Crystals and Liquid Crystals*, 2002, **379**, 365–370.

[74] C. Faulmann, S. Dorbes, W. G. de Bonneval, G. Molnar, A. Bousseksou, C. J. Gomez-Garcia, E. Coronado and L. Valade, *European Journal of Inorganic Chemistry*, 2005, 3261–3270.

[75] S. Dorbes, L. Valade, J. A. Real and C. Faulmann, *Chemical Communications*, 2005, 69–71.

[76] C. Faulmann, K. Jacob, S. Dorbes, S. Lampert, I. Malfant, M. L. Doublet, L. Valade and J. A. Real, *Inorganic Chemistry*, 2007, **46**, 8548–8559.

[77] K. Takahashi, H. B. Cui, H. Kobayashi, Y. Einaga and O. Sato, *Chemistry Letters*, 2005, **34**, 1240–1241.

[78] K. Fukuroi, K. Takahashi, T. Mochida, T. Sakurai, H. Ohta, T. Yamamoto, Y. Einaga and H. Mori, *Angewandte Chemie International Edition*, 2014, **53**, 1983–1986.

[79] B. Djukic and M. T. Lemaire, *Inorganic Chemistry*, 2009, **48**, 10489–10491.

[80] C. Faulmann, S. Dorbes, J. A. Real and L. Valade, *Journal of Low Temperature Physics*, 2006, **142**, 261–266.

[81] K. Takahashi, H. B. Cui, Y. Okano, H. Kobayashi, H. Mori, H. Tajima, Y. Einaga and O. Sato, *Journal of the American Chemical Society*, 2008, **130**, 6688–6689.

[82] H. Phan, S. M. Benjamin, E. Steven, J. S. Brooks and M. Shatruk, *Angewandte Chemie International Edition*, 2015, **54**, 823–827.

[83] Y.-S. Koo and J. R. Galn-Mascars, *Advanced Materials*, 2014, **26**, 6785–6789.

[84] Y.-C. Chen, Y. Meng, Z.-P. Ni and M.-L. Tong, *Journal of Materials Chemistry C*, 2015, **3**, 945–949.

[85] I. A. Gural'skiy, C. M. Quintero, J. S. Costa, P. Demont, G. Molnar, L. Salmon, H. J. Shepherd and A. Bousseksou, *Journal of Materials Chemistry C*, 2014, **2**, 2949–2955.

[86] M. Matsuda, H. Isozaki and H. Tajima, *Thin Solid Films*, 2008, **517**, 1465–1467.

[87] S. Shi, G. Schmerber, J. Arabski, J. B. Beaufrand, D. J. Kim, S. Boukari, M. Bowen, N. T. Kemp, N. Viart, G. Rogez, E. Beaurepaire, H. Aubriet, J. Petersen, C. Becker and D. Ruch, *Applied Physics Letters*, 2009, **95**, 043303.

[88] X. Zhang, T. Palamarciuc, J.-F. Letard, P. Rosa, E. V. Lozada, F. Torres, L. G. Rosa, B. Doudin and P. A. Dowben, *Chemical Communications*, 2014, **50**, 2255–2257.

[89] J. Dugay, M. Gimnez-Marqus, T. Kozlova, H. W. Zandbergen, E. Coronado and H. S. J. van der Zant, *Advanced Materials*, 2015, **27**, 1288–1293.

[90] A. Grohmann, M. Haryono, K. Student, P. Mller and M. Stocker, *European Journal of Inorganic Chemistry*, 2013, **2013**, 662–669.

[91] T. Palamarciuc, J. C. Oberg, F. El Hallak, C. F. Hirjibehedin, M. Serri, S. Heutz, J.-F. Letard and P. Rosa, *Journal of Materials Chemistry*, 2012, **22**, 9690–9695.

[92] A. Pronschinske, Y. Chen, G. F. Lewis, D. A. Shultz, A. Calzolari, M. Buongiorno Nardelli and D. B. Dougherty, *Nano Letters*, 2013, **13**, 1429–1434.

[93] T. G. Gopakumar, F. Matino, H. Naggert, A. Bannwarth, F. Tuczek and R. Berndt, *Angewandte Chemie-International Edition*, 2012, **51**, 6262–6266.

[94] T. Miyamachi, M. Gruber, V. Davesne, M. Bowen, S. Boukari, L. Joly, F. Scheurer, G. Rogez, T. K. Yamada, P. Ohresser, E. Beaurepaire and W. Wulfhekel, *Nature communications*, 2012, **3**, 938.

[95] M. Gruber, V. Davesne, M. Bowen, S. Boukari, E. Beaurepaire, W. Wulfhekel and T. Miyamachi, *Physical Review B*, 2014, **89**, 195415.

[96] S. Gueddida and M. Alouani, *Physical Review B*, 2013, **87**, 144413.

[97] A. S. Zyazin, J. W. G. van den Berg, E. A. Osorio, H. S. J. van der Zant, N. P. Konstantinidis, M. Leijnse, M. R. Wegewijs, F. May, W. Hofstetter, C. Danieli and A. Cornia, *Nano Letters*, 2010, **10**, 3307–3311.

[98] E. J. Devid, P. N. Martinho, M. V. Kamalakar, I. alitro, n. Prendergast, J.-F. Dayen, V. Meded, T. Lemma, R. Gonzlez-Prieto, F. Evers, T. E. Keyes, M. Ruben, B. Doudin and S. J. van der Molen, *ACS Nano*, 2015, **9**, 4496–4507.

[99] G. D. Harzmann, R. Frisenda, H. S. J. van der Zant and M. Mayor, *Angewandte Chemie International Edition*, 2015, 1–7.

[100] N. Baadji and S. Sanvito, *Physical Review Letters*, 2012, **108**, 217201.

[101] D. Aravena and E. Ruiz, *Journal of the American Chemical Society*, 2012, **134**, 777–9.

[102] E. Barsoukov and R. Macdonald, *Impedance Spectroscopy Theory, Experiment, and Applications*, John Wiley and Sons, Inc., New Jersey, 2005.

[103] N. Gondaliya, D. K. Kanchan, P. Sharma and M. S. Jayswal, *Polymer Composites*, 2012, **33**, 2195–2200.

[104] I. M. Hodge, K. L. Ngai and C. T. Moynihan, *Journal of Non-Crystalline Solids*, 2005, **351**, 104–115.

[105] K. Majhi, R. Vaish, G. Paramesh and K. B. R. Varma, *Ionics*, 2013, **19**, 99–104.

[106] R. Khazaka, M. L. Locatelli, S. Diaham, P. Bidan, L. Dupuy and G. Grosset, *Journal of Physics D-Applied Physics*, 2013, **46**, 1–7.

[107] G. Paramesh, R. Vaish and K. B. R. Varma, *Journal of Non-Crystalline Solids*, 2011, **357**, 1479–1484.

[108] A. K. Jonscher, *Nature*, 1977, **267**, 673–679.

[109] T. B. S. Jappe C. Dyre, *Reviews of Modern Phisics*, 2000, **72**, 837–892.

[110] M. Lalanne, P. Demont and A. Barnab, *Journal of Physics D: Applied Physics*, 2011, **44**, 185401.

[111] J. C. Dyre and T. B. Schrder, *Reviews of Modern Physics*, 2000, **72**, 873–892.

[112] P. Lunkenheimer, V. Bobnar, A. V. Pronin, A. I. Ritus, A. A. Volkov and A. Loidl, *Physical Review B*, 2002, **66**, 052105.

[113] S. Havriliak and S. Negami, *Polymer*, 1967, **8**, 161–210.

[114] G. Molnar, S. Cobo, T. Mahfoud, E. J. M. Vertelman, P. J. van Koningsbruggen, P. Demont and A. Bousseksou, *Journal of Physical Chemistry C*, 2009, **113**, 2586–2593.

[115] M. Sorai, J. Ensling and P. Gutlich, *Chemical Physics*, 1976, **18**, 199–209.

[116] J. P. Martin, J. Zarembowitch, A. Bousseksou, A. Dworkin, J. G. Haasnoot and F. Varret, *Inorganic Chemistry*, 1994, **33**, 6325–6333.

[117] H. Spiering, E. Meissner, H. Koppen, E. W. Muller and P. Gutlich, *Chemical Physics*, 1982, **68**, 65–71.

[118] P. Gutlich, A. Hauser and H. Spiering, *Angewandte Chemie-International Edition in English*, 1994, **33**, 2024–2054.

[119] P. Gutlich and H. A. Goodwin, *Spin Crossover in Transition Metal Compounds I*, 2004, **233**, 1–47.

[120] A. Hauser, A. Vef and P. Adler, *Journal of Chemical Physics*, 1991, **95**, 8710–8717.

[121] E. Coronado, J. R. Galan-Mascaros, M. Monrabal-Capilla, J. Garcia-Martinez and P. Pardo-Ibanez, *Advanced Materials*, 2007, **19**, 1359–1361.

[122] R. Tanasa, C. Enachescu, A. Stancu, F. Varret, J. Linares and E. Codjovi, *Polyhedron*, 2007, **26**, 1820–1824.

[123] A. Rotaru, M. M. Dirtu, C. Enachescu, R. Tanasa, J. Linares, A. Stancu and Y. Garcia, *Polyhedron*, 2009, **28**, 2531–2536.

[124] R. Gerhardt, *Journal of Physics and Chemistry of Solids*, 1994, **55**, 1491–1506.

[125] A. Rouahi, A. Kahouli, F. Challali, M. P. Besland, C. Vallee, B. Yangui, S. Salimy, A. Goullet and A. Sylvestre, *Journal of Physics D-Applied Physics*, 2013, **46**, 065308–065315.

[126] J. Krober, J. P. Audiere, R. Claude, E. Codjovi, O. Kahn, J. G. Haasnoot, F. Groliere, C. Jay, A. Bousseksou, J. Linares, F. Varret and A. Gonthiervassal, *Chemistry of Materials*, 1994, **6**, 1404–1412.

[127] M. Ohba, K. Yoneda, G. Agusti, M. Carmen Munoz, A. B. Gaspar, J. A. Real, M. Yamasaki, H. Ando, Y. Nakao, S. Sakaki and S. Kitagawa, *Angewandte Chemie-International Edition*, 2009, **48**, 4767–4771.

[128] J. A. Real, A. B. Gaspar and M. C. Munoz, *Dalton Transactions*, 2005, **12**, 2062–2079.

[129] Y. Miyazaki, T. Nakamoto, S. Ikeuchi, K. Saito, A. Inaba, M. Sorai, T. Tojo, T. Atake, G. S. Matouzenko, S. Zein and S. A. Borshch, *Journal of Physical Chemistry B*, 2007, **111**, 12508–12517.

[130] S. Bonnet, G. Molnar, J. S. Costa, M. A. Siegler, A. L. Spek, A. Bousseksou, W. T. Fu, P. Gamez and J. Reedijk, *Chemistry of Materials*, 2009, **21**, 1123–1136.

[131] S. Bedoui, M. Lopes, S. Zheng, S. Bonnet, G. Molnar and A. Bousseksou, *Advanced Materials*, 2012, **24**, 2475–2478.

[132] A. Marino, M. Servol, R. Bertoni, M. Lorenc, C. Mauriac, J.-F. Ltard and E. Collet, *Polyhedron*, 2013, **66**, 123–128.

[133] V. Nagy, I. Suleimanov, G. Molnar, L. Salmon, A. Bousseksou and L. Csoka, *Journal of Materials Chemistry C*, 2015.

[134] P. R. C. Gascoyne and J. Vykoukal, *Electrophoresis*, 2002, **23**, 1973–1983.

[135] J. Voldman, in *Electrical forces for microscale cell manipulation*, 2006, vol. 8, pp. 425–454.

[136] H. Morgan, M. P. Hughes and N. G. Green, *Biophysical Journal*, 1999, **77**, 516–525.

[137] B. Yafouz, N. Kadri and F. Ibrahim, *Sensors*, 2014, **14**, 6356–6369.

[138] J. Carrey, H. Carrere, M. L. Kahn, B. Chaudret, X. Marie and M. Respaud, *Semiconductor Science and Technology*, 2008, **23**, 025003–025008.

[139] C. Soci, A. Zhang, B. Xiang, S. A. Dayeh, D. P. R. Aplin, J. Park, X. Y. Bao, Y. H. Lo and D. Wang, *Nano Letters*, 2007, **7**, 1003–1009.

[140] J. Yang, R. Li, N. Huo, W.-L. Ma, F. Lu, C. Fan, S. Yang, Z. Wei, J. Li and S.-S. Li, *RSC Advances*, 2014, **4**, 49873–49878.

[141] S. Bonhommeau, G. Molnar, M. Goiran, K. Boukheddaden and A. Bousseksou, *Physical Review B*, 2006, **74**, 064424–1 – 064424–8.

[142] C. Lefter, I. A. Gural'skiy, H. Peng, G. Molnr, L. Salmon, A. Rotaru, A. Bousseksou and P. Demont, *physica status solidi (RRL) Rapid Research Letters*, 2014, **8**, 191–193.

[143] H. Naggert, A. Bannwarth, S. Chemnitz, T. von Hofe, E. Quandt and F. Tuczek, *Dalton Transactions*, 2011, **40**, 6364–6366.

[144] I. A. Gural'skiy, C. M. Quintero, K. Abdul-Kader, M. Lopes, C. Bartual-Murgui, L. Salmon, P. Zhao, G. Molnr, D. Astruc and A. Bousseksou, *Journal of Nanophotonics*, 2012, **6**, 063517–1–063517–13.

[145] M. Bernien, H. Naggert, L. M. Arruda, L. Kipgen, F. Nickel, J. Miguel, C. F. Hermanns, A. Krger, D. Krger, E. Schierle, E. Weschke, F. Tuczek and W. Kuch, *ACS Nano*, 2015, **9**, 8960–8966.

[146] G. Felix, K. Abdul-Kader, T. Mahfoud, I. A. Gural'skiy, W. Nicolazzi, L. Salmon, G. Molnar and A. Bousseksou, *Journal of the American Chemical Society*, 2011, **133**, 15342–15345.

[147] J. G. Simmons, *Journal of Applied Physics*, 1963, **34**, 1793–1803.

[148] R. K. Gupta and R. A. Singh, *Journal of Polymer Research*, 2005, **11**, 269–273.

[149] H. Amrollahi Bioki, *Eur. Phys. J. Appl. Phys.*, 2013, **62**, 20201.

[150] N. F. Mott, *Philosophical Magazine*, 1969, **19**, 835–852.